Hydrogenated Amorphous Silicon and p/i-heterojunctions

Optical and Electrical Modeling and Technology as Applied to Solar Cells

Dit proefschrift is goedgekeurd door de promotoren:
Prof. dr. M. Kleefstra
Prof. dr. C.I.M. Beenakker

Samenstelling promotiecommissie:
Rector Magnificus, voorzitter
Prof. dr. M. Kleefstra, Technische Universiteit Delft, promotor
Prof. dr. C.I.M. Beenakker, Technische Universiteit Delft, promotor
Dr. J.W. Metselaar, Technische Universiteit Delft, toegevoegd promotor
Prof. dr. ir. J. Slotboom, Technische Universiteit Delft
Prof. dr. W. Th. Wenckebach, Technische Universiteit Delft
Prof. dr. W.C. Sinke, Rijks Universiteit Utrecht
Dr. M. Zeman, Technische Universiteit Delft

CIP-DATA KONINKLIJKE BIBLIOTHEEK, DEN HAAG
Trijssenaar, M.
Hydrogenated Amorphous Silicon and p/i-heterojunctions: Optical and Electrical Modeling and Technology as Applied to Solar Cells / M. Trijssenaar – Delft – Ill.
Thesis Delft University of Technology. – With Ref. – With Summary in Dutch.
Subject headings: solar cells, hydrogenated amorphous silicon, optical modeling, electrical modeling, heterojunctions.
NUGI 841

Printed in the Netherlands

Aan mijn ouders
Aan Inge

CONTENTS

CHAPTER 1

GENERAL INTRODUCTION

1.1 Historical background

A brief historical overview of hydrogenated amorphous silicon (a-Si:H) research is given below. In 1965, Sterling and Swan first reported the deposition of undoped a-Si:H produced by the Radio Frequency Chemical Vapor Deposition (RFCVD) of silane (SiH_4) [200]. The technique they used is essentially the same as that used today: silane gas molecules are dissociated by a radio frequency (rf) plasma and the radicals formed deposit on a heated substrate. In 1969, Chittick, Alexander and Sterling studied this material more elaboratedly and reported the absorption, the dark conductivity, the activation energy of the dark conductivity, the photoconductivity and space charge limited currents [21]. Also, they reported a small effect of doping with phosphorus on the dark conductivity of a-Si:H.

A breakthrough came in 1975 when Spear and LeComber reported systematic studies of p- and n-type doping of a-Si:H deposited by RFCVD over a wide dopant concentration range [194]. The p- and n-type doping was accomplished by adding respectively diborane (B_2H_6) or phosphine (PH_3) to the source gas. Up to the present, the common method employed to produce n- or p-type material is the use of these two doping gases. The possibility to produce devices with effectively doped and undoped regions opened the way to various applications, heralded by the announcement of a-Si:H solar cells one year later by Carlson and Wronski [17]. Since then much research has been conducted on a-Si:H solar cells, and, for example, the first triple cell was reported in 1979

by Hamakawa [61]. Especially after the oil crisis of 1973, research into renewable energy sources increased, and with it research on solar cells.

The RFCVD process lends itself very well to the production of large-area a-Si:H devices, with an area of typically up to one or more square meters. Over this area it allows the uniform deposition of thin, typically several hundred nanometers thick, a-Si:H layers. This process places almost no restrictions on the substrate material, it may be curved and only has to withstand about 300 °C, which for example enables the production of see-through sun roofs for cars with an a-Si:H solar cell integrated in it [155].

The use of a-Si:H in photovoltaics is one of the most important applications. Other important applications are in thin film transistors for active matrix addressing in liquid crystal displays [222], image sensors which are used in fax readers and laser printing [22], light-emitting diodes [86], charged coupled devices [113], multi-color detectors [233] and radiation detectors [153]. Several other applications are described by LeComber [91]. A good introduction to the application of a-Si:H in devices is given by Kanicki [81].

1.2 Scope of this work

In this thesis, research on hydrogenated a-Si:H for use in a-Si:H solar cells is described. The important optical and electrical properties of p- and i-layers for use in solar cells are described and measured. Amongst these properties are the refractive index, the absorption coefficient, the dark and photoconductivity, the Fermi level position and the density of states, including the defect density in the gap and the valence and conduction band tail characteristic energies.

The solar cell efficiency is not only determined by the properties of the separate layers, but also by the interface characteristics. Of the interfaces of a solar cell, the p/i-junction is the most important one. This junction was investigated by measuring its current-voltage characteristics, and fitting these measurements to computer simulations. For this purpose, values of material properties determined on single layers were used as an input for the modeling.

The research and commercial applications of a-Si:H in solar cells is technology ruled. Traditionally, a-Si:H solar cells and other a-Si:H devices are optimized by examination of the results of different deposition conditions on the material and device properties, rather than that the progress in this research is because of improvements in the theories. This is because still little is known about the fundamental electrical and optical properties of a-Si:H. The relationship between the microscopic and macroscopic properties are not yet well understood, which frustrates quantitative theoretical descriptions of the material. Also, the properties of a-Si:H films and devices depend on the fabrication methods, systems and conditions, which makes it difficult to compare materials or devices which are manufactured in different laboratories using different deposition systems.

So far, this approach has led to conversion efficiencies of small-area (1 cm^2) single-junction solar cells of 12.0 % in 1987 [65] and 13.2 % in 1992 [118]. Multi-junction solar cells achieve higher efficiencies than their single-junction counterparts because of the more effective absorption of light of different wavelengths of the solar spectrum. In 1988, an efficiency of 13.7 % was reported for a triple-junction solar cell [256], the efficiency of which has not been improved markedly up to the present.

Although this empirical research has proved to be successful, the theoretical limit of 26 % for single cells [63] has not yet been achieved. Theories of the electronic structure and optical properties of a-Si:H have been developed simultaneously with the empirical research in order to close the gap between the achieved and the theoretically maximum efficiencies, and to understand the results of the empirical research. Models were derived from these theories, which enabled the carrying out of computer simulations. We implemented a model in a computer program in order to investigate the p/i-junction of solar cells and to test the validity of the models.

Device simulations offer notable advantages over the actual production and measuring of test devices: generally they are much cheaper, the impact of small changes of a configuration can be determined much faster and are usually more reliable and, last but not least, simulations do not require the handling of very poisonous and spontaneously flammable

gases. Of course, simulations have to be calibrated in order to be valid. For this purpose simulation results and measurements are compared, and, if necessary, the model or input parameters are adapted to describe the measurements correctly. Therefore, the production and simulation of devices should be carried out hand in hand.

For crystalline silicon, it has already become generally accepted that device simulators do speed up device research considerably. Without a doubt, this will become the case for a-Si:H too.

1.3 Properties of amorphous and microcrystalline silicon

Different forms of silicon

Silicon can exist in several forms: monocrystalline, polycrystalline, microcrystalline and amorphous. In the crystalline form every atom is four-fold coordinated in a tetrahedral configuration. Polycrystalline silicon as used in solar cells consists of crystals with dimensions of several millimeters [120], separated by grain boundaries. Because in electronics the term polycrystalline silicon is usually associated with material with a much smaller crystallite size, Green suggested that the term semicrystalline is more appropriate [51]. At the grain boundaries the crystal orientation of the neighboring crystals change randomly. Microcrystalline silicon has essentially the same structure as polycrystalline silicon, but the crystal size is in the order of nanometers to micrometers. Because of the smaller crystallite size in microcrystalline silicon compared to that of polycrystalline silicon, the effect of the boundaries on the electronic properties is much more pronounced in microcrystalline silicon.

The disorder of the atomic structure is the main feature that distinguishes amorphous materials from crystalline materials. The dominant defects in amorphous silicon are dangling bonds, which arise when one of the four bonds of a silicon atom is not bonded to another silicon atom, but is non-bonding [159], 'dangling' so to speak. This silicon atom is thus three-fold coordinated; it is coordinated with one atom less than would be the case in the perfect structure, formed by tetrahedrally bonded atoms. The defect density of pure, unhydrogenated amorphous

silicon (a-Si) is high, in the order of 10^{18} cm^{-3}, for material produced by rf magnetron sputtering [211], to 10^{20} cm^{-3}, for material produced by conventional vacuum evaporation, sputtering [16] or ion-implantation [31]. This high defect density of unhydrogenated a-Si prevents photoconductance [55] and effective doping to take place, which makes this material from a technological point of view of no interest.

Hydrogenated amorphous silicon

The defect density of unhydrogenated amorphous silicon can be reduced by four to five orders of magnitude by hydrogenation of the material to a level of about 10 at.% hydrogen. The hydrogen passivates the dangling bonds, which means that the dangling bonds are no longer electrically active defect states [106, 205]. Because of this, hydrogenated amorphous silicon (a-Si:H) can be effectively doped and this is from a technological point of view of much interest. This material has many applications, of which the most important ones are mentioned in section 1.1. Depending on the amount of bonded hydrogen and its bonding configuration in the a-Si:H disordered network, the electronic properties vary widely. Except for this section, unhydrogenated amorphous silicon is not considered in this thesis.

Because the short-range order of a-Si:H resembles that of crystalline silicon, the general electronic structures of these two materials resemble each other. Both materials have a band gap, which is 1.12 eV for crystalline silicon [52], and around 1.65 to 1.85 eV for a-Si:H [40].

Electronic structure of a-Si:H

The lack of long-range order in the structure of a-Si:H results in conduction and valence band tails [123, 28]: the band edges decrease smoothly instead of abruptly as is the case in crystalline silicon. These broadened band edges are shown in figure 1.1 and have an exponential energy dependence. The greater the disorder, the more the band tails extend into the band gap. The energy for which the band tail state density increases a factor e, the base of the natural logarithm, is referred to as the

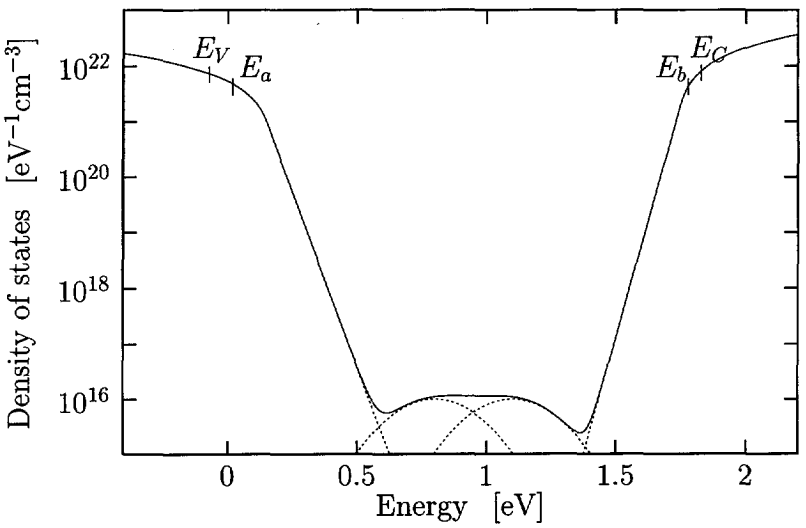

Figure 1.1: *Density of states in hydrogenated amorphous silicon. The energy levels E_V and E_C denote the mobility edges, defining the mobility gap as $E_C - E_V$, whereas the optical gap is given by the difference $E_b - E_a$.*

band tail characteristic energy or as the band tail slope. Although from a mathematical point of view the last term is less accurate, it is commonly used because it immediately rises the (correct) suggestion that the value determines the slope of the curve if the density of states (DOS) is plotted as a function of the energy on a logarithmic scale. The exponential part of the valence band tail of low-defect, high-quality a-Si:H has a characteristic energy of 40 to 45 meV, while the characteristic energy of the conduction band tail typically amounts to 25 to 30 meV.

Mott and Davis already in 1979 stated that a large density of states exists in the mid-gap region [126]. The electronic states in the band gap arise from dangling bonds, which are, as explained above, the unpaired electrons of three-fold coordinated silicon atoms. The large DOS pins the Fermi level around midgap in undoped material.

A quantitative relation between the dangling bond density and the band tail slope, found by Stutzmann, is discussed in section 2.7.2.

By doping a-Si:H, additional defects are created which act as recombination centers [106]. Also, doping causes a shift of the Fermi level, as shown in the historical work of Spear and LeComber [195]. The distance between the Fermi level and the near by mobility edge is determined by measuring the activation energy of the dark conductivity, which subject is treated in section 3.6.2.

Mobility gap and optical gap

The energy levels E_V and E_C, shown in figure 1.1, separate the localized band tail states from the extended states. The difference $E_C - E_V$ is defined as the mobility gap, and is of fundamental and practical interest because it is directly related to the free-carrier transport in amorphous semiconductors. The electronic properties of amorphous materials are described by the mobility gap, contrary to the optical properties, which are described by the optical gap. The optical gap is an extrapolation of the optical transitions between the bands associated with the extended states, as described in section 2.6.

There is no direct correlation between the optical gap and the mobility gap. However, it is theoretically suggested that the mobility edges are roughly 0.1 eV away from the exponential tail regions [192]. Also, the difference in value between these two gaps was determined experimentally to be 0.16 ± 0.03 eV for undoped a-Si:H [255]. The mobility gap was found by adding the separation of the valence band edge from the metal Fermi level to the separation of the electron mobility edge from the metal Fermi level, where the separations were found from internal photoemission experiments. For intrinsic a-Si:H with a Tauc optical gap of 1.73 eV, an effective mobility gap of 1.89 ± 0.03 eV was found, resulting in a difference between the optical and mobility gap of 0.16 ± 0.03 eV.

The optical gap of a-Si:H is a direct gap, in contrast with crystalline silicon, where the gap is indirect. The direct gap arises from the intrinsic disorder of the amorphous materials. A result of this direct gap is the much higher optical absorption of a-Si:H compared to crystalline silicon, resulting that a-Si:H solar cells can be much thinner than crystalline solar cells.

1.4 Fabrication of amorphous and microcrystalline silicon

Hydrogenated amorphous silicon and microcrystalline silicon films can be prepared by a variety of deposition techniques. Two kinds of deposition techniques can be distinguished: reactive sputtering [151] and chemical vapor deposition (CVD).

The sputtering technique ejects material from a target by ion bombardment from a plasma. Various types of sputtering techniques have been employed, such as radio frequent (rf), direct current (DC) and plasma magnetron. Sputtered amorphous silicon films are generally deposited by the rf sputtering of a polycrystalline silicon target in an argon atmosphere [103]. Hydrogen incorporation into the films is achieved by adding hydrogen gas to the sputtering gas. Sputtered a-Si:H has wide band tails [98], resulting in a small diffusion length. Therefore, solar cells fabricated by sputtering exhibit a poor fill factor and thus a poor overall performance.

The best solar cells are made with the CVD technology. In CVD, silicon-containing gas molecules are broken up and silicon deposits on the substrate. The energy to break up the silicon-containing molecules can be in the form of heat (pyrolytic CVD), light (photo-assisted CVD [49, 171]) or high energetic electrons (plasma enhanced (PE) CVD, also called glow discharge CVD). There are three main types of pyrolytic CVD: homogeneous (HOMO) CVD [178, 179], the substrate and the reactor have the same temperature and a hot gas is used; heterogeneous CVD, where the substrate is heated, and the recently developed hot wire or filament-assisted CVD [108, 246], where silane is decomposed on a hot tungsten filament.

In the plasma enhanced CVD technique, the plasma is generated by accelerating electrons in an electric field. The electric field can be set up by a direct current (DC) or by an alternating current (AC). Usually, for the deposition of amorphous silicon, a radio frequent (rf) alternating current is used, giving rise to the RFCVD deposition technique [112, 195]. In the RFCVD process, the energy can be coupled into the reactor inductively [195] or capacitively, where the latter coupling technique is the most widely used one.

RFCVD

Today, in industrial and device laboratory practice, the most common technique for the fabrication of a-Si:H devices is the capacitively coupled RFCVD. This deposition technique can be scaled up to an industrial scale, which is demonstrated by the total world production volume of 16.4 MW of a-Si:H solar cells in 1992, entirely produced by RFCVD [34].

In PECVD, silicon-containing gas molecules are broken up into radicals by collisions with electrons. The a-Si:H films grow by attachment of these very reactive radicals to the surface of the growing film. The electrons originate as secondary electrons in the collisions of electrons with gas molecules, and receive their energy by acceleration in the electric field. To pick up enough energy for the dissociation of silane molecules, the electrons must travel in the electric field for a sufficient distance. Therefore, the mean free path between collisions with molecules must be kept relatively large, but not so large that the probability of an high energetic electron colliding with a molecule approaches zero. This leads to an optimal gas pressure for sustaining the plasma in the order of 0.1 to 1.0 mbar [205]. The subject of glow discharge processes is extensively discussed by Chapman [20, p. 147-151].

Plasma frequency

Usually an AC plasma is used with a radio frequency of 13.56 MHz. This particular frequency is chosen because this is an internationally reserved frequency for industrial purposes with relaxed requirements for rf emission compared to other frequencies [20, p. 155]. Recently, also very high frequency (VHF) plasmas, with frequencies in the range of 30 to 300 MHz, have been used [46, 32, 133, 134]. Device quality a-Si:H deposited at 70 MHz has been reported [181]. Solar cells which incorporated this material for the intrinsic layer exhibited efficiencies of 8.0 to 9.0 %, for deposition rates of the intrinsic layer of 2.2 to 0.47 nm/sec, respectively. Here, a five- to ten-fold increase in deposition rate was achieved by using a frequency of 70 MHz instead of 13.56 MHz, while maintaining properties well enough to produce highly efficient solar cells. However, it is technically difficult to design plasma deposition systems

for higher frequencies, especially for large substrate areas [181] with dimensions of the plasma area approaching a quarter of the wavelength of the power source [133]. This limits the typical deposition dimensions to less than one meter for a frequency of 70 MHz.

The VHF plasma deposition technique is not only used for the production of a-Si:H, but also for that of microcrystalline silicon (μc-Si:H). At 70 MHz, highly conductive μc-Si:H layers have been deposited [161]. The conductivity of n-type layers is typically between 10 and 100 S/cm and of p-type layers between 0.1 and 10 S/cm for layer thicknesses between 20 and 400 nm. This makes these films candidates to form tunnel junctions in tandem solar cells.

Some properties of VHF deposited films are better than their 13.56 MHz counterparts: the hydrogen content is lower and the films exhibit less internal mechanical stress. But, as remarked earlier, it is technically difficult to scale this technique up to an industrial scale.

Source gases

As a source gas often silane (SiH_4) is used; usually diluted in hydrogen (H_2) to enhance the properties of the material [238, 184, 139]. It is common practice to mix the source gas with methane (CH_4) [5, 219] or ammonia (NH_3) [5] to increase the energy gap of the deposited a-Si:H. By adding germane (GeH_4) to the source gas, an amorphous silicon germanium alloy is obtained, which has a smaller energy gap than pure a-Si:H [152, 210, 84, 260].

Doping the film with phosphorus or arsenic by adding small amounts of phosphine (PH_3) or arsine (AsH_3) to the source gas yields n-type material. Doping the film with boron by adding small amounts of diborane (B_2H_6) or trimethylboron ($B(CH_3)_3$) to the source gas yields p-type material. In all cases the doping efficiency is low due to the fact that most dopant atoms are incorporated according to their optimal coordination. Only a small fraction, in the order of 0.1 to 1 % [206, 207], of the dopant atoms is four-fold coordinated, in which case they contribute to the excess carrier concentration in the material. Of these excess carriers originated from dopants, 90 % are trapped in deep defects, and, of the

remaining 10 %, 90 % occupy localized states near the band edge [204]. Thus 1 % of the excess carriers originated from dopants are in a conducting state above the mobility edge. This gives rise to a doping efficiency in terms of the ratio of free carriers over the total dopant concentration of less than 0.01 %.

Temperature & Substrates

A variety of substrates can be used because of the relatively low deposition temperature of typically 200 to 300 °C. For producing solar cells on an industrial scale, ordinary soda lime glass covered with a transparent conductive oxide is used. However, solar cells can also be produced on, for example, flexible transparent substrates or roofing tiles. For research purposes usually Dow Corning 7059 glass [29] is used because of its high electrical resistivity and optically flat surface. Corning 7059 glass has a high volume resistivity of typically 10^{13} Ωm at 250 °C and a very low alkali content of less than 0.3 %, which minimizes alkali ion migration into the deposited films. The typical surface smoothness is 10 nm, and the surface flatness is 0.004 cm/cm. Also monocrystalline silicon wafers are used as substrates, to facilitate infrared (IR) spectroscopy measurements of the deposited films. Further, ordinary soda lime glass is used for research purposes, to check the influence of the substrate on the properties of the films.

Reactor types

There can be either two electrodes per growth zone (diode type reactor) or three electrodes per growth zone (triode type reactor). In diode configurations, the glow discharge is maintained between two electrodes, one of which serves as the holder for the cell substrate. In triode configurations, the glow discharge is maintained between a solid electrode and a grid. The substrate is mounted beyond this grid on a third electrode. The advantage of the triode configuration over a diode configuration is that short-living, highly energetic particles in the glow discharge do not bombard the growing film, which could result in damage to the film.

The material properties can be controlled by varying the source gas flows, the pressure in the glow discharge, the power density of the discharge, the electrode geometry and the temperature of the substrate on which the film is deposited.

1.5 The deposition system

Thin layers of a-Si:H were prepared in a conventional single-chamber diode-type parallel-plate rf CVD reactor with an rf frequency of 13.56 MHz. A schematic diagram of the deposition system is shown in figure 1.2.

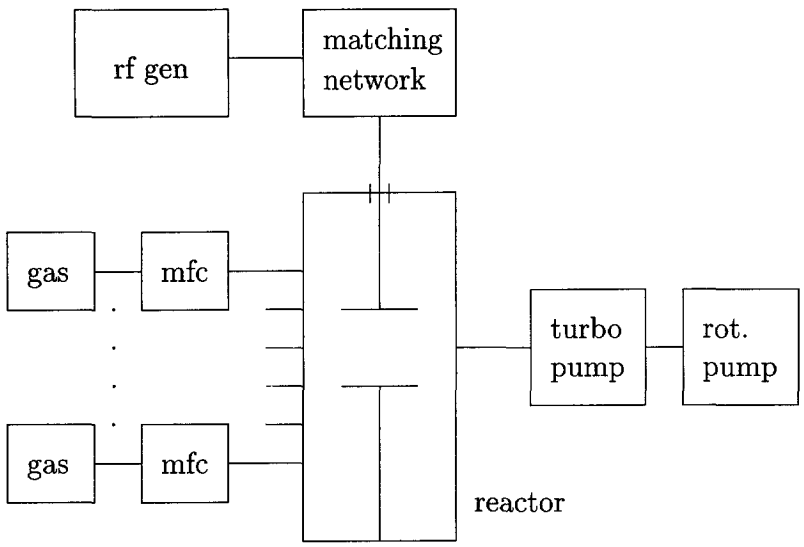

Figure 1.2: *Schematic diagram of the deposition system. The components are denoted by: gas: gas supply, mfc: mass flow controller, rf gen: rf generator and rot. pump: rotation pump.*

The main parts of this system are:

- The stainless steel reaction chamber, fabricated by Samco, model PD 10, with a volume of 17 liters. It contains an upper electrode and a heated, grounded lower electrode, both with a diameter of 18 cm,

separated by 20 mm from each other. The substrate is placed on the lower electrode. To prevent pinholes in the films due to powder which can possibly fall on the films, the upper electrode, on which also deposition takes place, is regularly cleaned.

- The 13.56 MHz rf generator (ENI ACG 5) is connected to the upper electrode through a matching network.
- The gas system was designed in house. The gas flow rates are controlled by Bronkhort F 201C–FA electronic mass flow controllers with an accuracy of 1 %. The maximum gas flow depending on the gas used. (The acronym sccm stands for standard cubic centimeter per minute, 60 sccm equals 1 mbar·lit/sec.)
- The gases used are electronic grade silane (SiH_4), hydrogen (H_2), methane (CH_4) and mixtures of 1 % diborane (B_2H_6) and 1 % phosphine (PH_3) in hydrogen for doping purposes.
- The vacuum pump system, which pumps the reaction chamber, consists of a Pfeiffer TPU 500 turbo molecular pump, with a capacity of 500 l/s, which is pumped by a Balzers DUO 060 A rotation pump with a capacity of 16.7 l/s (60 m^3/h). A total leak plus desorption rate of less than $2.0 \cdot 10^{-6}$ mbar·lit/sec is achieved in this system. At the deposition of an intrinsic film, the total gas flow typically amounts to 40 sccm, which is 0.66 mbar·lit/sec. Thus the contamination due to the leak and desorption is estimated to be less than $3 \cdot 10^{-6}$, whereas the purity of the silane itself is specified as less than $5 \cdot 10^{-5}$.

1.6 Amorphous silicon solar cells

Solar cells convert (sun) light directly into electrical power. There are several types of solar cells, which can use several different semiconductor materials. The materials used are, amongst others, single crystal Si, polycrystalline Si, a-Si:H, GaAs, CdTe and $CuInSe_2$. Because of its cost effectiveness, hydrogenated amorphous silicon has a considerable market share (27.8 % in 1992 [34]) in terrestrial solar power applications. From here on, only hydrogenated amorphous silicon solar cells are discussed.

Structure of the solar cell

Amorphous silicon solar cells can be divided into two categories, viz. single-junction cells and multi-junction cells, also called stacked cells. Stacked cells consist of two or more single-junction cells on top of each other, where the electrical contact between the junctions can be internal (two-terminal devices) or external (multi-terminal devices). Stacked cells consisting of two single-junction cells are generally called tandem cells, while cells consisting of three junctions are often referred as triple cells.

There are several types of single-junction a-Si:H solar cells: p-i-n, n-i-p and Schottky barrier cells. In p-i-n cells the light falls through the p-layer into the i-layer, whereas for n-i-p cells the light comes in through the n-layer. Of the single-junction cells, the p-i-n cell is the most widely used one, because of its high efficiency and stability. Of the stacked amorphous cells, the most popular one is the two-terminal p-i-n-p-i-n tandem solar cell. This cell is schematically drawn in figure 1.3. Typical thicknesses of the layers of a tandem cell are: glass substrate: several millimeters, transparent conductor: 1 μm, doped (p- or n-type) layers: 20 nm, intrinsic layer near the glass substrate: 70 nm, intrinsic layer near the metal back contact: 400 nm, and the metal back contact: several hundred nanometers.

The p-i-n structure is usually deposited on glass coated with Transparent Conductive Oxide (TCO). The TCO serves as a front contact, and is usually textured in order to increase the optical path of the light in the solar cell and to decrease reflection losses. The back contact consists of metal, usually silver or aluminum, which is thermally evaporated onto the n-layer. Silver has the advantage of having a high reflection coefficient, higher than most other metals including aluminum [138]. The high reflection coefficient causes more light to be absorbed in the active part of the solar cell, resulting in a higher solar cell efficiency. However, silver back contacts degrade very fast, typically within days. The high reflectivity combined with the low stability of silver contacts explains the popularity of these contacts in research environments and the absence of silver in commercial solar cells. By inserting a TCO layer between the back n-layer and the silver contact, a TCO/Ag back contact

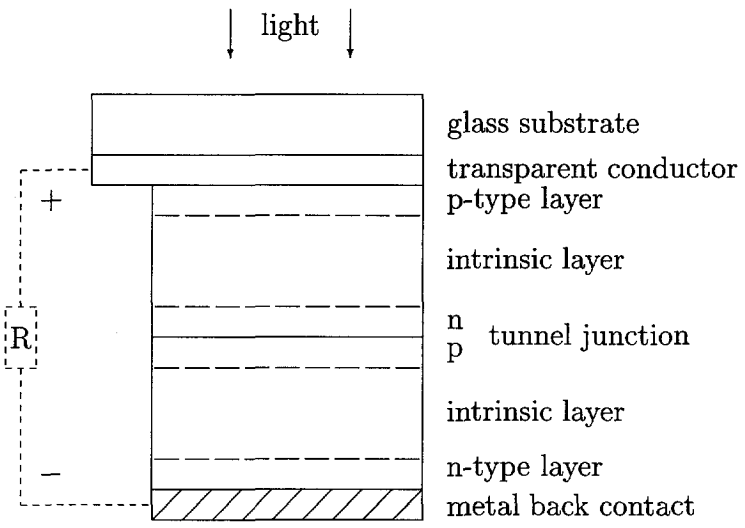

Figure 1.3: *Schematic cross section of an a-Si:H tandem solar cell. Dimensions are not to scale. The external load R is shown dotted.*

is obtained which has a higher reflectivity and a higher stability then a contact consisting of silver deposited directly on the n-type layer [215].

Multi-junction solar cells versus single-junction solar cells

A shift in research and commercial efforts from single-junction cells to multi-junction cells takes place because of the higher efficiency and the lower degradation of the latter. Because in multi-junction cells it is possible to use layers with different optical gaps, the absorption spectrum of the solar cell can be better matched to the light spectrum, and therefore multi-junction cells can achieve higher efficiencies than single-junction cells.

The degradation of solar cells caused by illumination, known as the Staebler-Wronski effect [198, 199], is of major concern in the practical application of solar cells. Compared to single-junction cells, multi-junction cells suffer less from this degradation [129, 130]. The lower degradation

of multi-junction cells is attributable on the one hand to the reduced i-layer thicknesses and on the other hand from a lower illumination intensity of the i-layers. A thinner i-layer causes a higher internal electric field in this layer. Because of the higher electric field, more carriers are extracted before they recombine, and therefore the driving mechanism for defect creation is largely reduced [201]. Also, because of the higher field, an increase in the defect density, and thus a decrease in the mobility-lifetime product of the carriers, has little impact because the mean drift length before recombination is much longer than the layer thickness. In contrast to this, the carrier drift length in single-junction cells is of the same order of magnitude as the i-layer thickness.

Although in tandem cells the second i-layer is not much thinner than the i-layer of a single-junction cell, the second i-layer of the tandem cell shows less degradation than the i-layer of the single-junction cell because the illumination intensity is much less.

Principle of energy conversion

When a p-i-n solar cell is illuminated, the absorption of photons creates free carriers. In general, carrier transport consists of a drift and diffusion component. The photo-generated carriers move through the device under these two influences until they recombine or they reach the contacts, in the last case contributing to the external current. Due to the high defect density of the doped layers, almost all carriers generated in the doped layers recombine in the layer in which they were generated, and thus do not contribute to the external current.

In the intrinsic layer of a solar cell an internal electric field exists, because the i-layer is sandwiched between a p-type layer, where the Fermi-level is close to the valence band, and an n-type layer, where the Fermi-level is close to the conduction band. The energy diagram of such an a-Si:H single-junction solar cell in equilibrium is schematically shown in figure 1.4. Because of this internal field and the sufficiently high free carrier drift length, photo-generated electrons in the intrinsic layer of the solar cell are driven to the n-layer and photo-generated holes drift to the p-layer, thereby generating the external solar cell voltage and current.

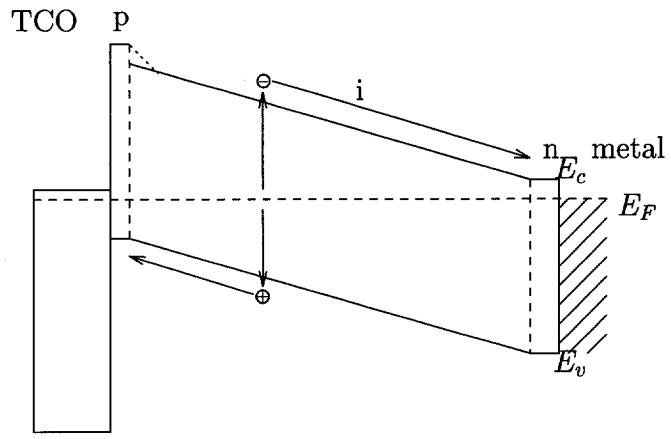

Figure 1.4: *Schematic energy diagram of an a-Si:H p-i-n solar cell in equilibrium.*

The p-type window layer and the p/i interface

In a typical p-i-n solar cell, an amorphous silicon carbide (a-SiC:H) or microcrystalline p-type layer with a wide band gap is used to serve as the front window layer. Because of the lower optical absorption of these p-type materials compared to conventional doped a-Si:H, more light enters the intrinsic layer, in which it can be converted to electrical power. Especially blue light, which has a much higher absorption coefficient than red light, takes advantage of this window layer.

Despite the use of highly transparent window layers, the quantum efficiency of the blue region of the light spectrum is frequently found to be lower than can be accounted for based on the reflection of light at the different interfaces and the optical absorption of the TCO and p-type layer. It is observed that even in solar cells with a thin i-layer, where the electric field is higher, recombination at or near the p/i interface limits the blue response [9]. This recombination is due to the fact that electrons generated close to the p/i interface can diffuse into the p-layer and recombine there. Likewise, holes generated near the i/n interface can be lost in this way. However, because of the much higher carrier generation rate at the front of the solar cell (almost all blue light is absorbed

there), this effect is most pronounced at the p/i interface. Because the band gap of the p-layer is larger than that of the i-layer, the p/i interface represents a heterojunction. To minimize the recombination at the abrupt p/i hetero interface, a graded band gap buffer layer or undoped wide band gap a-SiC:H layer is commonly introduced between the wide band gap p-layer and the i-layer [9, 96]. This buffer layer prevents back diffusion of electrons at the p/i interface, because of the stronger electric field caused by the buffer layer.

1.7 The thesis

This work is aimed to gain knowledge about amorphous silicon solar cells and the amorphous and microcrystalline materials used in these, in order to improve the cost/performance ratio of industrially fabricated a-Si:H solar cells. Because the p-layer and the p/i interface are very critical parts of solar cells, research was conducted into these two aspects of solar cells. Firstly, we investigated the deposition, characterization and optimization of p-type amorphous and microcrystalline silicon based materials for use in solar cells. Secondly, amorphous silicon solar cells were investigated with computer simulations.

Because of the importance of the p-type window layer (it should be as transparent as possible and the Fermi-level should be as close to the valence band as possible), research was carried out to optimize p-type material for use in solar cells. In order to accomplish this, we deposited and characterized several series of p-type films.

Chapter 2 deals with the optical measurements and analysis of the optical properties of thin amorphous and microcrystalline films. The optical analysis gives information on the thickness of the film, the refractive index, the absorption, the optical gap and on the Density Of States (DOS) in the band gap. Different methods to determine the optical gap are described, the gaps of the films were determined, and a relation between the gaps found by the methods was found. Further, of selected films, we determined the DOS with the Constant Photocurrent Method (CPM) and from Dual Beam Photoconductivity (DBP) measurements. The DOS is an influential parameter determining the electrical

properties of the material and therefore it is also an important input parameter in simulations.

Chapter 3 treats the electrical properties of amorphous silicon films in more extent. In particular, the conduction mechanisms and the theoretical backgrounds of the activation energy are treated. The Meyer-Neldel (MN) rule, which is the relation between the prefactor of the conductivity and the activation energy, is also treated. Previous, it was found that amorphous silicon and its alloys obey the MN rule. We show that p-type microcrystalline silicon and its carbon alloys also obey the MN rule.

The p-layer and the p/i-junction are the most critical parts in the single-junction solar cell, because light is entering the cell from the p-layer side. Because of the importance of the p-layer, we deposited several series of p-type material suitable for use in solar cells. Optical and electrical measurements on amorphous and microcrystalline silicon-based materials were carried out, not only to investigate the quality and the suitability of these p-type layers for use in solar cells, but also to obtain a baseline set of parameters for device simulations. The p-type materials were amorphous silicon carbide (a-SiC:H), microcrystalline silicon (μc-Si:H) and microcrystalline silicon carbide (μc-SiC:H).

Chapter 4 describes simulations of solar cells. Further increase in solar cell efficiency is not only expected from technological efforts, but also from computer simulations, because they can point out the solar cell parts which need further optimization. Simulations of devices offer notable advantages over the actual production and measurement of hardware devices: generally they are much cheaper, the impact of small changes of a configuration can be determined much faster and more reliable, and it is possible to examine the influence of input parameters which experimentally cannot be set independently from each other.

The dark and illuminated JV-characteristics of a single-junction solar cell and of a p/i/metal-structure were measured and simulated, in order to establish a baseline set of parameters for the modeling of solar cells, and to determine the band lineup of a experimental p/i-heterojunction structure.

CHAPTER 2

OPTICAL ANALYSIS AND THE DETERMINATION OF THE DENSITY OF STATES OF HYDROGENATED SILICON FILMS

2.1 Introduction

The optical properties of amorphous and microcrystalline silicon are important with respect to the use of these materials in optoelectronic devices like solar cells or photosensors.

For example, the fraction of absorbed light in a layer of a solar cell should be low for doped material and high for intrinsic material in order to obtain highly efficient solar cells with these materials. This is because the doped layers of a solar cell are considered to be non-active layers: the free carriers generated by photon absorption in these layers almost immediately recombine, due to the high defect density of the doped layer, and thus do not significantly contribute to the electrical current of the solar cell. The high defect density of the doped layers arises from the low doping efficiency (see section 1.4), and from this the heavy doping needed to sufficiently move the Fermi level away from midgap.

For the intrinsic layer, which is the active layer of a solar cell, a high absorption coefficient is desirable, because the higher the absorption, the thinner the i-layer can be to achieve a predetermined total absorption. A thinner i-layer is advantageous for two reasons. Firstly, thinner layers suffer less from photo-induced degradation (Staebler-Wronski effect [198, 199]) than thick layers (see section 1.6) [258, 201]. Secondly, due to the limited lifetime of free carriers, the thicker the i-layer is, the more

carriers recombine before they reach the doped layers, and thus the less the current generated by the solar cell.

For these reasons, the optical properties of the doped materials applicable in solar cells were measured. From the optical measurements, not only the optical properties of the material are obtained, but also information on the electronic structure is obtained, because the electronic density of states strongly influences the optical properties of the material. The fact that knowledge about the electronic structure of the material is of major importance for the modeling of a-Si:H devices, strengthens the need to accurately determine the optical properties. The modeling of a-Si:H devices is described in chapter 4.

Further, of films with a thickness between $\sim$ 50 and 1500 nm, the film thickness is conveniently determined from these optical measurements.

To determine the optical parameters for the high energy region, with absorption coefficients above $\sim 10^4$ cm^{-1}, reflection and transmission (RT) measurements were carried out. Which topic is covered in section 2.4. The thicknesses of single thin layers were determined from these RT measurements, as described in section 2.5. The sub band gap absorption, with absorption coefficients smaller than $\sim 10^4$ cm^{-1}, was measured with the Constant Photocurrent Method (CPM) and by Dual Beam Photoconductivity (DBP) measurements, as described in section 2.8.

From the absorption coefficient, two important optical bulk properties of a-Si:H films are derived: the optical gap and the Urbach energy. These contain information on the electronic density of states, and input parameters of electrical simulations are derived from these properties. The optical gap is discussed in section 2.6, and section 2.7 treats the Urbach energy.

From modeling the absorption coefficient, values of the mobility edge, the defect density and the relation between the valence and conduction band tail characteristic energy are derived, which topic is described in section 2.9.

First, the basics of the theory of optical properties and the used experimental setup will be discussed.

2.2 Theory of optical properties

The linear response of a solid to incident electromagnetic radiation with an angular frequency ω is determined by the complex dielectric constant $\tilde{\varepsilon}(\omega)$, where

$$\tilde{\varepsilon}(\omega) = \varepsilon_1(\omega) - i\,\varepsilon_2(\omega). \tag{2.1}$$

More conveniently, the optical properties of a material are given by the refractive index $n(\omega)$ and the extinction coefficient $k(\omega)$, respectively the real and imaginary part of the complex refractive index $\tilde{n}(\omega)$:

$$\tilde{n}(\omega) = n(\omega) - i\,k(\omega), \tag{2.2}$$

which is related to $\tilde{\varepsilon}(\omega)$ by

$$\tilde{\varepsilon}(\omega) = [\tilde{n}(\omega)]^2. \tag{2.3}$$

From relation 2.1, 2.2 and 2.3 it can be easily deduced that

$$\varepsilon_1(\omega) = n^2 - k^2, \tag{2.4}$$

$$\varepsilon_2(\omega) = 2nk. \tag{2.5}$$

Although specifying the same information, more often the absorption coefficient $\alpha(\omega)$ instead of the extinction coefficient is used, where $\alpha(\omega)$ is given by

$$\alpha(\omega) = \frac{\omega\,\varepsilon_2(\omega)}{n(\omega)\,c} = \frac{4\pi\,k(\omega)}{\lambda}, \tag{2.6}$$

where c is the speed of light in vacuum and
λ is the wavelength of the light.

The absorption coefficient determines the fraction of the incident light which is absorbed in a layer. For a layer with thickness d, the intensity of the light at the end of the layer $I(d)$, referred to the incident light intensity I, is

$$I(d) = Ie^{-\alpha(\omega)\cdot d}, \tag{2.7}$$

and the fraction of absorbed light A in the layer equals

$$A = I - I(d) = I(1 - e^{-\alpha(\omega)\cdot d}). \tag{2.8}$$

The absorption of an amorphous film can be deduced from the density of states (DOS). In order to accomplish this, Mott and Davis derived an expression for the photoconductivity of amorphous semiconductors [126]. Under the assumptions that the momentum conservation of electrons is relaxed and the matrix elements for the electronic transitions are constant over the range of photon energies of interest, the photoconductivity of an amorphous semiconductor is given by

$$\sigma(\hbar\omega) = \frac{2\pi e^2\hbar^3\Omega}{m_e^2\hbar\omega}\int [f(E) - f(E+\hbar\omega)]N(E)\,|\,D\,|^2\,N(E+\hbar\omega)\,dE, \tag{2.9}$$

where e is the electron charge,
Ω is the volume of the specimen,
m_e is the electron mass,
$f(E)$ is the probability that an energy level with energy E is occupied,
$N(E)$ is the DOS distribution and
D is the transition matrix element, averaged over all initial and final states.

For electrons, the probability function $f(E)$ is given by the Fermi-Dirac distribution function:

$$f(E) = \frac{1}{1 + e^{(E-E_F)/kT}}. \tag{2.10}$$

The width of the Fermi-Dirac distribution function between the energy level which has a probability of 0.95 to be filled and the energy level with the probability of 0.95 to be empty, $6kT$, equals 0.16 eV at T=300 K. Because energy levels separated by an energy $\hbar\omega$ are considered, where $\hbar\omega$ equals the photon energy which is at least 0.7 eV, equation 2.9 is evaluated at T=0 K, resulting in

$$\sigma(\hbar\omega) = \frac{2\pi e^2\hbar^3\Omega}{m_e^2\hbar\omega}\int N^1(E)\,|\,D(E,\hbar\omega)\,|^2\,N^0(E+\hbar\omega)\,dE, \tag{2.11}$$

where $N^0(E)$ is the empty-state DOS distribution and
$N^1(E)$ is the occupied-state DOS distribution.

The empty and occupied DOS distributions $N^0(E)$ and $N^1(E)$ are given by

$$N^0(E) = [1-f(E)]\, N(E), \tag{2.12}$$

$$N^1(E) = f(E)\, N(E). \tag{2.13}$$

The absorption coefficient $\alpha(\omega)$ corresponding to the photoconductivity given by equation 2.11 is

$$\alpha(\omega) = \frac{4\pi}{n(\omega)c}\sigma(\hbar\omega). \tag{2.14}$$

Thus, the absorption coefficient becomes

$$\alpha(\omega) = \frac{c_\alpha}{n(\omega)\hbar\omega}\int N^1(E)\,|D(E,\hbar\omega)|^2\, N^0(E+\hbar\omega)\; dE, \tag{2.15}$$

where c_α is a constant equal $8\pi^2e^2\hbar^3\Omega/m_e^2c$.

To calculate the absorption coefficient, the matrix element D and the DOS distribution $N(E)$ have to be determined.

For the matrix element D two types are considered, the momentum matrix element P and the dipole matrix element R, which are related to each other as

$$\left(\frac{m\hbar\omega}{\hbar^2}\right)^2 \int N^1(E)\,|R(E,\hbar\omega)|^2\, N^0(E+\hbar\omega)\; dE$$

$$= \int N^1(E)\,|P(E,\hbar\omega)|^2\, N^0(E+\hbar\omega)\; dE. \tag{2.16}$$

The matrix elements P and R depend on the electron energy E, as well as on the photon energy $\hbar\omega$. However, Mott and Davis stated that a statistical average of the matrix elements over the electron energy E can be used, resulting in $P(\hbar\omega)$ and $R(\hbar\omega)$. If the momentum matrix element is assumed to be constant, equation 2.15 yields

$$\alpha(\omega) = \frac{c_P}{n(\omega)\hbar\omega}\int N^1(E)\, N^0(E+\hbar\omega)\; dE, \tag{2.17}$$

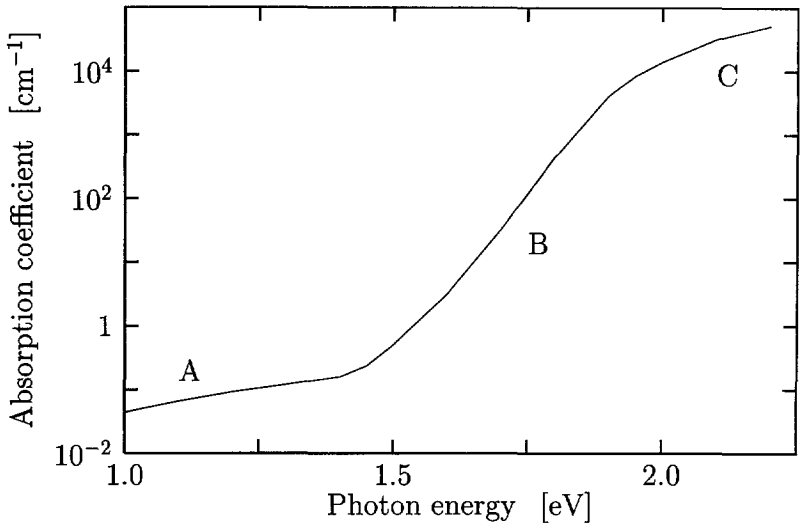

Figure 2.1: *Typical absorption spectrum of amorphous silicon.*

where the constant c_P equals c_α. In the case of a constant dipole matrix element, equation 2.15 gives

$$\alpha(\omega) = \frac{c_R \hbar\omega}{n(\omega)} \int N^1(E)\, N^0(E+\hbar\omega)\, dE, \tag{2.18}$$

where c_R equals $m^2 c_\alpha/\hbar^4$. A constant dipole matrix element was assumed by Spicer to describe the electronic structure of amorphous germanium [197]. If the density of states distribution is known, the absorption coefficient can be calculated from equation 2.17 or 2.18, depending on the model assumed. These equations will be used in section 2.6 to derive a formula to calculate the optical gap from measured absorption data. In section 2.9 the entire DOS will be derived by means of inverse modeling from measured absorption data.

From the equations for $\alpha(\omega)$ and the general form of the DOS of amorphous silicon as shown in figure 1.1, the absorption spectrum takes the form as depicted in figure 2.1. In this absorption spectrum three regimes are distinguished, denoted by A, B and C in figure 2.1 [217, 218]. Region A, the shoulder of the absorption spectrum, is caused by optical transitions involving defect states: excitation from the valence band to

defect-related deep states, and excitation from these defect states to the conduction band. Region B, the exponential rise of the absorption coefficient from ~ 5 cm^{-1} to $\sim 5 \cdot 10^3$ cm^{-1}, is caused by transitions from the valence band tail to the conduction band tail, and was first observed by Wood [254]. Region C, the high absorption region, where the absorption coefficient varies slowly, is dominated by interband transitions, transitions from the extended valence band states to the extended conduction band states.

2.3 Experimental setup of the optical measurements

The experimental setup to measure the reflectance and transmittance of a thin film as a function of the wavelength of the incident light is schematically illustrated in figure 2.2. This setup was also used for CPM and DBP measurements, in order to measure the sub band gap absorption of a-Si:H films.

A 50 W halogen lamp, powered by a computer-driven power supply, is used as a light source. The light of this lamp is focused on the entrance slit of a Spex 1680 B double grating monochromator. This monochromator has a focal length of 0.22 m and the two gratings have 1200 lines per mm and have a maximum reflectivity (are blazed) for photon energies of 0.8 eV. The RT, CPM and DBP measurements are fully computer controlled, including the placing of the order selection filters, which eliminates the need of operator intervention during the measurements.

The light intensity is measured with two-color photodiodes, type K1713–03, manufactured by Hamamatsu. These two-color photodiodes consist of separate silicon and germanium detectors which are mounted one behind the other in a single package. The combined photon energy range of the two-color photodiodes is from 0.7 to 6.0 eV.

The usable photon energy range of the combined RT and CPM or DBP measurement system not only depends on the photodiodes, but also on the spectrum of the lamp and the spectrum of the monochromator. The experimental setup used yields a usable photon energy range from 0.75 to 3.20 eV, depending on the thickness and absorption of the sample. With a high-quality opamp the photodiode current is converted to a voltage

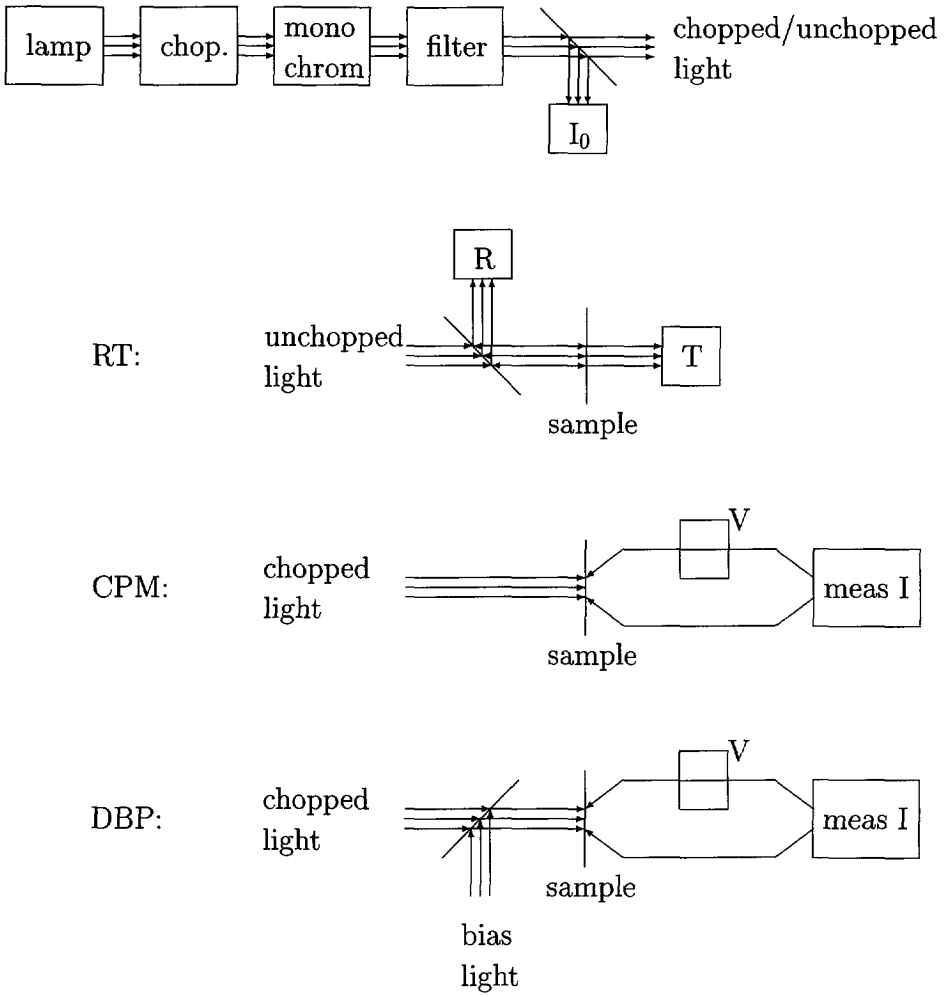

Figure 2.2: *Schematic diagram of the optical measurement system. The light of the lamp can be chopped (chop.) and is made monochromatic (mono chrom.). The filters remove higher-order light of the monochromator and reduce stray light. The detectors are denoted by R, T and I_0, and measure the reflected, transmitted and incident light intensity, respectively. For* CPM *and* DBP*, a voltage is applied on the sample, and the induced current is measured.*

proportional to the intensity of the incident light on the detectors. A computer-controlled multiplexer connects these voltages to a Hewlett Packard 3478 A voltmeter, which is read out by a computer.

The experimental procedure to measure the reflection and transmission of a layer consists of two phases. First, a calibration cycle is executed, and, second, the samples are measured. In the calibration cycle, the signal of the detectors is measured with a bare Corning 7059 substrate placed in the substrate holder. The reflection and transmission of this substrate is calculated from the known refractive index. Combining the measured reflection and transmission of the bare Corning substrate with the calculated reflection and transmission yields the full scale values of the reflection and transmission, i.e. the signal of the detectors in the case where the reflection would be 100 %, and where the transmission would be 100 %. This can be calculated since the voltage of the detectors is proportional to the incident light intensity. After this calibration, the samples of interest are measured.

The reflection and transmission were measured for photon energies in the range of 0.75 to 3.20 eV (1653 to 388 nm wavelength). The thicknesses of the measured layers for these RT measurements are typically between 100 and 1000 nm.

2.4 Reflection and transmission of an optical system

The reflection and transmission of a single interface between two media with different refractive indices are calculated from the Fresnel coefficients. The measurements and simulations were carried out with unpolarized light at normal incidence, in order not to be troubled by the dependence of the reflectance and transmittance on the angle of incidence. For this case, the reflection coefficient of light going from a medium with a complex refractive index $\tilde{n}_0$ to a medium with a complex refractive index $\tilde{n}_1$ is:

$$\tilde{r}_1 = \frac{\tilde{n}_0 - \tilde{n}_1}{\tilde{n}_0 + \tilde{n}_1}. \tag{2.19}$$

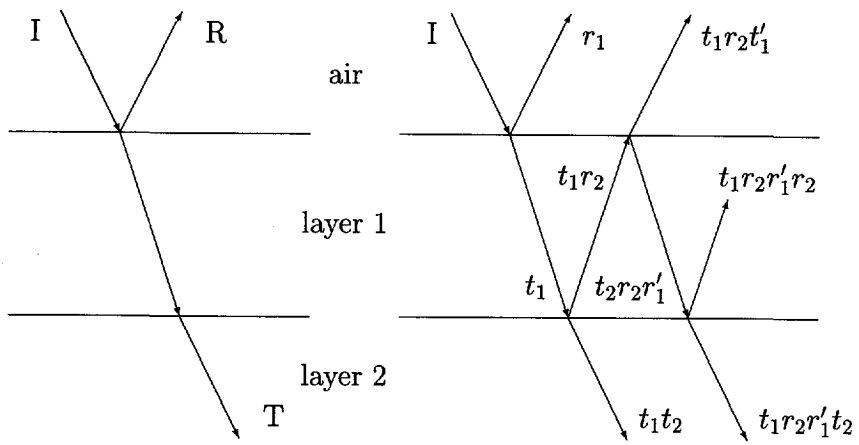

Figure 2.3: *Path of light through a single layer when not dealing with multiple reflections (left) and when dealing with multiple reflections (right).*

The reflection R is given by

$$R = \mid \tilde{r}_1 \mid^2 . \tag{2.20}$$

The transmission coefficient for this case is

$$\tilde{t}_1 = \frac{2\tilde{n}_0}{\tilde{n}_0 + \tilde{n}_1}, \tag{2.21}$$

with the transmission T equal to

$$T = \frac{\tilde{n}_1}{\tilde{n}_0} \mid \tilde{t}_1 \mid^2, \tag{2.22}$$

where $\tilde{n}_l = n_l - ik_l$ for $l = 0, 1$.
The imaginary part of the refractive index accounts for the absorption of the layer, as given by equation 2.6.

To obtain the combined reflection and transmission of a layer, the multiple reflections in the layer are added, as shown in figure 2.3. Two different cases must be considered at adding the multiple reflections. Namely, whether the layer is considered to be coherent or incoherent, which depends on the layer thickness compared to the coherence length of

the light used. The amorphous and microcrystalline films are considered to be coherent, while the glass substrate is considered to be incoherent.

For coherent layers, the amplitudes of the multiple reflections are added to obtain the combined reflection and transmission. For a single layer, absorbing as well as non-absorbing, the combined reflection and transmission coefficients are calculated from the Airy summation, which yield for the reflection coefficient

$$\tilde{r}_{1,2} = \tilde{r}_1 + \tilde{t}_1\tilde{t}_1'\tilde{r}_2 e^{-2i\delta_1} \sum_{k=0}^{\infty} (\tilde{r}_1'\tilde{r}_2 e^{-2i\delta_1})^k = \frac{\tilde{r}_1 + \tilde{r}_2 e^{-2i\delta_1}}{1 + \tilde{r}_1\tilde{r}_2 e^{-2i\delta_1}}, \tag{2.23}$$

and for the transmission coefficient

$$\tilde{t}_{1,2} = \tilde{t}_1\tilde{t}_2 e^{-i\delta_1} \sum_{k=0}^{\infty} (r_1 r_2' e^{-2i\delta_1})^k = \frac{\tilde{t}_1\tilde{t}_2 e^{-i\delta_1}}{1 + \tilde{r}_1\tilde{r}_2 e^{-2i\delta_1}}, \tag{2.24}$$

where

$$\delta_1 = \frac{2\pi}{\lambda} n_1 d_1 \tag{2.25}$$

represents the phase thickness of the thin film. The phase thickness gives the difference of phase of the light at the back of the film compared to the front of the film. The optical thickness is defined as $n_1 d_1$.

The path and the absorption of the light through a system of multiple layers is determined by the complex refractive indices of these layers.

2.5 Determining the layer thickness

The optical parameters are calculated from the measured reflectance and transmittance of the film. Because the film thickness of the samples, typically between 50 and 1500 nm, is comparable to the wavelength of the light used, and the coherence length of this light is much larger than the thickness of the films, interference effects dominate the reflection and transmission. The high refractive index of amorphous and microcrystalline films, in the range of 3.5 to 4.0, enhances reflection at the interfaces and thus amplifies interference effects. Two different methods are available to determine the thickness of the measured films.

The first method makes explicit use of the interference effects: it uses the position of the interference extrema to determine the thickness. Therefore, this method is only useful if a suitable number of interference extrema are recorded. This constrains the measurable thicknesses to a range of typically 200 to 1500 nm.

The second method does not make explicit use of the interference effects and is capable of determining the film thickness of thinner films than the first method, typically down to 50 nm thickness.

Both methods will be described shortly below.

Determining the film thickness from the position of the interference extrema

The thickness of the film is calculated from the distance between the minima and maxima in the reflection caused by interference. A maximum in the reflectance is obtained when the light reflected at the film-air interface is coherent with the light that has traveled one or more times through the film:

$$k \cdot \lambda = 2 n_1 d_1. \tag{2.26}$$

From equation 2.26, the thickness of the films can be found if the refractive index is known. The refractive index can be obtained from the height of the reflection maxima [67]. This method is discussed in more detail by, for example, v.d. Heuvel [67].

Determining the film thickness from the total spectrum

The method to determine the film thickness by using all reflectance and transmittance information uses the analytical expressions derived theoretically for the reflection $R(\omega)$ and transmission $T(\omega)$ of incident monochromatic light on a thin film with thickness d, as described in section 2.4:

$$R(\omega) = f_1(n, k, d; \omega)\,, \tag{2.27}$$

$$T(\omega) = f_2(n, k, d; \omega)\,, \tag{2.28}$$

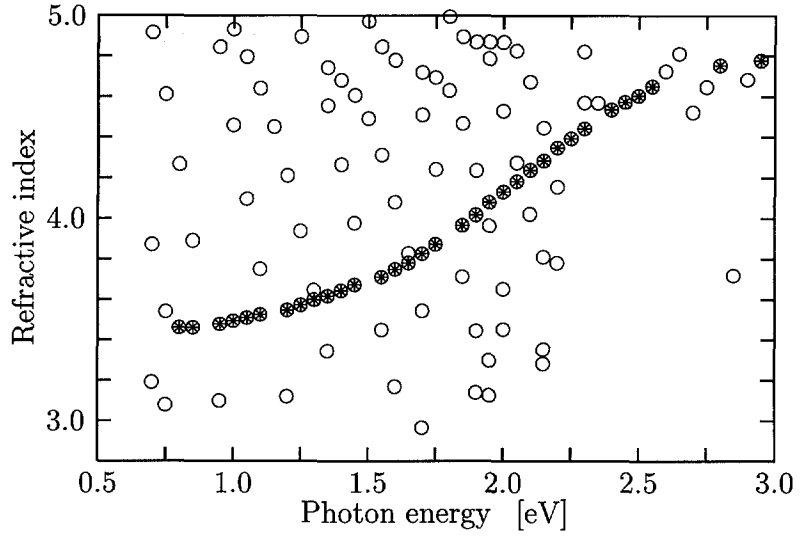

Figure 2.4: *All solutions of (n,k) pairs calculated for the correct thickness of the sample. The (n,k) pairs which constitute the correct physical solution are marked by crosses.*

where $n = n(\omega)$ is the refractive index and
$k = k(\omega)$ is the extinction coefficient.

Measuring $R(\omega)$ and $T(\omega)$ at m different wavelength yields a system of $2 \cdot m$ equations with $2 \cdot m + 1$ unknown parameters. Now a thickness d is chosen and solutions of (n,k) pairs are calculated for every frequency ω. The found values of n are plotted against ω, as shown in figure 2.4, and the thickness d is adapted until a smooth curve is found, because only this smooth curve has physical relevance.

The equations 2.27 and 2.28, consisting of tens of factors if written out completely, are described detailed by Tomlin [225, 226]. The numerical procedure to solve these equations as described above, is an adaptation of the scheme suggested by Denton [35]. More on the procedure has been published by, for example, v.d. Boogaard [15].

2.6 The optical gap

Several methods to determine the optical gap of an amorphous semiconductor has been proposed, and still there is considerable debate on the determination of the optical gap. The different methods will be discussed in the light of the use of the optical gap for simulation purposes.

One of the most direct methods to determine an optical gap is to take the energy at which the absorption coefficient is a predetermined, arbitrary value, where most often 10^4 cm^{-1} is used. This energy gap is denoted by E_{04}. It turns out that an optical gap defined in this way results in gap values which are close to the value of the mobility gap [255]. Thus, although this criterion is rather arbitrary, it delivers information which can serve to compare the transparency of films when other methods to determine an optical gap are too ambiguous. Analogous, the less commonly used E_{05} is defined as the energy at which the absorption coefficient is 10^5 cm^{-1}.

Although not defining an optical gap, the method to judge the transparency of p-type layers according to the absorption at a particular photon energy yield equally valid results. Comparing layers by this method gives rise to meaningful results only if the absorption curves of the different layers are similar. In general, this criterion is more easily be met by comparing layers of the same type, for example p-type a-SiC:H, than by comparing layers of different types. Landweer [89] compared the absorption at 2.3 eV ($\alpha_{2.3}$) of p-type a-SiC:H films with different Si/C ratios to judge the films on their suitability as a window layer for solar cells. The $\alpha_{2.3}$ was successfully used as a measure of the transparency of these layers.

The formal way to determine the optical gap is to extrapolate the linear part of a suitable function of the absorption α plotted versus the photon energy $\hbar\omega$ to $\alpha=0$. What this suitable function can be is derived in the rest of this section. As said before, there are different definitions of the optical gap and different authors have a different point of view as to which function to apply to determine the optical gap.

A short review and a judgement of the different definitions on unambiguity and theoretical description of the semiconductor is given below.

Formal derivation of the optical gap

It is assumed that the DOS distribution of the extended states near the edges of the valence and conduction bands is given by

$$N(E) = \begin{cases} N_{E_V} \cdot \left(\dfrac{E_a - E}{E_a - E_V}\right)^p & \text{if } E \leq E_a \\ \\ N_{E_C} \cdot \left(\dfrac{E - E_b}{E_C - E_b}\right)^q & \text{if } E \leq E_b \end{cases} \tag{2.29}$$

where E_V, E_C are respectively the mobility edges of the valence and the conduction band,
N_{E_V}, N_{E_C} are the density of states at the mobility edges,
E_a, E_b are the extrapolated top and bottom of the extended valence and conduction band distributions and
p, q denote the energy dependence of the extended state DOS.

The optical gap is now defined as the difference between E_a and E_b. The powers p and q denote whether the energy dependence of the extended DOS is assumed to be linear ($p=q=1$) or to be parabolic ($p=q=\frac{1}{2}$). Müller used equation 2.29 with $p=q=\frac{1}{2}$ to model the extended states [127], whereas Klazes assumed linear band edges [83].
The DOS distribution is illustrated in figure 2.5 for a linear extended state distribution and N_{E_V}=N_{E_C}= $4\cdot10^{21}$ cm^{-3}eV^{-1}. Crystalline semiconductors have parabolic band edges, so p=q = 1/2 for these materials. Tauc [216, 217] and Cody [26, 27] assumed that parabolic band edges were also applicable for a-Si:H.

As was discussed previously, two types of the matrix element D exist. From equation 2.17, which describes the absorption for a constant momentum matrix element P, and equation 2.29, describing the extended state DOS, it can be derived that

$$\begin{aligned} \alpha(\omega) &= \frac{c_P}{n(\omega)\hbar\omega} \frac{\Gamma(p+1)\Gamma(q+1)}{\Gamma(p+q+2)} \\ &\quad \times \frac{N_{E_V} N_{E_C}}{(E_a - E_V)^p (E_C - E_b)^q} (\hbar\omega - E_{g,opt,m})^{p+q+1}. \end{aligned} \tag{2.30}$$

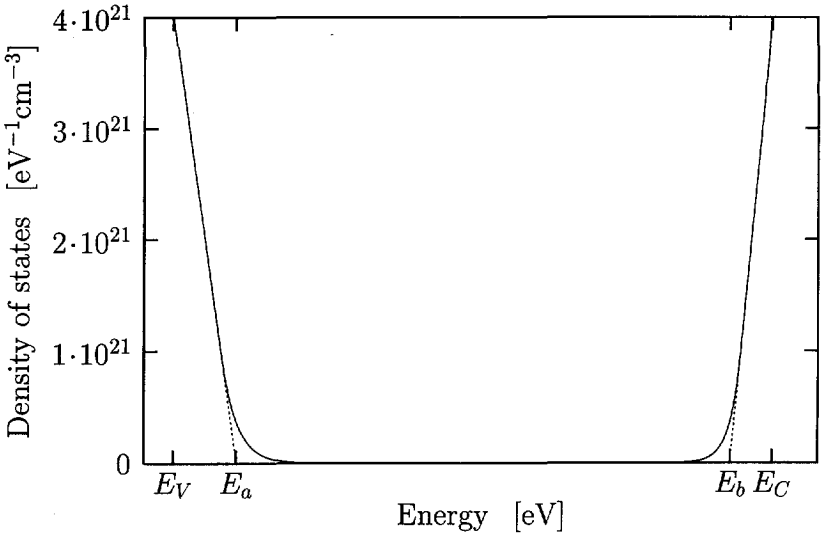

Figure 2.5: *Definition of the band gap for a linear extended density of states distribution. E_V and E_C denote the mobility edges and the optical gap is defined by $E_b - E_a$.*

The analogous expression for the case of a constant dipole matrix element R can be derived from equations 2.18 and 2.29, yielding

$$\alpha(\omega) = \frac{c_R}{n(\omega)\hbar\omega} \frac{\Gamma(p+1)\Gamma(q+1)}{\Gamma(p+q+2)} \times \frac{N_{E_V} N_{E_C}}{(E_a - E_V)^p (E_C - E_b)^q} (\hbar\omega - E_{g,opt,d})^{p+q+1}. \quad (2.31)$$

In section 2.9, equations 2.30 and 2.31 will be used to model measured absorption spectra. For the determination of the optical gap, it is convenient to reduce these equations to

$$\hbar\omega - E_{g,opt,m} \propto [\alpha(\omega) \cdot n(\omega) \cdot \hbar\omega]^{1/(p+q+1)}, \quad (2.32)$$

$$\hbar\omega - E_{g,opt,d} \propto [\alpha(\omega) \cdot n(\omega) \,/\, \hbar\omega]^{1/(p+q+1)}. \quad (2.33)$$

Depending on whether a linear or parabolic extended state distribution is assumed, there are four definitions for the determination of the

Table 2.1: *Different definitions for the determination of the optical gap, with their main author. The third column states the assumed energy dependence of the extended density of states N_{es}.*

model	matrix element assumed const.	$N_{es} \propto$	$\hbar\omega - E_{g,opt} \propto$	main author
A	P	$\sqrt{E}$	$(\alpha n \cdot \hbar\omega)^{1/2}$	Tauc [216, 217]
A'			$(\alpha \cdot \hbar\omega)^{1/2}$	
B	P	E	$(\alpha n \cdot \hbar\omega)^{1/3}$	Klazes [83]
C	R	$\sqrt{E}$	$(\alpha n/\hbar\omega)^{1/2}$	Cody [26, 27]
D	R	E	$(\alpha n/\hbar\omega)^{1/3}$	

optical gap. The four definitions, together with the common practice to omit the refractive index from relation A, are listed in table 2.1.

2.6.1 Influence of the refractive index on the optical gap

The most widely used of these definitions, type A and A', assume a constant momentum matrix element and a parabolic extended state DOS distribution. Also, it is often assumed that the refractive index $n(\omega)$ is constant, which eliminates $n(\omega)$ from the definition of the gap. This assumption is used implicitly in an important review paper by Davis and Mott [33], and in a publication by Tauc [218]. Following these publications, most authors have employed this method [5, 26, 111, 184, 220]. Figure 2.6 shows the $n(\omega)$ for typical amorphous and microcrystalline materials. Over the range where equation A is fitted to obtain the optical gap, for intrinsic a-Si:H typically from 1.85 to 2.25 eV, $n(\omega)$ changes $\sim 10\,\%$ resulting in a change of $\sim 5\,\%$ for the square root of $n(\omega)$. This leads to a difference in the optical gap of ~ 0.01 eV, as is also shown in table 2.2 for various intrinsic a-Si:H samples. Because the Tauc gap can not only differ 0.1 eV depending on the film thickness [26], but it can also change more than 0.1 eV depending on the fitting interval chosen, it is concluded that the difference between type A and type A' concerning the optical gap is negligible.

The third definition, type B, used by Klazes [83] to obtain the optical gap, takes a linear DOS and a constant momentum matrix. Generally,

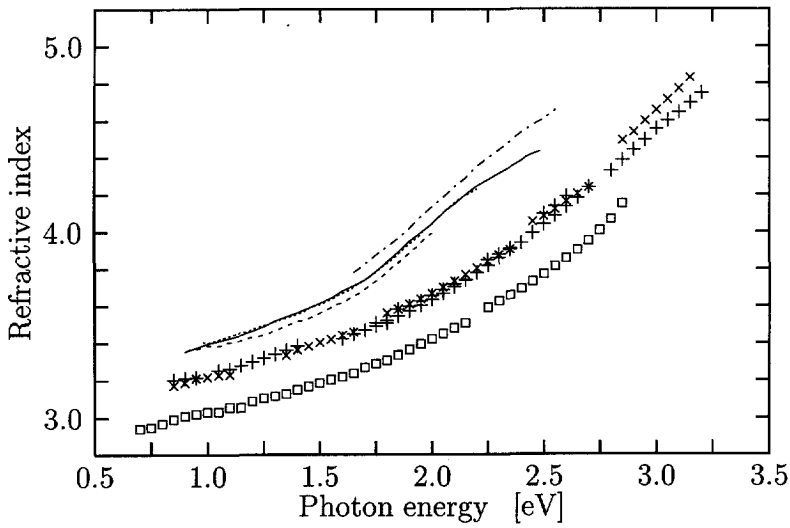

Figure 2.6: *Refractive index of intrinsic amorphous silicon (lines), p-type (+ and ×) and n-type (□) microcrystalline silicon as a function of the photon energy.*

the value of the optical gap found by using this definition is ~ 0.15 eV lower than the value obtained from a Tauc plot. Klazes examined the influence of the omission of the refractive index in equation B. A negligible influence on the linearity of the plot was found, but the band gaps determined from plots without refractive index were 0.05 eV lower than those determined from equation B itself.

2.6.2 Judgement of the various definitions of the optical gap

In order to establish which definition of the optical gap best describes the behavior of amorphous silicon, the values of the gap of different intrinsic a-Si:H samples were determined according to the definitions in table 2.1. The fitting range of the gap types A, A' and D was from 1.85 to 2.25 eV. The definitions type B and C resulted in relations with a much greater straight part of the plot, and the fitting range was therefore chosen from

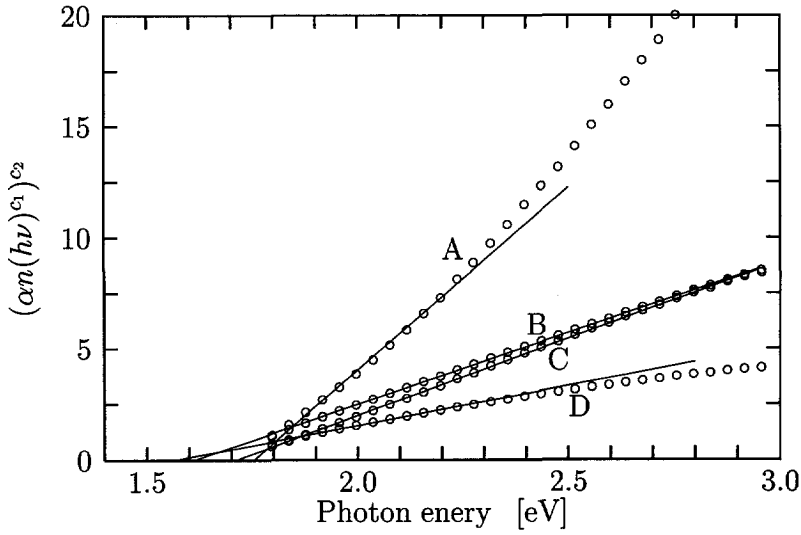

Figure 2.7: *Determination of the optical gap of a representative intrinsic a-Si:H film according to the four methods described in table 2.2. The value of the optical gap can be found from the intersection of the tangent of a curve and the $\alpha=0$ axis. The constants c_1 and c_2 are -1 or $+1$ and $1/3$ or $1/2$ respectively, depending on the gap type.*

1.85 to 2.50 eV. However, the impact of the fitting range on the determination of the optical gap is very small for types B and C. Figure 2.7 shows the fits according to models A, B, C and D for a representative intrinsic a-Si:H film. The results for various other intrinsic a-Si:H films are stated in table 2.2.

As can be seen from figure 2.7, the types B and C result in a plot with the largest straight part. From this, we conclude that these two types are most suitable to determine the optical gap in an unambiguous way. Maessen [105] concluded that type B resulted in a slightly better fit than type C, proceeding from which he suggested using type B to determine the optical gap. However, Jackson found that the dipole matrix element of a-Si:H is constant for energies between 0.6 and 3.0 eV [75], which gives rise to the determination of the optical gap according to type C or D. From which it is concluded that type C, fitting $(\alpha n/\hbar\omega)^{1/2}$, should

Table 2.2: *Optical gap in eV of six intrinsic a-Si:H films determined from the various models.*

model:	A	A'	B	C	D
fit to:	$(\alpha n\hbar\omega)^{1/2}$	$(\alpha\hbar\omega)^{1/2}$	$(\alpha n\hbar\omega)^{1/3}$	$(\alpha n/\hbar\omega)^{1/2}$	$(\alpha n/\hbar\omega)^{1/3}$
120a	1.736	1.725	1.58	1.69	1.52
200b	1.749	1.740	1.58	1.66	1.54
201	1.738	1.728	1.60	1.70	1.53
258	1.750	1.740	1.60	1.69	1.52
535d	1.718	1.707	1.59	1.66	1.50
542d	1.738	1.729	1.61	1.68	1.54

be used to determine the gap. Further, type C delivers values which correspond better to the Tauc values than type B delivers.

As a last remark, it is noted that although the different methods to determine the optical gap yield different absolute values, the relative trends of the band gap as a function of the temperature, different preparation conditions, annealing, ion bombardment after preparation etc. do not so much depend on the chosen model itself. Thus, for relative comparisons, the chosen model has less impact on the results than when absolute gap values are needed, for example, as input parameters for simulations.

2.6.3 Relation between the optical gap values obtained from the various definitions

Figure 2.8 shows the values of the Tauc optical gap (type A) and Klazes optical gap (type B) as a function of the Cody optical gap (type C) of over 200 films, deposited under various conditions by RFCVD. The figure includes data of 85 i-a-SiGe:H films, 36 i-a-Si:H films, 30 p-a-SiC:H films, 4 p-a-Si:H films, 8 n-μ-SiC:H films, 11 n-μ-Si:H films, 16 p-μ-SiC:H films and 35 p-μ-Si:H films.

The optical gaps were determined by fitting the appropriate function, as described in the previous section, for values of α between 2.0 and 20 cm^{-1}. By taking a constant interval of the absorption coefficient,

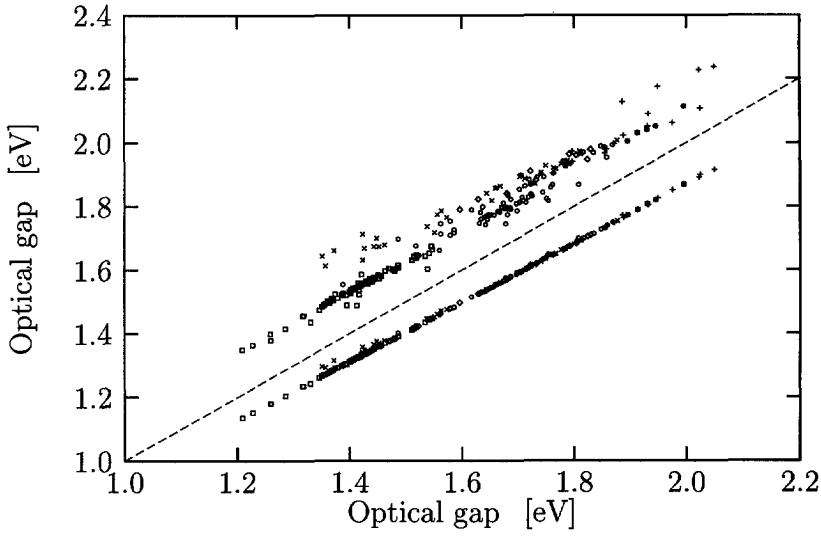

Figure 2.8: *Tauc optical gap (above) and Klazes optical gap (below) as a function of the Cody optical gap. The dashed line denotes the one-to-one relation. The amorphous samples are: doped and undoped silicon and silicon carbide (○) and intrinsic silicon germanium (□). The microcrystalline samples are: p-type silicon (×) and silicon carbide (+), and n-type silicon (∗) and silicon carbide (◇).*

rather than simply taking a constant energy interval, it is guaranteed that the values of the optical gap of films with low gap and high gap are comparable.

It is clear that an unambiguous relation exists between the Cody gap and the Klazes gap, whereas the Tauc gap shows a spread of about 0.2 eV compared to the Cody or Klazes gap. From least squares fitting, the relation between the Klazes optical gap $E_{opt,K}$ and the Cody optical gap $E_{opt,C}$ was determined to be

$$E_{opt,K} = (0.925 \pm 0.003) \cdot E_{opt,C} + (0.017 \pm 0.005)\,, \tag{2.34}$$

whereas the relation between the Tauc optical gap $E_{opt,T}$ and the Cody optical gap was found to be

$$E_{opt,T} = (0.983 \pm 0.044) \cdot E_{opt,C} + (0.168 \pm 0.027)\,. \tag{2.35}$$

These relations yield for a material with a Cody optical gap of 1.66 eV, a Tauc optical gap of 1.80 ± 0.08 eV and a Klazes optical gap of 1.55 ± 0.01 eV.

2.7 The Urbach energy

The optical absorption of all amorphous semiconductors has an exponential energy dependence for photon energies just below the band gap given by

$$\alpha(E) = \alpha_0 \, e^{-(E-E_1)/E_0}, \tag{2.36}$$

where $\alpha(E)$ is the absorption coefficient,
α_0 is a constant,
E_1 is a constant and
E_0 is the Urbach energy.

The parameters α_0 and E_1 were determined experimentally to be respectively $(1.3 \pm 0.4) \cdot 10^6$ cm^{-1} and 2.17 ± 0.02 eV for a large set of intrinsic a-Si:H samples [25]. The exponential tail is called the Urbach edge after its first observation in alkali halide materials by Urbach in 1953 [234]. For a-Si:H, this exponential tail typically occurs for absorption coefficients between 1 and 3000 cm^{-1}. The characteristic energy dependence of the Urbach edge is called the Urbach energy. The origin of the exponential absorption edge is from the joint density of states, which is dominated by the valence band tail because this band tail is much broader than the conduction band tail (see section 1.3). This also gives the importance of the Urbach energy for modeling: it yields the information on the valence band tail characteristic energy. For this purpose, the Urbach energy can be determined from the sub band gap absorption, measured with CPM or DBP.

Because both the Urbach energy and the defect density are a measure of the disorder, a relation between the Urbach energy and the defect density is expected. Indeed, this relation exists, and is discussed in section 2.7.2.

First, the relation between the Urbach energy and the optical gap is treated.

2.7.1 Relation between the Urbach energy and the optical gap

Many material parameters are needed for the modeling of a-Si:H devices. In order to facilitate the modeling and to implement material characteristics in the simulations, relations between parameters are needed. In view of this, the relation between the Urbach energy and the optical gap is discussed below.

Cody et al. concluded that both the optical gap $E_{g,opt}$ and the Urbach energy E_0 are controlled by the amount of disorder in the network [23, 24, 25]. This disorder arises from structural disorder, as well as from thermal lattice vibrations. The dependence of the band gap on the hydrogen concentration [23, 111, 166] is an indirect effect; it arises from the effect of hydrogen on the disorder, which in turn affects the band gap [24].

The temperature dependence of $E_{g,opt}$ and the effect of structural disorder on $E_{g,opt}$ is described by the theoretical relation [3, 24]

$$E_{g,opt}(T,X) = E_{g,opt}(0,0) - D(<U^2>_T + <U^2>_X - <U^2>_0) \quad (2.37)$$

where T is the temperature,
X is a parameter describing the structural disorder,
$E_{g,opt}(0,0)$ is the optical gap at T=0K with no H disorder,
D is the deformation potential,
U is the displacement of the atoms from their equilibrium positions,
$<U^2>_T$ is the average of this displacement due to the non-zero temperature,
$<U^2>_X$ is the contribution of structural disorder to the mean square deviation of the atomic positions from a perfectly ordered configuration,
$<U^2>_0$ is the zero point uncertainty in the atomic positions.

Next, the dependence of the Urbach energy on the displacement of the atoms from their equilibrium positions in a-Si:H must be found. From standard treatments of the Urbach energy in crystalline semiconductors it is concluded that the Urbach energy is proportional to $<U^2>_T$ [218].

The effect of structural disorder on the Urbach energy can be included by adding the contribution from the structural disorder to that of the thermal disorder [25]:

$$E_0(T,X) \propto <U^2>_T + <U^2>_X \ . \tag{2.38}$$

This relation only holds when the thermal disorder (the $<U^2>_T$ term) and the static structural disorder (the $<U^2>_X$ term) have similar effects on the electronic energy levels, which is experimentally confirmed [25].

Combining equations 2.37 and 2.38, while writing $E_0(T,X)$ in terms of $E_0(0,0)$ yields

$$E_{g,opt}(T,X) = E_{g,opt}(0,0) - D <U^2>_0 \left\{ \frac{E_0(T,X)}{E_0(0,0)} - 1 \right\}. \tag{2.39}$$

This linear relationship between the band gap and the Urbach energy was found to be in good agreement with experimental data of a-Si:H samples with different hydrogen contents, measured at different temperatures. The experimental data gives rise to [25]

$$E_{g,opt}(T,X) = 2.108 - 6.067 * E_0(T,X) \pm 0.02, \tag{2.40}$$

where the error is estimated from the difference between the fit and the measured data. Figure 2.9 shows this relation, together with experimental data from samples deposited in our group. The optical gaps shown in figure 2.9 are derived in the same way Cody obtained the optical gap: the Tauc plot was fitted in the high-energy region, for energies up to 3.0 eV, so the values can be compared to relation 2.40. Values of the optical gap derived in this way are ~ 0.07 eV higher than those obtained by fitting for energies between 1.85 and 2.25 eV, as was done for the values shown in table 2.2. It is noted that the coefficients of relation 2.40 should be adapted if another definition of the optical gap is used.

Discussion

In figure 2.9, it is shown that relation 2.40 does not apply to intrinsic a-SiGe:H and intrinsic a-SiC:H. The change in the band gap effected by alloying with germanium or carbon does not result in a change in

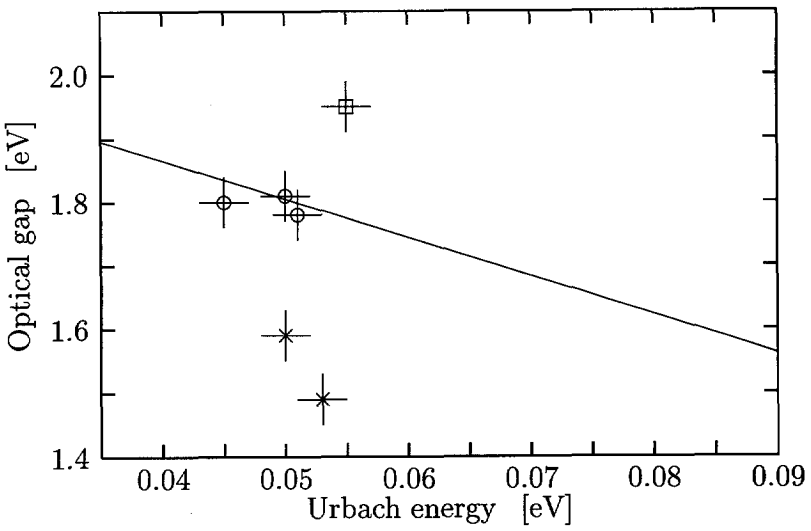

Figure 2.9: *Relation between the optical gap and the Urbach energy, as according to Cody (line), and measured values with error bars of a-Si:H (○), a-SiGe:H (×) samples and a typical a-SiC:H (□) sample.*

disorder which is reflected in the Urbach energy. Street also concludes that a-Si:H samples with a high hydrogen content and high optical gap can be deposited, which do not show a correspondingly reduced Urbach energy [205].

Nevertheless, this model can serve as a tool to couple the optical gap with the valence band tail characteristic energy of the i-layer of a solar cell for modeling purposes, where it must be kept in mind that the model describes the variation in optical gap and Urbach energy as being due to temperature effects or hydrogen dilution, but this model does not apply to alloying with carbon or germanium. It is expected that the coupling between $E_{g,opt}$ and E_0 introduces a trade-off between the electrical properties of the i-layer of a solar cell and its optical absorption. A low defect density, accompanied by a low E_0, is favorable to reduce the recombination of the photo-generated carriers. But relation 2.40 implies an increased optical gap, which lowers the absorption, which is undesirable.

2.7.2 Relation between the Urbach energy and the defect density

The relation between the Urbach energy and the defect density is described below. This relation provides a basis for the coupling of two important input parameters for the modeling of amorphous semiconductors, viz. the defect density in the gap, and the valence and conduction band tail slopes. The relation is found by Stutzmann [209], and was the basis of the defect pool model, which describes the defect creation in a-Si:H from a thermodynamical point of view [177].

Recently, it was suggested that the defect density in a-Si:H may actually be determined by the thermal equilibrium between different configurations within the amorphous network [202, 11, 189, 128]. This thermal equilibrium is thought to be mediated by the movement of hydrogen. However, Stutzmann remarks that the same quantitative relation between the dangling bond density and the band tail slope is valid in the limits of very low (100 K) and very high (900 K) temperatures, which indicates that thermal equilibrium processes are of only secondary importance for the dangling bonds in a-Si:H [209]. For other types of defects, such as neutral defects, the equilibration time is in the order of one year at 300 K in n-type a-Si:H, which makes it clear that an other type of equilibrium is involved [251]. This is chemical equilibrium, which in itself is distinct from thermal equilibrium in that the rate at which equilibrium is reached is bounded by chemical reactions, instead of by phonon interactions.

The concentration of defects states is calculated from the Urbach energy, as proposed by Stutzmann [209]. Stutzmann remarked that irrespective of the substrate, annealing temperature, doping level, impurity concentration and so on, a strong experimental correlation exists between the dangling bond density N_{db} and the Urbach tail slope E_0. This correlation, together with the theoretical relation derived below, is shown in figure 2.10. The figure includes data from undoped, doped and contaminated samples. The undoped samples were deposited in various laboratories with the RFCVD technique [73, 74, 95, 209], annealed up to 650°C [209], deposited with the hot-wire CVD technique [108] and deposited

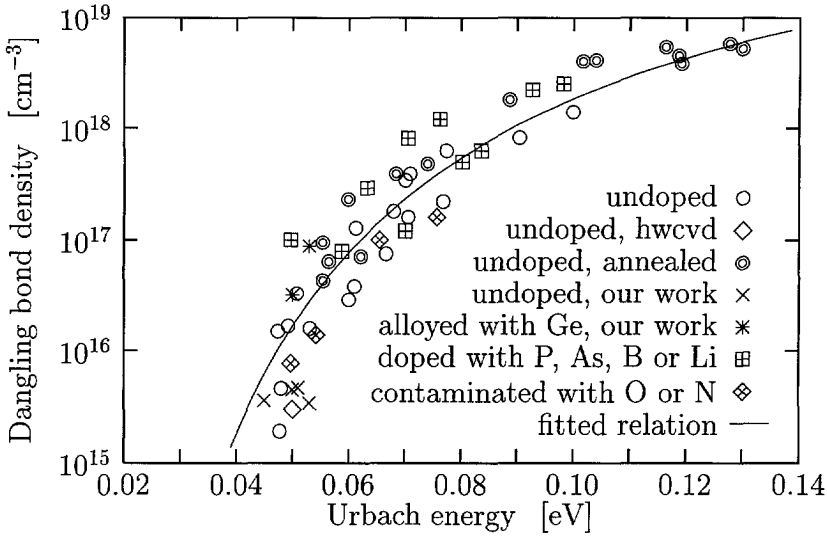

Figure 2.10: *Experimental correlation between the dangling bond density and the Urbach energy in a-Si:H. The line shows the fit of the theoretically derived relation.*

in our own laboratory. The samples alloyed with germanium (Ge) were also deposited in our laboratory. The doped samples were doped with phosphorus (P), arsenic (As), boron (B) or lithium (Li) [209], while the contaminated samples contained oxygen (O) or nitrogen (N) [188].

This correlation is explained with the weak-bond dangling-bond conversion model, in which a few (about 10^{20} cm^{-3} or less) extremely strained bonds in the a-Si:H network are viewed as effective defect molecules in an otherwise rigid lattice. The bonding and anti-bonding levels of these defect molecules give rise to the localized tail states of the valence and conduction band. Under non-equilibrium excitation conditions, excess charge carriers may be trapped in these defect molecules and cause them to dissociate, thereby leading to the formation of metastable dangling-bond defects [208]. With this model, the correlation between the defect density and the Urbach tail slope can be explained with the aid of figure 2.11.

The exponential part of the valence band tail is described by (see

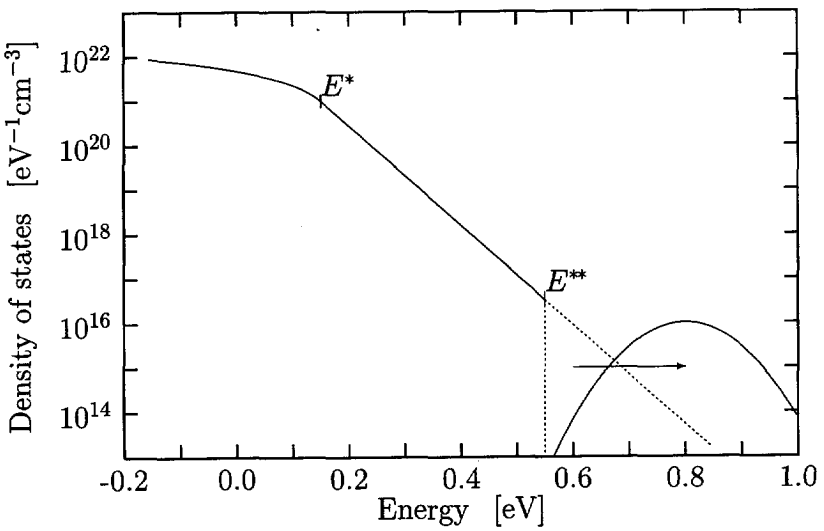

Figure 2.11: *Model for the density of states in a-Si:H. The transformation of valence band tail states into dangling bond states is depicted.*

figure 2.11)

$$N(E) = N^* e^{-(E-E^*)/kT_v}, \tag{2.41}$$

where $N(E)$ is the DOS at energy E,

- N^* is the DOS at the start of the exponential part of the tail
- E^* is the energy where the exponential tail starts and
- kT_v is the characteristic valence band tail energy.

In section 2.9.2, it is shown that for practical applications kT_v can be approximated by the Urbach energy E_0, so equation 2.41 becomes

$$N(E) = N^* e^{-(E-E^*)/E_0} \tag{2.42}$$

where E_0 is the Urbach energy.

This exponential valence band tail does not extend indefinitely towards higher energies, but ends at a critical energy E^{**}. It ends because the deeper the energy level in the gap is, the more the bond is strained, and above a certain bond strain the weak bond spontaneously dissociates,

forming two dangling bonds. The spontaneous formation of dangling bonds is indicated in figure 2.11. Here E^{**} denotes the demarcation energy beyond which the valence band tail states dissociate and form dangling bonds. The dangling bond states may be slightly higher in energy than the unstable tail states owing to the energy gained in the resulting lattice relaxation [209].

Now, the density of spontaneously formed dangling bonds can easily be calculated from equation 2.42:

$$N_{db} = \int_{E^{**}}^{\infty} N \, dE = N^* E_0 \, e^{-(E^{**}-E^*)/E_0}. \tag{2.43}$$

Next, the difference $E^{**} - E^*$ is determined. It is estimated from optical absorption measurements as well as from photoemission measurements that the exponential band tail starts at an energy

$$E^* = E_V + 0.15\,\text{eV} \tag{2.44}$$

The corresponding density of states N^* is approximately $10^{21}\ \text{cm}^{-3}\,\text{eV}^{-1}$ [75, 250]. The demarcation energy E^{**} was determined by Stutzmann by fitting equations 2.43 and 2.44 to experimental data. He found

$$E^{**} = E_V + 0.55 \pm 0.05\,\text{eV}. \tag{2.45}$$

Equations 2.43, 2.44 and 2.45 result for the total number of dangling bonds

$$N_{db} = 10^{21} \cdot E_0 \cdot e^{-0.40/E_0} \tag{2.46}$$

Relation 2.46 is depicted in figure 2.10 alongside the experimental data. Considered the plainness of the theory, the relation shows a remarkably good overall fit. However, if the fit is examined into more detail in the region were the Urbach energy is around 50 meV, it is seen that the relation overestimates the dangling bond density by about a factor of four. Although a factor four is not negligible, it must be considered that an experimental error of a factor two is not unusual at the determination of the defect density in the gap. Also, it is better to think in terms of the logarithm of the defect density (as depicted in figure 1.1), rather than the defect density itself.

2.8 The sub band gap absorption

The Density of States (DOS) in the gap of intrinsic a-Si:H has a strong influence on the electrical and optical properties of this material. It is a crucial parameter for the description of amorphous silicon, and it quantifies the main difference between crystalline and amorphous silicon. Also, from a technological point of view, the determination of the defect density is critical because to produce highly efficient solar cells it is necessary to have intrinsic a-Si:H with defect densities below 10^{16} cm^{-3}. Intrinsic silicon with a defect density higher than $5 \cdot 10^{16}$ cm^{-3} leads to a poor performance when applied in a solar cell. Therefore, the DOS of the used intrinsic material was determined.

The DOS in the gap can be determined by means of several methods, such as the Constant Photocurrent Method (CPM) [56, 235, 236, 237], Deep-Level Transient Spectroscopy (DLTS) [90], Dual Beam Photoconductivity (DBP) measurements [92], Field Effect (FE) measurements [196], Photothermal Deflection Spectroscopy (PDS) [72, 74], by measuring the Space Charge Limited Current (SCLC) [13, 14] and with Thermally Stimulated Conductivity (TSC) measurements [186, 48, 263, 264]. SCLC is a pure electrical measurement: from JV measurements the DOS in a limited regime, typically 0.2 eV width from midgap, can be determined. Also the FE experiment is purely electrical: the conductivity of a film is influenced by applying an electric field normal to the surface of the film, which causes band bending.

CPM, DBP and PDS all measure the absorption of light in the sub band gap regime, from which the DOS can be determined. CPM was originally developed for crystalline semiconductors [56], and applied to amorphous material by Vaněček [235, 236, 237]. Because the recombination kinetics of amorphous silicon are much more complicated than those of crystalline silicon, much theoretical research has been devoted to the application of CPM on a-Si:H [156]. We used two independent methods to determine the sub band gap absorption and from this the DOS of the intrinsic a-Si:H films, viz. CPM and DBP. These two techniques use different methods to handle the problem that the carrier lifetime varies with the carrier concentration and thus with the photon energy.

Table 2.3: *Deposition conditions of the intrinsic a-Si:H films.*

parameter	value	
rf power density	5.9	mW/cm^3
substrate temperature	230	°C
total gas pressure	0.25	mbar
SiH_4 flow	25.0	sccm
H_2 flow	15.0	sccm

Sample preparation

The deposition conditions of the intrinsic layers deposited in the deposition system described in section 1.5, are stated in table 2.3.

The deposition rate of intrinsic a-Si:H films was determined from seven samples, which were deposited over a time period of one and a half years, and amounted to 11.0 ± 0.5 nm/min (95 % confidence region). There was no trend towards a lower or higher deposition rate in this time period.

All amorphous films were deposited with the lowest possible plasma power to maintain a plasma everywhere between the electrodes, because this yields the best films, both in terms of absence of mechanical defects, such as microvoids, as well as in terms of electronic quality, such as a low density of states in the band gap [14, 160, 203]. A power density of 5.9 mW/cm^3 was the minimum power density with which it was possible to maintain a plasma everywhere between the electrodes. With lower power densities the plasma between the electrodes was not homogeneous: the effect of the edges of the electrodes and the non-uniform gas flow became very pronounced.

Keeping all other deposition conditions constant, a 3.3 times increase in power density to 20 mW/cm^3 resulted in a 3.7 times higher deposition rate. This is in agreement with measurements done by van Oort conducted in the same reaction chamber, but with a different gas handling system [139].

The films were deposited on Dow Corning 7059 glass with a size 1.00 $*$ 1.00 $*$ 0.020 inch ($25.4 * 25.4 * 0.51$ cm).

2.8.1 THE SUB BAND GAP PHOTOCONDUCTIVITY OF AMORPHOUS SILICON

The photoconductivity σ_{ph} of an amorphous film is given by [95]

$$\sigma_{ph} = \frac{A \cdot I \cdot e \cdot \eta \cdot \mu \cdot \tau}{d}, \tag{2.47}$$

where A is the total absorption of the film,
I is the incident photon flux,
η is the quantum efficiency for photo-carrier generation,
μ is the drift mobility of the carriers,
τ is the lifetime of the carriers and
d is the thickness of the film.

The absorbed photon flux G_L equals $A \cdot I$. For films which absorb little light, $\alpha \cdot d \ll 1$, the illumination is uniform throughout the film and equation 2.8 reduces to

$$A = \alpha \cdot d. \tag{2.48}$$

Equations 2.47 and 2.48 give

$$\sigma_{ph} = \alpha \cdot I \cdot e \cdot \eta \cdot \mu \cdot \tau. \tag{2.49}$$

If the product $\eta\mu\tau$ is independent of the photon energy $\hbar\omega$, equation 2.49 expresses the possibility to determine the absorption coefficient α as a function of $\hbar\omega$. However, the lifetime τ depends on the number of excess carriers, and therefore on G_L [165]. It was found from experiments that for a-Si:H the relation between the photoconductivity σ_{ph} and the absorbed photon flux G_L is

$$\sigma_{ph} \propto {G_L}^{\gamma} \propto (\alpha \cdot I)^{\gamma}, \tag{2.50}$$

where the value of γ is between 0.5 and 1.0, depending on the material [99, 1, 119]. The exponent γ is independent of the photon flux, but depends on the temperature [193]. The Constant Photocurrent Method and Dual Beam Photoconductivity apply different methods to handle the dependence of $\eta \cdot \mu \cdot \tau$ on the illumination.

2.8.2 Constant Photocurrent Method

In order to normalize equation 2.50, the absorption coefficient at an arbitrary, but constant photon energy, α_0, and the incident photon flux at this arbitrary photon energy, I_0 are defined. Normalization of equation 2.50, by dividing σ_{ph} by $\sigma_{ph,0}$, gives

$$\frac{\sigma_{ph}}{\sigma_{ph,0}} = \left(\frac{\alpha(\hbar\omega) \cdot I(\hbar\omega)}{\alpha_0 \cdot I_0} \right)^{\gamma}. \tag{2.51}$$

In CPM, a sample is illuminated with monochromatic light and the photocurrent caused by this illumination is measured. With a feedback loop the illumination intensity is adjusted to obtain a certain, constant photocurrent, which is the equivalent of keeping the term $\sigma_{ph}/\sigma_{ph,0}$ of equation 2.51 constant. Equation 2.51 then gives

$$\alpha(\hbar\omega) = \frac{c}{I(\hbar\omega)}, \tag{2.52}$$

where the constant c equals $\alpha_0 \cdot I_0$ and can be assessed by a fit of $\alpha(\hbar\omega)$ to values of the absorption at higher photon energies, which are obtained from Reflection Transmission measurements. The photon flux needed to obtain this constant photocurrent is measured as a function of the photon energy. Because the photocurrent is constant, the carrier density and thus the carrier lifetime is constant. In other words: the occupancy of the defect states in the gap is not changed when the photon energy of the incident light is changed.

2.8.3 Dual Beam Photoconductivity

In DBP, the sample is illuminated with white bias light, which is modulated with chopped monochromatic light. The light intensity of the chopped light is much smaller than the bias light in order to consider the values of the parameters which determine the photoconductivity to be determined by the bias light. The advantage of DBP over CPM is the much faster response time and higher signal-to-noise ratio. The current in a DBP measurement is mainly determined by the bias light, whereas the current in a CPM measurement is determined by the low-energy monochromatic light. This gives rise to a response time of DBP

which can be as much as two orders of magnitude faster than that of CPM. The faster response time also results in a better signal-to-noise ratio of the measurements.

The absorbed photon flux consists of two parts, viz. the absorption from the bias light ($G_{L,bias}$) and the absorption from the small chopped fraction, denoted by ΔG_L:

$$G_L = G_{L,bias} + \Delta G_L. \tag{2.53}$$

From 2.50 follows that the change in photoconductivity caused by illumination with the chopped light is proportional to

$$\Delta\sigma_{ph} \sim \gamma \cdot G_{L,bias}^{\gamma-1} \cdot \Delta G_L. \tag{2.54}$$

2.8.4 Measurements on p-type amorphous silicon carbide and intrinsic amorphous silicon

The absorption of p-type a-SiC:H was determined by RT measurements and DBP measurements. For the low energy region, with photon energies below 2.0 eV, three DBP measurements were averaged to obtain the absorption. CPM measurements could not be employed because of the low photosensitivity (ratio of the photoconductivity over the dark conductivity) of doped a-Si:H films. Figure 2.13 shows the results of these measurements on a representative p-type a-SiC:H sample deposited in our laboratory, sample no. 203.

The absorption of intrinsic amorphous silicon was determined by RT measurements, CPM measurements and by DBP measurements. Figure 2.12 shows the combined results of these measurements on a representative a-Si:H sample, no. 186, while figure 2.13 shows the results of these measurements on different samples, deposited under the same conditions.

The Urbach energy E_0 and density of gap states N_{db} was determined from these measurements.

For p-type a-SiC:H, $E_0 = 190 \pm 10$ meV and $N_{db} = (1 \pm 0.5) \cdot 10^{18}$ cm^{-3}, while for intrinsic a-Si:H, $E_0 = 45 \pm 2$ meV and $N_{db} = (5 \pm 2) \cdot 10^{15}$ cm^{-3}.

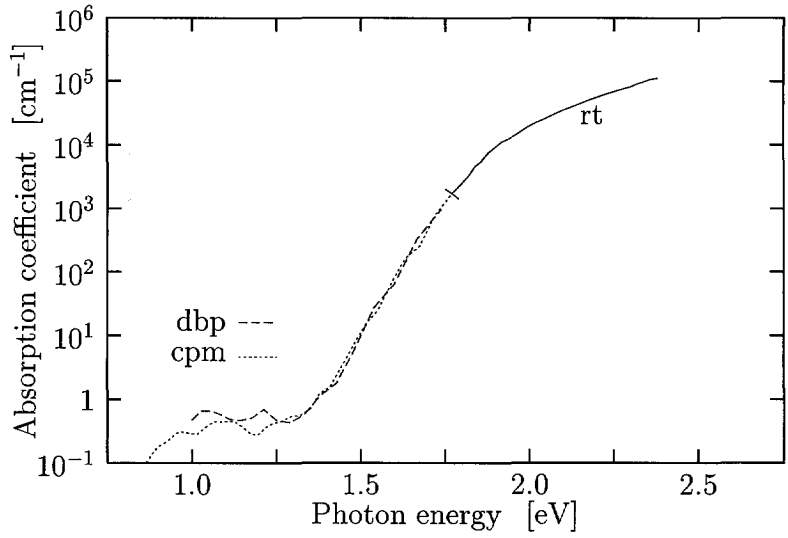

Figure 2.12: *Absorption of a representative intrinsic amorphous silicon film deposited in our laboratory, sample no. 186.*

2.9 Modeling the absorption coefficient of amorphous silicon

The measured absorption spectrum of the intrinsic amorphous silicon films, as shown in figures 2.12 and 2.13, was modeled with equations 2.17 and 2.18. For this modeling, the general shape of the DOS must be known.

The DOS is described by the extended states and localized states, where the localized states consist of the defect states and the tail states. The extended states are given by equation 2.29.

The defects are represented by the two-state model: each defect is represented by a donor and acceptor level. A defect can be in three charge states: positive (empty defect), neutral (defect occupied by one electron) and negative (occupied by two electrons). The donor level, representing transitions between the positive and the neutral state, lies ~ 0.4 eV below the acceptor level, at which transitions between the neutral and negative state take place. The model to describe the distribution of defect states as function of the energy is taken to be a Gaussian distri-

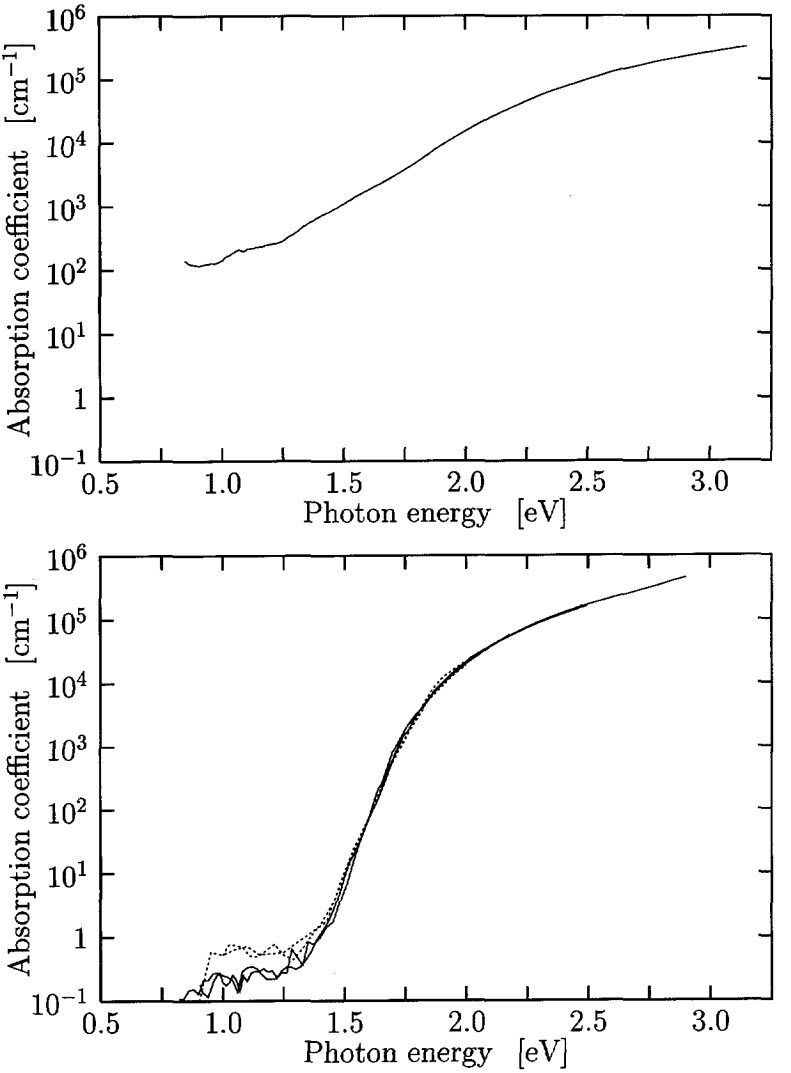

Figure 2.13: *Absorption of representative amorphous silicon films. Above: p-type a-SiC:H, sample no. 203. Below: intrinsic a-Si:H films deposited in our group (no. 120, 186, 201 and 258) and by the Utrecht University (no. 535 and 542). The dotted lines denote films no. 186 and 535, while the rest of the films are shown by unbroken lines.*

bution. Therefore, the defect states are given by two equivalent Gaussian distributions, one representing the donor states, and one representing the acceptor states:

$$N_{db,1}(E) = \frac{N_{db}}{\sqrt{\pi}W} e^{(-(E-E_{db,1})/W)^2}, \tag{2.55}$$

$$N_{db,2}(E) = \frac{N_{db}}{\sqrt{\pi}W} e^{(-(E-E_{db,2})/W)^2}, \tag{2.56}$$

where N_{db} is the total (integrated) defect density,
$E_{db,1}$, $E_{db,2}$ are the positions of the peaks of the distributions,
W is $\sqrt{2}$ times the variance of the distribution.

The valence band tail states N_{vbt} and conduction band tail states N_{cbt} are described by

$$N_{vbt} = N^* \cdot e^{-(E-E^*)/kT_v}, \tag{2.57}$$

$$N_{cbt} = N^* \cdot e^{-(E^*+E_{g,mob}-E)/kT_c}, \tag{2.58}$$

where N^* is the defect density at the mobility edge,
kT_v is the valence band tail characteristic energy and
kT_c is the conduction band tail characteristic energy.

The refractive index used in the simulations was the same as the measured refractive index shown in figure 2.6.

As discussed in section 2.2, three regimes of the absorption coefficient can be distinguished. The high absorption region, determined by transitions between extended states, is described by equations 2.30 and 2.31.

There are four different models, A, B, C and D. Each model describes whether the energy dependence of the extended states is taken parabolic or linear, and whether a constant dipole or constant momentum matrix element describes the optical transition. The models are listed in table 2.1 and have been fitted to experimental data.

Analyzing equations 2.30 and 2.31 gives advance insight into which parameters can be extracted by fitting and which cannot be determined with this method. It can be seen that it is not possible to determine

the constants N_{E_V} and N_{E_C} independently from the prefactor c_P or c_R, which include many physical parameters that are not exactly known, such as the integration volume involved for each transition. Therefore, N_{E_V} and N_{E_C} cannot be determined from these measurements with any useful degree of accuracy.

Also, the differences $E_a - E_V$ and $E_C - E_b$ cannot be determined independently of this prefactor. Therefore, $E_a - E_V$ was taken as twice the distance $E_C - E_b$, which choice is based on physical grounds [205]. Because the mobility gap equals

$$E_{g,mob} = E_C - E_V = E_{g,opt} + (E_a - E_V) + (E_C - E_b), \tag{2.59}$$

it can be found by fitting $E_a - E_V$.

Next, the power p is taken to be equal to the power q, because they are also dependent. Although theoretically it is possible that $p \neq q$, there are no physical indications that $p \neq q$. There is to the author's knowledge no literature assuming that p and q are different.

Also, kT_v and kT_c are dependent. If one tail characteristic energy is known, the other can be determined by inverse modeling. The band tail characteristic energies can be determined from Time-of-Flight measurements, and typical values of kT_v and kT_c of intrinsic a-Si:H are respectively 42 and 27 meV [223, 224]. With total-yield photoelectron spectroscopy [54], Winer found values of kT_v and kT_c of intrinsic a-Si:H of 45 and 30 meV, respectively [249]. Because the valence band tail is broader than the conduction band tail, a change in the Urbach energy will mainly affect the value of the valence band tail characteristic energy. Therefore, kT_c is assumed to be known from other experiments, and the value of kT_v is fitted.

2.9.1 Modeling the high energy absorption region

First, the fitting range was chosen from 1.5 eV onwards, because the validity of the different models can only be assessed in the high-energy region. Fitting for photon energies lower than 1.5 eV does not yield extra information on the validity of the model describing the transitions between the extended states. However, it will increase computation time

Table 2.4: *Fitted mobility gap $E_{mob,sim}$ and valence band tail kT_v for the different models. The conduction band tail characteristic energy kT_c=25 meV. The optical gap $E_{opt,meas}$ is the average value of the optical gaps as listed in table 2.2.*

model	$E_{opt,meas}$ [eV]	$E_{mob,sim}$ [eV]	kT_v [meV]	error $\cdot 10^{-3}$
A	1.74 ± 0.01	1.87 ± 0.01	50.7 ± 0.2	0.85
B	1.59 ± 0.01	1.78 ± 0.01	44.0 ± 1.3	0.24
C	1.68 ± 0.02	1.86 ± 0.01	51.2 ± 1.2	0.43
D	1.53 ± 0.02	1.77 ± 0.01	43.8 ± 2.0	0.56

Table 2.5: *Fitted optical gap $E_{opt,sim}$, mobility gap $E_{mob,sim}$ and valence band tail kT_v for the different models. The conduction band tail characteristic energy kT_c=25 meV.*

model	$E_{opt,sim}$ [eV]	$E_{mob,sim}$ [eV]	kT_v [meV]	error $\cdot 10^{-3}$
A	1.78 ± 0.03	1.81 ± 0.14	50.0 ± 0.2	0.59
B	1.53 ± 0.02	1.81 ± 0.03	45.8 ± 1.0	0.19
C	1.75 ± 0.01	1.79 ± 0.15	48.5 ± 1.6	0.22
D	1.33 ± 0.04	1.82 ± 0.05	47.6 ± 1.2	0.24

considerably. To determine which models describe the measured data best, first the valence band tail characteristic energy kT_v, the mobility gap $E_{mob,sim}$ and the multiplication constant were fitted for the average value of the optical gaps as stated in table 2.2 and a conduction band tail characteristic energy of 25 meV. These average values of the optical gap, together with their 95 % confidence region, are listed in the second column of table 2.4. The errors given for the simulated values are also based on a 95 % confidence region. Table 2.4 also lists the fitted mobility gap and the fitted valence band tail characteristic energy. The results are graphically shown in figure 2.14.

Next, the data was fitted with these values as starting parameters and the optical gap added as a fitting parameter. The results of these fits are listed in table 2.5.

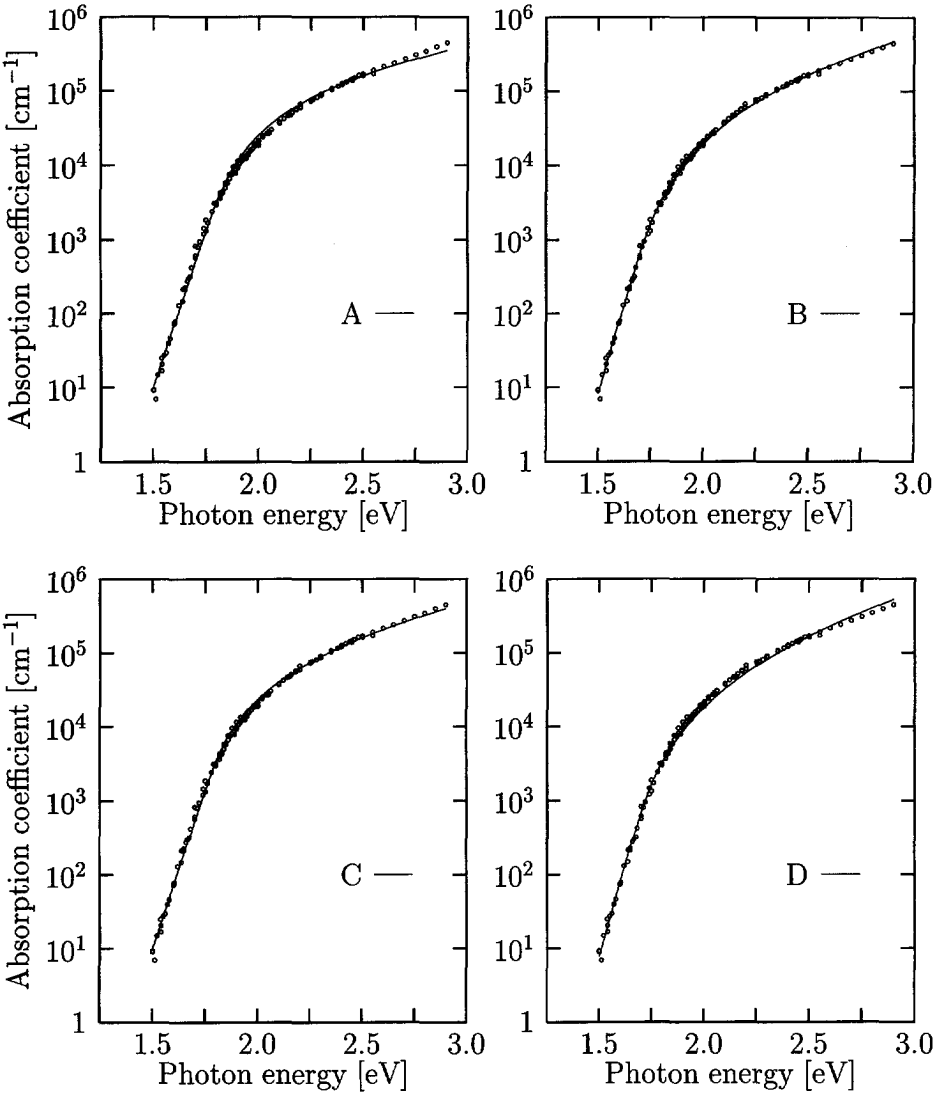

Figure 2.14: *Best fits to measured absorption data with the models A, B, C and D. The optical gap was taken to be constant with values of respectively 1.74, 1.59, 1.68 and 1.53 eV.*

Results

Table 2.4 lists the fitted mobility gap and valence band characteristic energy, with the optical gap fixed at the measured values as stated in table 2.2. Table 2.5 lists these parameters if the optical gap is taken as a fitting parameter too. The difference between the measured optical gap and the optical gap found from inverse modeling, is because the measured optical gap is derived from a limited energy region, typically from 1.85 to 2.25 eV, whereas the simulated one is determined from the total energy region where the absorption is measured. Also, it is clear that the value of the optical gap strongly depends on the applied model. Therefore, it can be concluded that two constraints have to be imposed in order to derive a meaningful optical gap. First, one method should be chosen, and, second, the energy region where equation 2.32 and equation 2.33 are fitted should be chosen to be constant.

From the models A and C, both assuming a constant momentum matrix element, model C describes the measured data best, while from the models assuming a constant dipole matrix element, model B describes the data best. The difference in residual error of $0.19 \cdot 10^{-3}$ by fitting model B, and $0.22 \cdot 10^{-3}$ by fitting model C, is not significant in view of the experimental error of the absorption coefficient, which is estimated to be typically about 3 to 6 %.

The valence and conduction band tail characteristic energies kT_v and kT_c should both have a value smaller than the Urbach energy, which was determined experimentally to be 45 ± 2 meV. For these simulations, the value of kT_v is overestimated, due to the limited energy range. It turns out that the total residual error is minimized when the error at energies near 1.5 eV is not minimal, which results in a simulated Urbach energy larger than the measured one. This problem is circumvented by modeling the total energy spectrum, as is done in the next section.

All four models gave a mobility gap which are the same within the limits of experimental error; the value of the mobility gap is estimated to be 1.81 ± 0.03 eV. This is a strong point of these simulations, because the mobility gap is the electrical parameter of interest; the optical gap only gives additional information on the optical behavior of the material.

Table 2.6: *Two parameters sets of the models B and C, of the modeling of the complete absorption spectrum. The sets for a conduction band characteristic energy of 25 and 30 meV are given. The error χ denotes the quality of the fit.*

model:	kT_c	B	C	
$E_{opt,sim}$	25 meV	1.555 ± 0.005	1.741 ± 0.004	eV
	30 meV	1.562 ± 0.005	1.746 ± 0.004	eV
E_{mob}	25 meV	1.825 ± 0.005	1.771 ± 0.004	eV
	30 meV	1.832 ± 0.005	1.776 ± 0.004	eV
kT_v	25 meV	43.6 ± 0.4	44.9 ± 0.4	meV
	30 meV	42.5 ± 0.4	43.9 ± 0.5	meV
N_{db}	25 meV	$(4\pm1)\cdot10^{15}$	$(2\pm0.5)\cdot10^{16}$	cm^{-3}
	30 meV	$(4\pm1)\cdot10^{15}$	$(2\pm0.5)\cdot10^{16}$	cm^{-3}
χ	25 meV	1.58	1.19	$\cdot10^{-3}$
	30 meV	1.39	1.10	$\cdot10^{-3}$

2.9.2 Modeling the complete energy spectrum

In order to obtain reliable (kT_v,kT_c) pairs and information about the defect density, the complete energy spectrum was modeled. To determine the dependence of the different fitting parameters on kT_c, the inverse modeling was performed for values of kT_c between 17.5 and 37.5 meV, which range is wide enough to cover any realistic value of kT_c. The range is chosen this wide, in order to clearly show the dependence of the parameters on kT_c.

Fits of models B and C to the total energy spectrum of the measured absorption data are shown in figure 2.15 and the relevant parameters found from the simulations are listed in table 2.6. The mean squared error χ denotes the quality of the fit: the lower this number is, the closer the measured points are to the simulated values. The mean squared error is described detailed in appendix A.

Comparison of table 2.6 with table 2.5 reveals that the mobility gap of model C is slightly, about 0.02 eV, lowered by adding the low energy

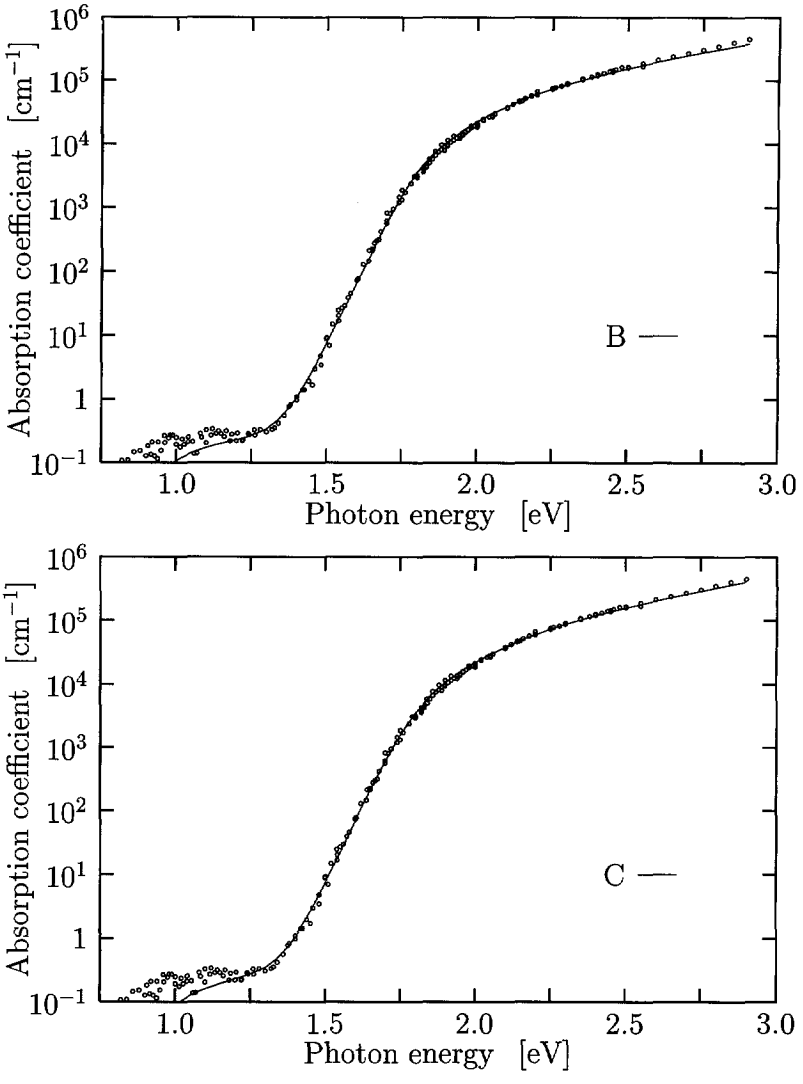

Figure 2.15: *Fits to the total absorption spectrum of intrinsic a-Si:H for model B (above) and model C (below). The measured data is denoted by circles.*

region to the fitting procedure. This is caused by the fact that modeling the complete spectrum introduces a larger total error to be minimized, and the minimum of the total error does not coincide to the minimum of the error at modeling the high energy region. This arises because the model does not perfectly describe the absorption process, especially in the low energy region of the absorption, as can be seen from figure 2.15. Therefore, the mobility gap found from modeling the high energy region is adopted as a more reliable value.

Figure 2.16 shows the dependence of the mobility gap on the conduction band tail characteristic energy. If it is considered that values of the conduction band tail characteristic energy are generally between 25 and 35 meV, the dependence of the mobility gap on kT_c is very modest; less than 0.08 eV between these extremes.

The total density of defect states is independent of the valence band tail characteristic energy, and amounts to $(4\pm1)\cdot10^{15}$ cm^{-3} for model B and to $(2\pm0.5)\cdot10^{16}$ cm^{-3} for model C. Figure 2.15 shows that for photon energies lower than 1.2 eV, the model does not describe the measured data well. Therefore, the defect density obtained from these fits should be used with caution.

Figure 2.16 clearly shows the dependence of the valence band tail characteristic energy on the conduction band tail characteristic energy, which result is also theoretically expected. Assuming a conduction band tail characteristic energy between 25 and 30 meV, which is reasonable, a valence band tail characteristic energy of 43 ± 0.7 meV for model B and 43.5 ± 0.7 meV for model C is obtained. Both values are close to each other and not much smaller than the measured Urbach energy of 45 ± 2 meV. Therefore, taking the value of the Urbach energy for the valence band tail characteristic energy introduces only a small error.

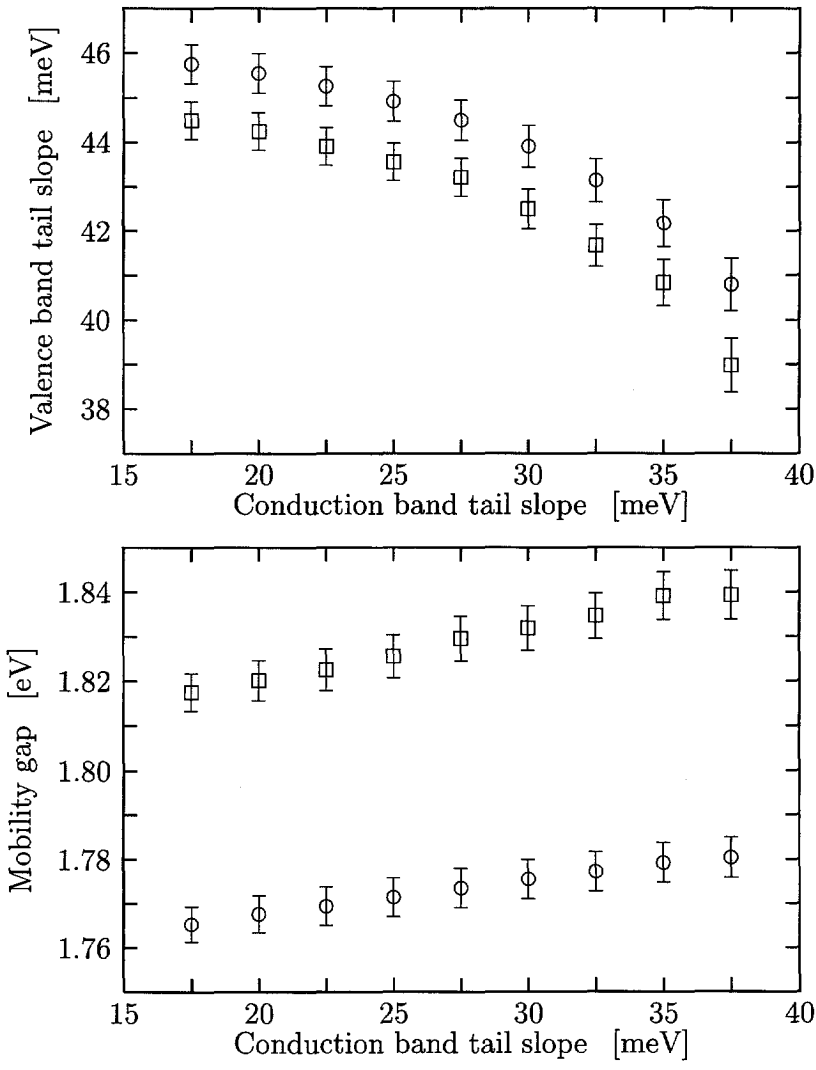

Figure 2.16: *Dependence of the valence band tail characteristic energy (figure above) and the mobility gap (figure below) on the conduction band tail characteristic energy of the models B (□) and C (○). The vertical bars denote the error bars based on a 95 % confidence region.*

2.10 Conclusions

In this chapter, measurements of the optical properties of amorphous silicon and the derivation of optical and electrical key parameters from these measurements have been described. The optical behavior of a material is characterized by the refractive index and absorption coefficient, as described in section 2.2.

We used Reflection & Transmission measurements, the Constant Photocurrent Method and Dual Beam Photoconductivity measurements to determine these optical parameters of thin amorphous films. By combining results from these three methods, the refractive index and the absorption coefficient for photon energies between 0.75 and 3.2 eV was determined. We determined the film layer thicknesses from the RT measurements, which procedure has been described in section 2.5.

A formal derivation of the optical gap is given in section 2.6. Depending on whether a constant momentum or constant dipole matrix element is assumed for the optical transitions, and whether a linear or parabolic energy dependence of the extended states is assumed, the optical gap is derived from one of four different formulas. We conclude that the optical gap derived according to Cody [26] or to Klazes [83] give the best fits. If a constant dipole matrix element is assumed to describe the optical transitions best, as found by Jackson in 1985 [75], the optical gap must be determined according to Cody's method.

Notwithstanding the fact that the definition of the optical gap according to Tauc [217] result in fits which are less good, the most widely used definition of the optical gap found in literature is the Tauc gap, because of historical reasons.

The refractive index is often assumed constant in the determination of the Tauc gap. It was determined that the influence of this simplification is in the order of 0.01 eV, whereas the influence of the fitting range on the the Tauc gap is in the order of 0.1 eV, so the influence of the refractive index on the Tauc gap can generally be neglected.

The relation between the Urbach energy and the optical gap, treated in section 2.7, describes the coupling between these parameters, and it is expected that this coupling implies a trade-off between the electrical

properties of the intrinsic layer of a solar cell and its optical properties. The smaller the defect density of the i-layer is, the lower the recombination, which is electrically favorable; however, it implies a higher optical gap and lower absorption, which is an undesirable effect.

We determined the DOS of intrinsic amorphous silicon from measurements of the sub band gap absorption, done by Constant Photocurrent Measurements and Dual Beam Photoconductivity, as described in section 2.8. The DOS amounted to $(5\pm2)\cdot10^{15}$ cm^{-3}, which value indicates device quality material.

We simulated the absorption coefficient from the DOS, where two types of the optical transitions, and two types of the extended state DOS were assumed. Although the four models yield different values of the optical gap, ranging from 1.33 to 1.78 eV, the mobility gap, found by modeling the high energy region, is the same in all cases, and is estimated to be 1.81±0.03 eV. This is an important result: whereas for optical simulations the optical gap is the determining parameter, electrical simulations use the mobility gap as a input parameter.

It is concluded that of the four possible models, the models corresponding to Klazes' and Cody's methods to obtain the optical gap (model B and model C) describe the absorption data best. The density of defect states found by model B is $(4\pm1)\cdot10^{15}$ cm^{-3}, whereas model C gives a value of $(2\pm0.5)\cdot10^{16}$ cm^{-3}. However, both model B and C do not describe the measured data for low photon energies well, and therefore these figures must be used with some caution. The value found by model B is usually used in electrical simulations of amorphous silicon devices and this results in satisfactory simulations.

The found value of the valence band tail characteristic energy is only ~10 % lower than the Urbach energy, because of the relatively small conduction band tail characteristic energy. The dependence of the optical gap, the mobility gap and the density of defect states on the assumed conduction band tail characteristic energy was found to be negligible. As was expected on theoretical grounds, the value of the valence band tail characteristic energy depends clearly on the assumed conduction band tail characteristic energy.

Chapter 3

Doped amorphous and microcrystalline hydrogenated silicon and silicon carbide

3.1 Introduction

As explained in section 1.6, the doped layers of a solar cell serve to build up the electric field in the intrinsic layer, in order to extract the photo-generated carriers from the i-layer. Light which is absorbed in the doped layers is lost in terms of current production, due to the high density of states in the band gap, acting as recombination centers for the photo-excited electron-hole pairs. For this reason, the doped layers of a solar cell are also called non-active layers, and it is desirable to have the doped layers as transparent as possible. The high density of states in the gap of doped layers originates from the dopant atoms [201].

Maximizing the optical performance of a solar cell

In the commonly used a-Si:H solar cell structures, as described in section 1.6, the light enters through the p-layer. Therefore, in order to minimize optical losses, the front p-layer of a solar cell should be as transparent as possible.

The argument of maximum transparency is also valid for the n- and p-layers which are sandwiched between the two intrinsic layers of a tandem solar cell. Because all incident light falls through the front p-layer, as shown in figure 1.3, optical absorption in this layer is more detrimental to solar cell performance than absorption in the middle p- and n-type layers of a tandem cell.

While all blue light is absorbed before it reaches the back of the solar cell, a significant fraction of long wavelength (>600 nm) light may pass through the intrinsic layer without being absorbed [122]. There are three approaches to increase the absorption in the intrinsic layer.

One way is to increase the thickness of the intrinsic layer of the solar cell. However, a thicker intrinsic layer leads to a decreased electric field in this layer, and thus to a decreased mean drift length of the carriers. Therefore more carriers recombine before they reach the doped layers and a lower current is obtained. Moreover, as explained in sections 1.6 and 2.1, thicker layers degrade faster than thinner layers, thereby decreasing the internal electric field even more, leading to an extra decrease of the current [258]. Thus the overall effect of an increase in thickness above the optimum thickness is a decrease of the solar cell efficiency. The optimum thickness is much smaller than the thickness needed to absorb almost all long-wavelength light.

Another way to increase the absorption in the intrinsic layer is to reflect light that is not absorbed on its first path through the amorphous layers back into the solar cell. A highly reflective back contact supports the optical lengthening of the solar cell while keeping the electrical properties the same [122]. This utilization of the back surface reflection for amorphous silicon solar cells was first proposed for p-i-n solar cells on stainless steel [60, 136]. The back-reflected light should not be absorbed in the back n-layer, which gives rise to the requirement of having a back n-layer which is transparent for long-wavelength light, which requirement is usually easily met.

The third approach is to minimize the total absorption of the doped layers of the solar cell. There are two methods to achieve this. First, the thicknesses of the doped layers can be reduced. However, decreasing these thicknesses beyond a certain minimum thickness results in a decrease of the electric field in the intrinsic layer, resulting in a lower extraction ratio of the photo-generated carriers, and thus in a lower efficiency. The minimum thickness is around 10 nm, depending on how close the Fermi level of the doped layer is to the band edge. Second, the absorption coefficient of the material can be decreased, which can be achieved by, for example, alloying the material with carbon.

Electrical requirements for the doped layers of solar cells

The Fermi level positions of the p- and n-doped layers determine the maximum achievable open circuit voltage, and therefore also the maximum achievable conversion efficiency of a solar cell, as explained in section 1.6. The open circuit voltage is generated mostly near the p/i-interface [58, 59], and is strongly influenced by carrier recombination at the p/i-interface [71, 167].

Besides determining the maximum open circuit voltage of a solar cell, the Fermi level positions also determine the DC conductivity of the doped layers, and thus influence the serial resistance of the solar cell. The closer the Fermi level is positioned to the valence or conduction band, the higher is the electrical conductivity, the lower is the serial resistance, and thus the higher is the short circuit current and fill factor.

For the p-layer of a solar cell, a conductivity of at least 10^{-5} S cm^{-1} is required in order to keep the serial resistance of the window layer negligible [89]. A higher serial resistance of the window layer causes a lower open circuit voltage and lower fill factor. Usually, the conductivity requirements of the n-doped layers are more easily met than those of the p-doped layers, because of the higher doping efficiency of phosphorus compared to boron.

Conclusion

Summarizing, from an optical point of view, all doped layers of a solar cell should be as transparent as possible to maximize the conversion efficiency of the solar cell. At the same time, the layers should have a high dark conductivity and low activation energy. Generally, the optical and electrical requirements counteract: the more transparent the film, the less its conductivity. Insofar as the solar cell efficiency is concerned, the electrical characteristics of the layer are as important as the optical transparency of the film.

Because all light enters through the front p-layer, this layer is the most crucial doped layer of the solar cell. Of the interfaces, the p/i-interface is the most important solar cell interface.

3.2 General description of the doped materials

Historically, the first p-layers used in solar cells were heavily boron doped a-Si:H layers [17, 18, 102, 135]. The disadvantage of these layers is the high optical absorption caused by the heavy boron doping [19, 101, 231], limiting the maximum efficiency of the solar cell.

There are two common methods to decrease the absorption of the p-type material. First, the a-Si:H can be alloyed with carbon [219, 221], and second, instead of amorphous material, microcrystalline material can be used [111]. Also research has been carried out in combining these two approaches to obtain high-quality microcrystalline silicon carbide.

The advantage of doped microcrystalline silicon over doped a-Si:H, is the much higher possible dark conductivity, and thus a Fermi level position closer to the band edge, resulting in a higher open circuit voltage of the solar cell.

3.2.1 Doped hydrogenated amorphous silicon carbide

Adding carbon to a-Si:H increases the band gap of the material. The widened band gap is the reason for the application of amorphous silicon carbide (a-SiC:H) as p-layers in solar cells, which was a breakthrough in solar cell performance [219, 221]. However, incorporation of carbon in a-Si:H not only widens the band gap, but simultaneously shifts the Fermi level away from the band edge. This Fermi level shift can be experimentally observed by a decrease of the electrical conductivity and an increase of the activation energy of the electrical conductivity [220] and arises from the increasing DOS in the gap [174], resulting that more carriers originating from the dopant atoms are trapped [121]. Because the incorporation of carbon has an opposite effect on the optical properties versus the electrical ones of the film, the carbon content of the films must be optimized to obtain optimal films for use in solar cells.

In order to establish the deposition parameters of the deposition system for p-type silicon carbide films suitable as a window layer in solar cells, a series of films have been deposited, under varying deposition conditions.

3.2.2 Doped hydrogenated microcrystalline silicon

Microcrystalline silicon (μc-Si:H) films can be deposited with the same deposition technique used to produce a-Si:H films, which makes microcrystalline material along with amorphous material suited to the production of large area devices. Because of the favorable properties of microcrystalline material, it is used in commercial applications such as solar cells, thin film transistors [79, 80] and pressure sensors.

Microcrystalline films lie on the borderline between the amorphous and the polycrystalline phase: in general, they are composed of small crystallites embedded in an amorphous matrix. The existence of this amorphous matrix is due to deposition conditions just near the transition from amorphous to microcrystalline growth. Vepřek ascribes this two-phase system to deposition too far from partial chemical equilibrium (PCE) [241, 242, 244]. The term PCE was introduced by Wagner [243] to indicate a state with vanishing chemical fluxes, but remote from thermodynamical equilibrium [239, 243]. Thermodynamic equilibrium corresponds to a state with vanishing values of the thermodynamic fluxes such as energy and mass. Similar, vanishing chemical fluxes characterize chemical equilibrium. PCE is a chemical kinetic steady state, added with the condition that the chemical fluxes vanish, so there no net etching or deposition occurs. At PCE, the actual concentrations of the reactants and products are given by the balance of their formation and decomposition, with a negligible flow term. Microcrystalline films without detectable amounts of amorphous tissue, less than 1 %, are obtained if the difference of the deposition and etching rates, which is the growth rate, is small compared to the etch rate. The grain size is usually determined by X-ray or electron diffraction methods and varies typically from 3 to 20 nm.

The optical as well as electrical properties of μc-Si:H are clearly distinct from crystalline or amorphous silicon. The optical gap of microcrystalline material can be raised to about 2.0 to 2.2 eV [45, 69], as can be done with a-SiC:H. But, in contrast to a-SiC:H, this gap does not narrow upon doping [111]. Also in contrast to a-SiC:H, the conductivity of films with such high band gaps remain high, while that of amorphous

films drop to values comparable to that of intrinsic a-Si:H.

Fully crystallized microcrystalline material is intrinsically defect rich due to the large number of internal surfaces or interfaces, which result in interface states at the grain boundaries [247]. Microcrystalline surface states may be hydrogen passivated to a large degree, because glow-discharge prepared microcrystalline silicon typically contains 5 to 15 at. % hydrogen. Nevertheless, a silicon grain boundary trapping state distribution of 10^{11} $cm^{-2}eV^{-1}$ still leads to an effective volume density of states of 10^{17} $cm^{-3}eV^{-1}$ for a crystallite size of 10 nm. This is a high value, compared to intrinsic amorphous material which has a density of states lower than 10^{16} $cm^{-3}eV^{-1}$ [247]. The high density of states in doped layers is desirable, because it prevents light-induced degradation of the doped layers from taking place.

3.2.3 Doped hydrogenated microcrystalline silicon carbide

With a special technique, Electron Cyclotron Resonance (ECR) CVD, p-type microcrystalline silicon carbide (p μc-SiC:H) films can be deposited which have optical and electrical properties outperforming those of p-type μc-Si:H films deposited by conventional RFCVD [62, 64, 65]. Highly transparent, highly conductive p-type μc-SiC:H has been prepared with this technique: typical values of the dark conductivity σ_d and the Tauc optical gap $E_{g,opt}$ are σ_d=1 S cm^{-1} at $E_{g,opt}$=2.0 eV and $\sigma_d = 10^{-2}$ S cm^{-1} at $E_{g,opt}$=2.8 eV. The suitability of this material for use in solar cells was also demonstrated [62, 64, 65]. An a-Si:H solar cell implementing an ECR p-type μc-SiC:H layer with σ_d >1 S cm^{-1} and $E_{g,opt}$=2.25 eV showed a conversion efficiency of 12.0 %, measured under AM1 illumination [62]. The cell had a very large open circuit voltage V_{oc} of 0.967 V, a short circuit current density J_{sc} of 17.7 mA/cm^2 and the fill factor FF amounted to 0.703. A comparable cell with an RFCVD p-type a-SiC:H layer showed an V_{oc} of 0.875 V, a J_{sc} of 17.8 mA/cm^2 and an FF of 0.660. Thus the increase in efficiency is mainly attributable to the higher V_{oc}, which in turn is primary caused by an increase in the built-in potential [132].

Notwithstanding the good results obtained with the application of ECRCVD p-type layers in solar cells, the ECRCVD technique is difficult

Table 3.1: *Deposition conditions of the silicon layers.*

material	p a-Si:H	p μc-Si(C):H	n μc-Si(C):H	
rf power density	5.9	195	195	mW/cm^3
substrate temp.	230	200	200	°C
gas pressure	0.25	1.00	1.00	mbar
SiH_4 flow	25.0	4.0	4.0	sccm
H_2 flow	20.0 – 35.0	95.0	95.0	sccm
B_2H_6 flow	0.05 – 0.20	0.025	–	sccm
PH_3 flow	–	–	0.025	sccm
CH_4 flow	0 – 40	0.0 – 0.5	0.0 – 0.5	sccm

to scale up to an industrial scale, and therefore the practical value of this technique is limited. Thinking in terms of the mass production of devices, the conventional RFCVD process is from a technological point of view to be preferred to ECRCVD. Because of this consideration, doped microcrystalline silicon carbide films deposited by RFCVD were investigated [229].

3.3 Sample preparation

Amorphous silicon carbide (a-SiC:H), microcrystalline silicon (μc-Si:H) and microcrystalline silicon carbide (μc-SiC:H) films were deposited by PECVD in the single chamber deposition apparatus described in section 1.5. Silane was used as a silicon source, while p- or n-type doping was achieved by adding a gas mixture consisting of 1 % diluted diborane or phosphine in hydrogen. A strong hydrogen dilution and high rf power were used at the deposition of microcrystalline silicon [240, 117, 112, 232]. The general deposition conditions of these materials are listed in table 3.1.

Doped hydrogenated amorphous silicon carbide

The amorphous silicon carbide (a-SiC:H) layers were deposited on Dow Corning 7059 glass substrates. The flow of the dopant gas mixture was

varied between 5 and 20 sccm, resulting in a source gas mixture containing 0.02 % to 0.3 % diborane, depending on the dopant gas and methane flows. Because the dopant gas mixture consisted of 99 % hydrogen, the source gas became more diluted by the addition of more dopant gas, and consequently the growth rate went down. The growth rate of the films varied from 15 to 20 nm/min, depending on the dopant gas flow. To eliminate the band gap narrowing caused by boron doping, carbon was incorporated into the films, by adding up to 40 sccm methane to the source gas. Samples without carbon were deposited as a reference.

The deposition time of all p-type silicon carbide films was 15 min, which is long enough to ensure that the properties of the deposited layers are dominated by the bulk.

Doped hydrogenated microcrystalline silicon

A high rf power density and a high hydrogen dilution were used to produce microcrystalline films [140, 227]. Because the doped layers in solar cells are deposited on amorphous material, rather than on bare glass, and the properties of microcrystalline material depend on the substrate, the films were deposited on Dow Corning 7059 glass as well as on glass coated with 100 nm intrinsic a-Si:H, in order to investigate the influence of the substrate on the properties of the microcrystalline films. The microcrystalline films were also deposited on monocrystalline silicon substrates for the determination of the crystallite size of the films by means of X-ray diffraction spectroscopy. The crystallite size, as determined from the experimental data shown in figure 3.1, was 9.4 nm for the p-type layers and 12.3 nm for the n-type layers.

Doped hydrogenated microcrystalline silicon carbide

As a carbon source, up to 0.5 sccm methane was added to the source gas mixture which was used to produce μc-Si:H films, in order to obtain microcrystalline silicon carbide films. The methane to silane ratio was varied from 0 to 1/7, so the total spectrum from pure microcrystalline silicon via microcrystalline silicon carbide to a-SiC:H was investigated.

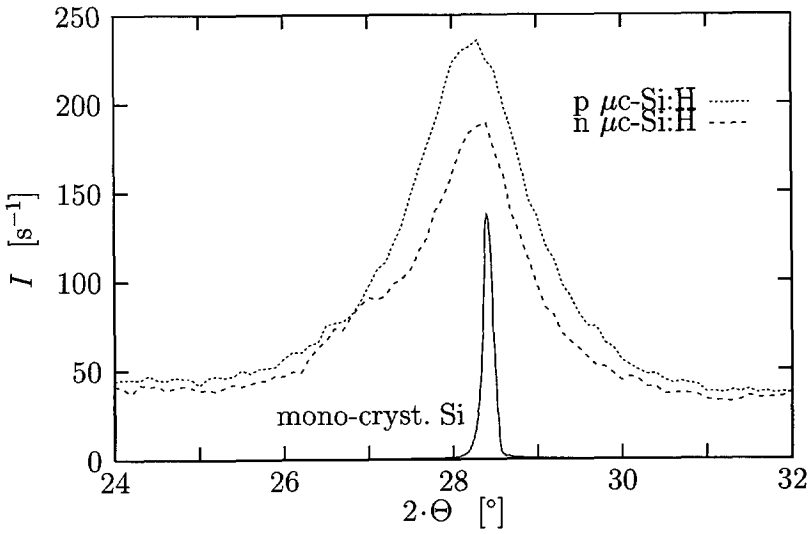

Figure 3.1: *The X-ray diffraction intensity I in counts per second as a function of the scattering angle* $2 \cdot \Theta$ *of μc-Si:H. The signal of the monocrystalline silicon substrate is displayed 100 times reduced.*

The deposition time of all films was 20 min, resulting in thicknesses of 110 to 135 nm for the p-type silicon carbide films and 65 to 75 nm for the n-type films, corresponding to growth rates of respectively 6.1 ± 0.6 nm/min and 3.50 ± 0.25 nm/min. The growth rate decreases with increasing methane content of the source gas. The films deposited with methane concentrations above 8 % for p-type and 12 % for n-type films were not microcrystalline.

3.4 Optical and electrical measurement methods

The thickness, absorption and the optical gap of the layers were determined as explained in chapter 2. The typical error of the absorption coefficient is $\sim 5 - 10$ %, whereas the typical error in the optical gap is ~ 0.1 eV. The growth rates were determined by dividing the thickness by the deposition time, which procedure neglects the possible influence of the substrate on the deposition of the first few nanometers of the film.

The optical gap is obtained from a Tauc plot. Because the Tauc plot is generally slightly curved upwards, as discussed in section 2.6.2, the optical gap is obtained by fitting all plots in the energy region of 1.85–2.25 eV, in order to obtain a meaningful value for the optical gap.

The electrical conductivity σ of the films was determined by means of the four-point probe technique [158, 169] for films with $\sigma > \sim 10^{-5}$ S cm^{-1}. The conductivity of films with $\sigma < \sim 10^{-5}$ S cm^{-1} was determined from the resistance measured between two parallel metal electrodes on the film. These thermally evaporated contacts were 20 mm long and separated by 0.5 mm. A Keithley 617 Electrometer was used to apply an electric field of $2 \cdot 10^3$ V/cm and to measure the current caused by this field. It was verified that the contact behavior was Ohmic.

Also, of a number of selected samples, the temperature dependence of the dark conductivity was measured.

The photoconductivity was measured by illuminating the samples with light with AM1.5 spectrum and an intensity of 100 mW/cm^2, obtained from an Oriel model 81150 solar simulator.

3.5 Measurements on the doped materials

3.5.1 Doped hydrogenated amorphous silicon carbide

Figure 3.2 shows the growth rate of the p-type a-SiC:H films as a function of the methane and dopant gas flows. There is no significant dependence of the growth rate on the methane flow. However, the dependence on the hydrogen flow, which amounts to 100 times that of the diborane flow, is significant, as shown in figure 3.2. From least squares fitting, the growth rate in nm/min equals $(21.9 \pm 2.7) - (0.38 \pm 0.2) \cdot \phi_{H_2}$, where ϕ_{H_2} denotes the hydrogen flow in sccm. This relation is shown in figure 3.2. Comparing figure 3.2 to 3.3 shows there is no dependence between the growth rate and the optical or electrical properties.

The absorption coefficient at 2.3 eV, $\alpha_{2.3}$, and dark conductivity σ_d as functions of the diborane and methane gas flows are shown in figure 3.3. By increasing the dopant gas flow, the films become less transparent, whereas increasing the methane flow has the opposite effect on

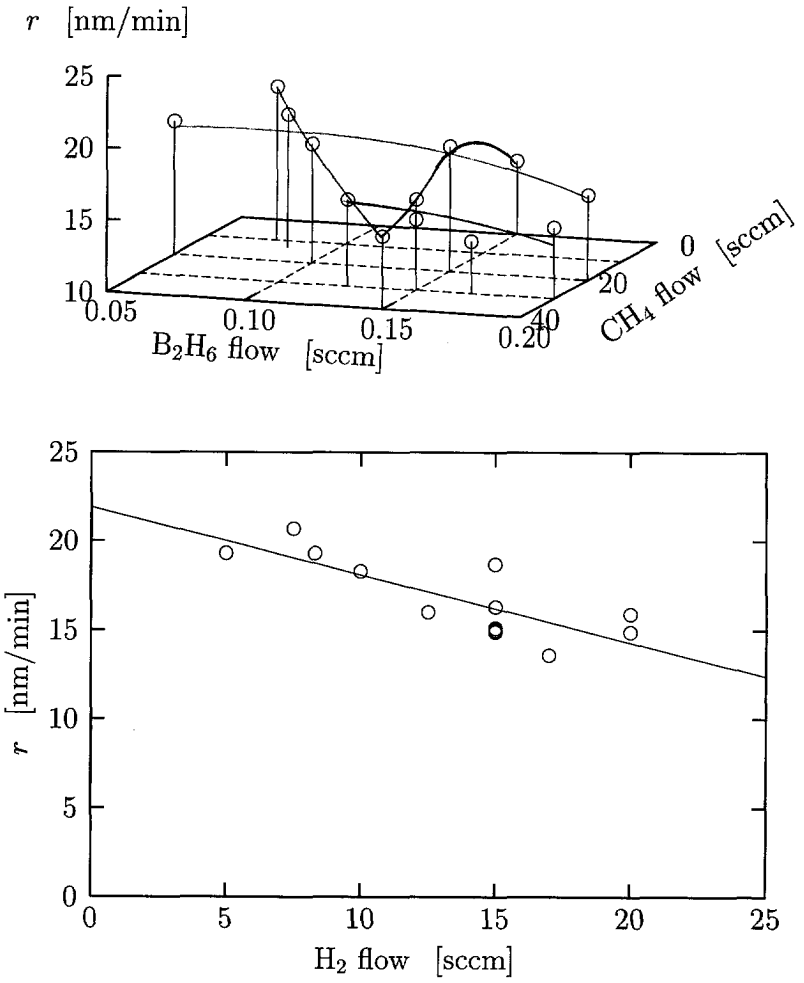

Figure 3.2: *Growth rate r of p-type a-SiC:H films as a function of the gas flows. Above: growth rate as a function of the diborane and methane gas flows. Below: growth rate as a function of the hydrogen gas flow. The hydrogen flow amounts to 100 times that of the diborane flow. The line in the figure below denotes the best fit as obtained from least squares fitting.*

the transparency, which behavior is in accordance with that described in literature [219]. Figure 3.3 shows the electrical conductivity of the p-type a-SiC:H films as a function of the methane and dopant gas flows. All shown films meet the criterion of a conductivity of at least 10^{-5} S cm^{-1}, as described in section 3.1.

From figure 3.3 it can be seen that increasing the diborane flow from 0.05 to 0.10 sccm at a fixed methane flow strongly increases the dark conductivity, more than a factor 4. Above 10 sccm the increase in conductivity with the dopant gas flow is small. By adding more methane to the source gas at a fixed diborane flow, both the conductivity and the absorption coefficient decrease significantly.

3.5.2 Doped hydrogenated microcrystalline silicon

The growth rate of the p-type μc-Si:H films was 6 ± 1 nm/min, while that of the n-type films amounted to 5.0 ± 0.2 nm/min.

Figure 3.4 shows $\alpha_{2.3}$ as a function of the thickness of the μc-Si:H film.

Because μc-Si:H has a much higher doping efficiency than a-Si:H has [110, 111, 162], the Fermi level of doped microcrystalline films can be closer to the valence or conduction band than in amorphous material. This is shown in figure 3.5 for relatively thick films, where it must be kept in mind that the activation energy of a-SiC:H films is generally about 0.4 eV.

A result of the closer position of the Fermi level to one of the band edges is that the dark conductivity of doped microcrystalline films can be several orders of magnitude higher than that of amorphous films, as is also shown in figure 3.5.

Figure 3.5 shows the dark conductivity of the μc-Si:H films as a function of the layer thickness. This figure also shows that the electrical properties of microcrystalline material strongly depend on the layer thickness. The change in material properties is especially pronounced for layers thinner than 40 nm. Layers with thicknesses around 10 nm have a very low conductivity in the order of 10^{-8} S cm^{-1}. Layers with thicknesses greater than 25 nm show high conductivity. For p-type material

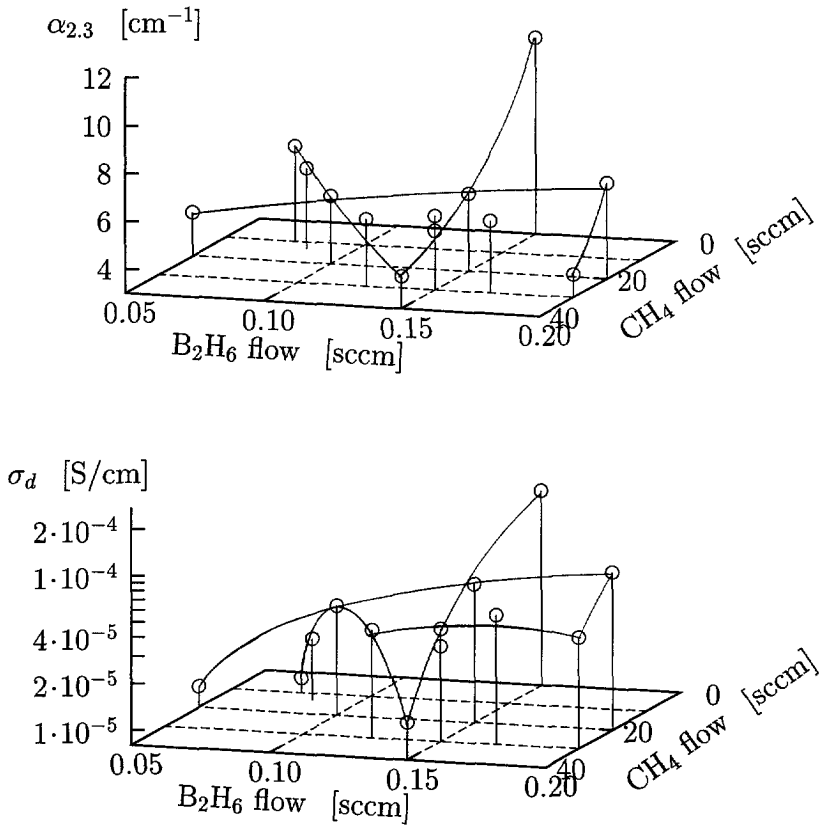

Figure 3.3: *Absorption coefficient at 2.3 eV ($\alpha_{2.3}$, figure above) and dark conductivity (σ_d, figure below) of p-type a-SiC:H films as functions of the diborane and methane gas flows.*

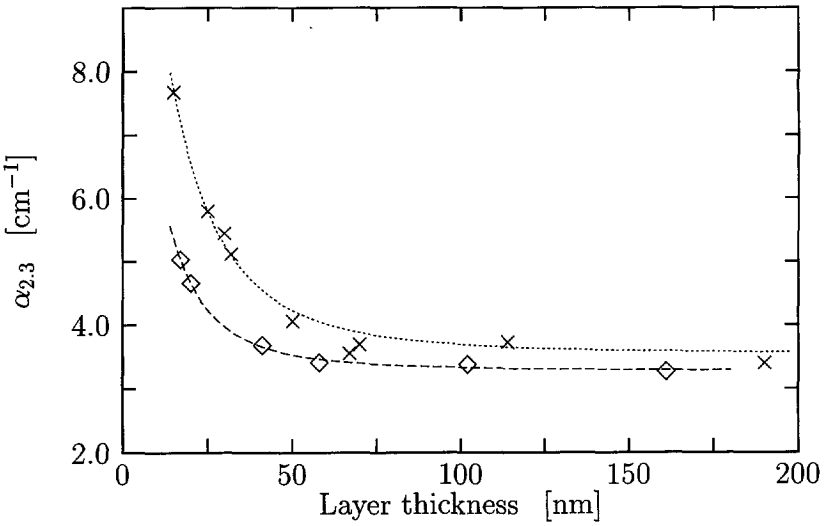

Figure 3.4: *Absorption coefficient at 2.30 eV ($\alpha_{2.30}$) of p-type (×) and n-type (◇) microcrystalline silicon films as functions of the film thickness. The dotted lines are for visual convenience.*

the conductivity is between 0.1 and 1.2 S cm^{-1} and for n-type material the conductivity is about an order of magnitude higher and amounts to about 8 S cm^{-1}. The dependence of the electrical properties on the layer thickness and the difference of an order of magnitude in conductivity between p- and n-type μc-Si:H material has also been found by other authors, independent of the exact deposition conditions, and thus independent of the exact value of the conductivity [131].

3.5.3 Doped hydrogenated microcrystalline silicon carbide

Figure 3.6 shows the Tauc optical gap, as a function of the methane to silane ratio of the source gas mixture. The optical gap of the layers increases with increasing methane content of the source gas.

Figure 3.6 shows the absorption coefficient $\alpha_{2.30}$ at an energy of 2.30 eV as a function of the methane to silane ratio. The absorption coefficient decreases with increasing methane content of the film. Thus,

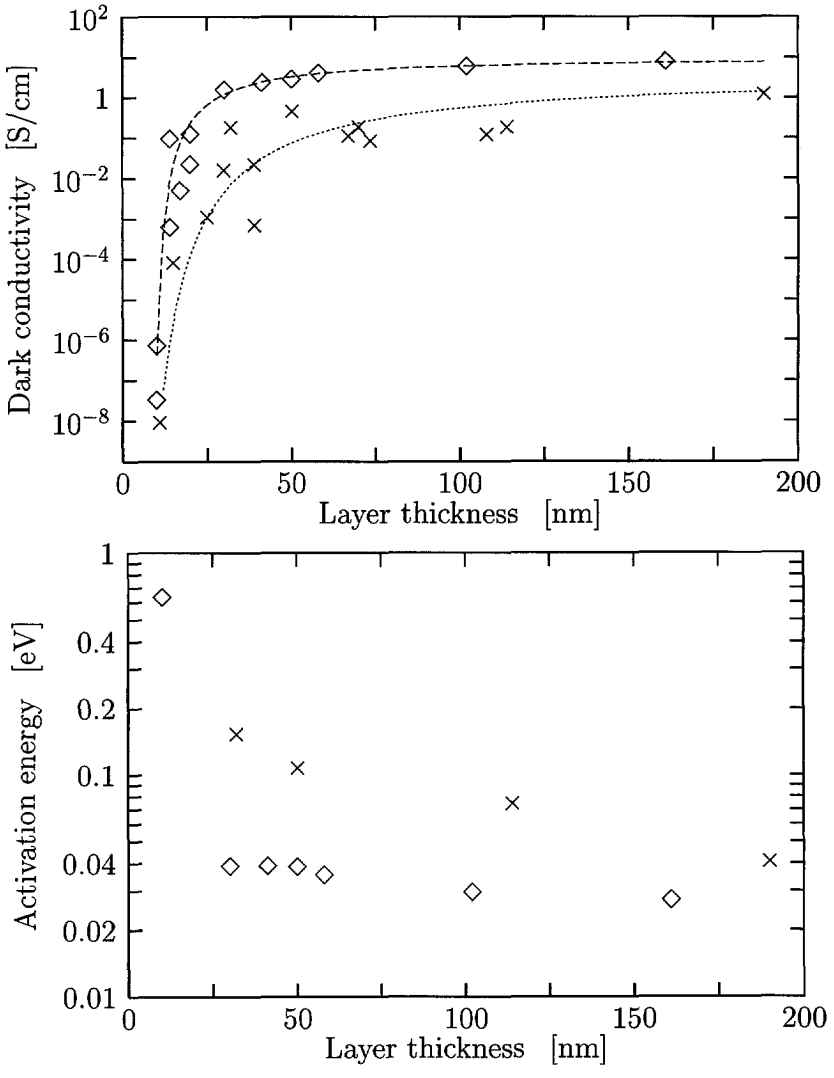

Figure 3.5: *Dark conductivity (above) and activation energy (below) of p-type (×) and n-type (◇) doped microcrystalline silicon films as functions of the layer thickness. The dotted lines are for visual convenience.*

by adding a small amount of carbon to the source gas mixture the microcrystalline films become more transparent.

In respect to the use of these layers in solar cells, it must be stated that actual doped layers applied in solar cells are thinner than the films used in this investigation, but the dependence of the optical properties on the thickness is not very pronounced [227].

The electrical properties were determined for the films deposited on Corning glass as well as for the films deposited on glass covered with intrinsic amorphous silicon. Figure 3.7 illustrates the influence of the source gas mixture on the electrical DC dark conductivity σ_d of these films. The films show a conductivity higher than 10^{-5} S cm^{-1} for a methane to silane ratio of less than about 8 % for p-type films. The value of 10^{-5} S cm^{-1} is a typical value of the conductivity of p-layers used in highly efficient solar cells. The n-type films deposited with source gas mixtures with methane to silane ratios of less than about 12 % have conductivities higher than 10^{-4} S cm^{-1}, which are useful values for solar cell application. The dark conductivity rapidly decreases for methane concentrations higher than the mentioned 8 % for p-type and 12 % for n-type films.

All silicon carbide films deposited on amorphous silicon show higher, or at least almost equal, conductivity than the same films deposited on bare Corning glass. The difference becomes more pronounced at higher methane to silane ratios of the source gas. This difference in conductivity is explained by the difference of the silicon carbide layers and is not an artifact of the conductivity of the underlaying amorphous intrinsic silicon film. Because the total conductivity σ_{tot} of a sandwich of two layers, with thickness a and b and conductivity σ_a and σ_b, stacked on top of each other, equals

$$\sigma_{tot} = \frac{a}{a+b} \cdot \sigma_a + \frac{b}{a+b} \cdot \sigma_b , \tag{3.1}$$

and the dark conductivity of the underlaying amorphous films is less than 10^{-10} S cm^{-1}, the underlaying film cannot account for a total conductivity of more than 10^{-10} S cm^{-1}.

The higher conductivity can be explained by two effects. The first effect is based on the fact that a film which is deposited under conditions

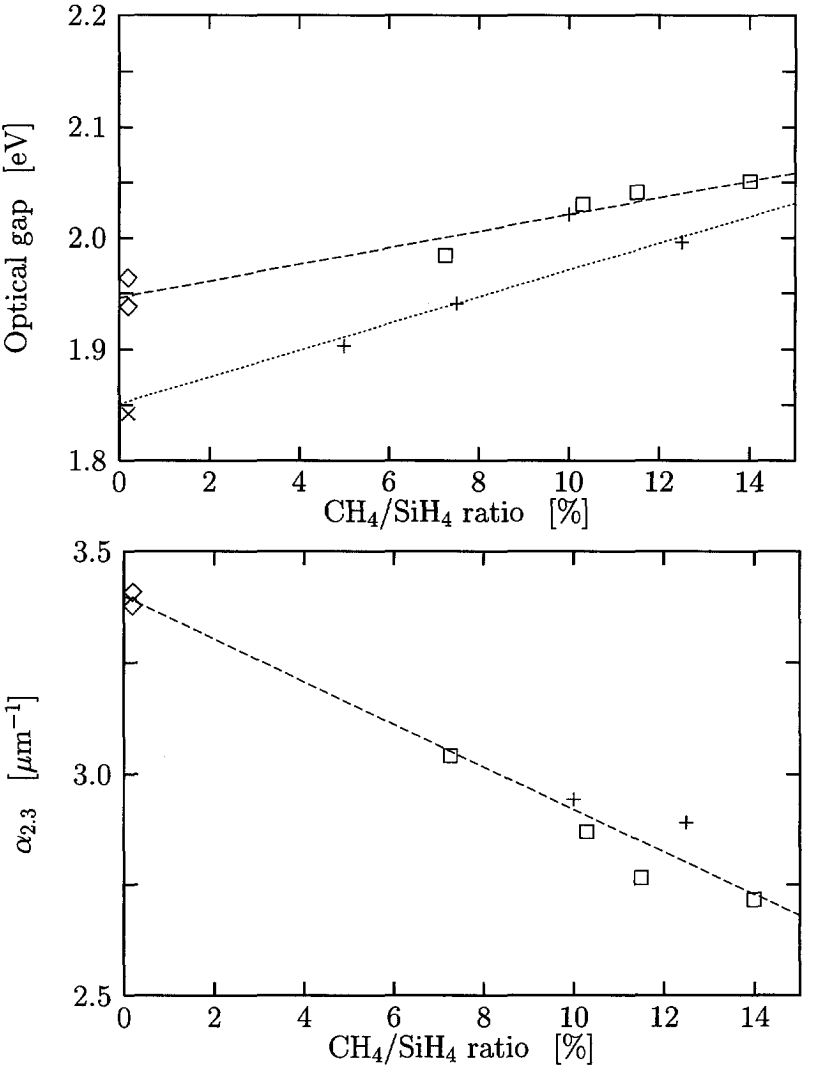

Figure 3.6: *Tauc optical gap (figure above) and absorption coefficient at 2.30 eV ($\alpha_{2.30}$) of p-type (+) and n-type (□) μc-SiC:H films as functions of the methane to silane ratio of the source gas. Values of comparable μc-Si:H films are marked with × for p-type, and ◇ for n-type films. The dotted lines are for visual convenience.*

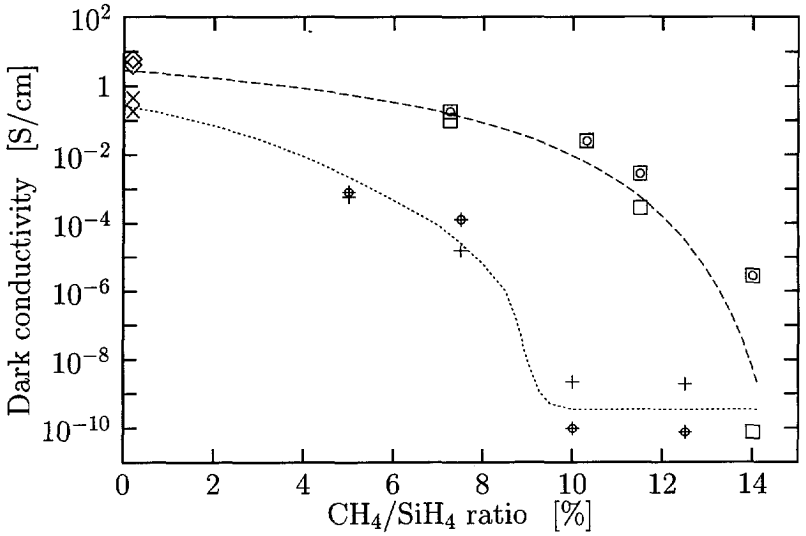

Figure 3.7: *Dark conductivity of doped μc-SiC:H films on Corning and amorphous substrates as a function of the methane to silane ratio of the source gas: +: p-type on Corning, ⌖ : p-type on amorphous substrate, □: n-type on Corning and ▨: n-type on amorphous substrate. Values of comparable μc-Si:H films are marked with × for p-type, and ◇ for n-type films. The dotted lines are for visual convenience.*

favoring microcrystalline growth can be roughly considered to consist of two parts [227]. The first part of the film is not microcrystalline and has a low σ_d. The rest of the film is microcrystalline and has a high σ_d. When the first part of the film becomes a relatively larger fraction of the total film thickness, the σ_d of the total film will decrease. But to explain a difference in σ_d of more than one order of magnitude, which is the case for the films deposited on a-Si:H versus those on Corning glass, it must be assumed that more than 0.9 of the total thickness of the films on Corning glass is not microcrystalline and only the last 10 % of the film is crystallized. This seems not to be very likely, and so a second effect has to take place also.

The second effect is that not only is the thickness of the first part of the film different, but the second part of the layer has a different

structure also, i.e. a different crystallite size or a different amount of amorphous tissue. The electrical measurements point in the direction that at least the second part of the film depends on the substrate.

Figure 3.8 shows the activation energy E_σ as a function of the methane to silane ratio of the source gas. Compared to typical activation energy values of 400 meV of doped a-SiC:H films [220], the activation energy of the n-type μc-SiC:H films remain low up to 14 % methane to silane ratio. For p-type films this ratio is at about 8 %. These low activation energies allow high open circuit voltages of solar cells, as explained in section 1.6.

The photoconductivity σ_{ph} under standard AM1.5, 100 mW/cm^2 illumination, was also measured. Figure 3.8 illustrates that the photosensitivity σ_{ph}/σ_d, rapidly increases at 8 % and 12 % methane to silane ratio for, respectively, p- and n-type films, which is the expected behavior in view of the rapidly decreasing dark conductivity and the increasing activation energy under these deposition conditions.

The electrical measurements show a transition from microcrystalline to amorphous material at the 8 % and 12 % methane to silane ratios for, respectively, the p- and n-type films.

As mentioned before, the actual doped layers in solar cells are thinner than the films in this investigation. In contrast to the optical properties, which do not show a strong dependence on the film thickness, the effect of the layer thickness on the dark conductivity is very pronounced. The difference in dark conductivity of 10 nm thick films versus 40 nm thick ones deposited under the same conditions can be eight orders of magnitude, as shown in figure 3.5. However, Shimada showed successful use of 10 nm thick layers which were prepared under microcrystalline formation conditions in solar cells [183].

3.5.4 Comparison of the different materials

Figure 3.9 shows the dark conductivity of a-SiC:H, μc-Si:H and μc-SiC:H films as functions of the absorption coefficient. The points in the lower right corner of the plot denote the best films in terms of transparency and conductivity. It can be seen that the μc-Si:H films are the best

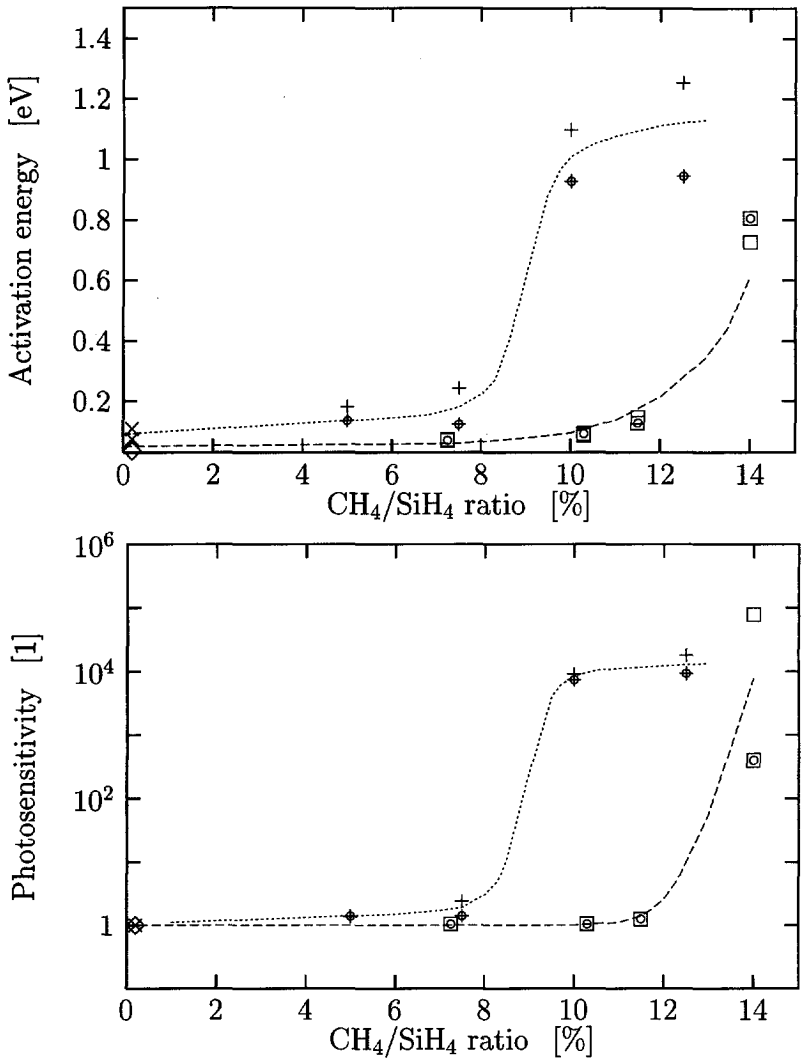

Figure 3.8: *Activation energy (above) and photosensitivity (σ_{ph}/σ_d, below) of μc-SiC:H films on Corning as well as on amorphous substrates, as functions of the methane to silane ratio of the source gas. Values are given for p-type on Corning (+), p-type on amorphous (⌖), n-type on Corning (□) and n-type on amorphous (▣) substrates. The values of μc-Si:H are marked with × for p-type, and ◇ for n-type films and the dotted lines are for visual convenience.*

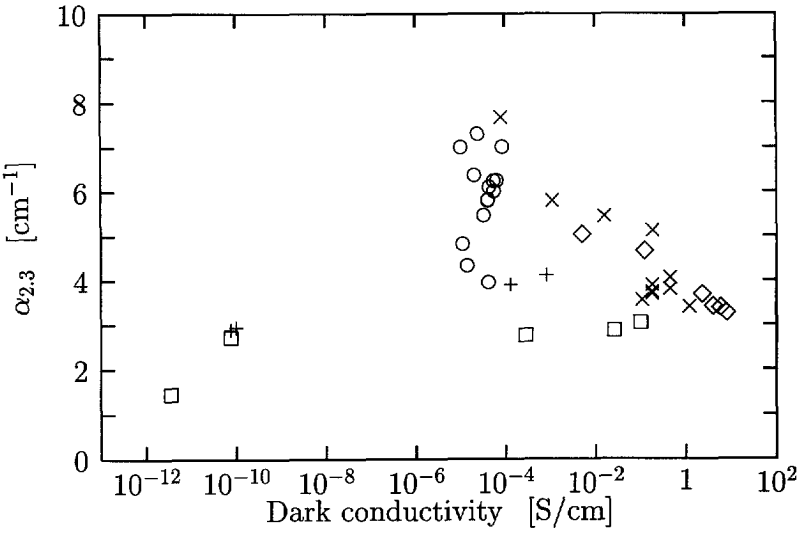

Figure 3.9: *Absorption coefficient at 2.3 eV as a function of the dark conductivity for a-SiC:H (p-type:* ○*), μc-Si:H (p-type:* ×*, n-type:* ◇*) and μc-SiC:H (p-type:* +*, n-type:* □*).*

choice in this respect. Also, the higher the conductivity of the μc-Si:H films is, the lower is the absorption, which is explained by the higher degree of microcrystallinity of the films with higher conductivity.

3.6 Electrical properties

Because of the importance of the electrical properties of a-Si:H and μc-Si:H, both from a theoretical as well as from a technological point of view, this subject is described in more detail in this section. Of the electrical properties of a material, the electrical DC conductivity is the most important in respect to its use in solar cells. Other electrical properties, such as the Hall effect and thermopower, do not play any role of importance in this field. Therefore, we focused on the DC conductivity.

In section 3.6.1, the DC conductivity is treated. The temperature dependence of the DC conductivity, which can be described by an activation energy in a limited temperature region, and the Meyer-Neldel

rule, a relation between two parameters describing the conductivity as a function of the temperature, are discussed in more detail in section 3.6.2.

3.6.1 Electrical DC conductivity

An explicit formula for the DC conductivity of amorphous semiconductors can be given if two important approximations are applied. The first approximation, the one particle approximation, takes the energy eigenstates independent of their occupation: the energy levels an electron can occupy are not influenced by other electrons. This approximation is least valid for the localized states. The second approximation is that a homogeneous material is assumed, which is not a priori the case in amorphous semiconductors. For inhomogeneous materials, conduction can be considered as a percolation process favoring the path of high conductance. With these two approximations the DC conductivity σ is given by [87, 53]

$$\sigma = \int e \cdot N(E) \cdot \mu(E) \cdot f(E,T) \cdot [1 - f(E,T)]\, dE, \tag{3.2}$$

where e is the electron charge,
$N(E)$ is the density of states distribution,
$\mu(E)$ is the carrier mobility and
$f(E,T)$ is the Fermi function of energy E and temperature T.

The dominant conduction path is thus determined by the DOS, the carrier mobility and the Fermi function. Three different regimes of the DC conductivity can be distinguished, depending on the energy of the carriers which carry the conduction [33, 47].

The first conduction mechanism is hopping, also called tunneling conduction [205, p. 17]. This is the hopping of carriers near the Fermi level E_F from occupied localized states to spatially and energetically nearby unoccupied states. Because it is unlikely to find such nearby states at the same energy level, the tunneling process is usually inelastic: it involves the emission or absorption of a phonon. Therefore a hopping energy ΔW_1 is involved and the conduction obeys

$$\sigma = \sigma_1 \cdot e^{-\Delta W_1 / kT}, \tag{3.3}$$

where σ_1 is a constant and ΔW_1 is the hopping energy.

Because unhydrogenated amorphous silicon has a very high defect density in the middle of the gap, conduction at room temperature takes place by hopping at the Fermi level. Due to the much lower defect density in hydrogenated a-Si:H, this hopping at the Fermi energy does not significantly contribute to the total conduction in hydrogenated a-Si:H at room temperature. But at low temperatures, the hopping at the Fermi level becomes the largest contribution to the DC conductivity of hydrogenated a-Si:H.

As the temperature is lowered, the number and energy of the phonons available for absorption decreases, and this restricts tunneling to centers which lie energetically closer to each other, typically within the range kT. This variable range hopping is hopping of carriers between centers which will generally not be nearest neighbors. Mott derived for this variable range hopping [124, 125]

$$\sigma = c \cdot e^{-(T_0/T)^{1/4}}, \tag{3.4}$$

where c and T_0 are constants.

The second conduction mechanism is thermally assisted hopping, which takes place near the mobility edges, E_V and E_C in figure 1.1. On raising the temperature, the Fermi distribution broadens, and because the DOS $N(E)$ and the mobility $\mu(E)$ increases as one moves from midgap to the band gaps, hopping near the band edges will become the prominent conduction mechanism at higher temperatures. The temperature at which this happens is well below room temperature.

The form of this conductivity is

$$\sigma = \sigma_2 \cdot e^{-(E-E_F+\Delta W_2)/kT}, \tag{3.5}$$

where σ_2 is a constant and ΔW_2 is the hopping energy.

It is expected that $\sigma_1 \ll \sigma_2$ since the density of states and the range of their wave functions is probably smaller near the Fermi level than near the mobility edges [47].

The third principal contribution to the DC conductivity is from band conduction, carried by electrons excited above the conduction band edge and by holes below the valence band edge.

Usually, for both doped and undoped material, this conduction takes place by a single type of carrier. In the following, the case of electrons will be considered; the corresponding formulas for holes are analogous. Because the conduction takes place far away from the Fermi level E_F by a single type of carrier, non-degenerate statistics can be applied: the Fermi function is approximated by the Maxwell Boltzmann function, and equation 3.2 reduces to

$$\sigma = \int e \cdot N(E) \cdot \mu(E) \cdot e^{-(E-E_F)/kT} \, dE. \tag{3.6}$$

The concept of a mobility edge states that $N(E)\mu(E)$ increases almost abruptly from zero to a finite value at the mobility edge E_C, and above this mobility edge $N(E)\mu(E)$ does not vary too rapidly with the energy [126]. In this case equation 3.6 can be approximated by

$$\sigma = \sigma_0 \cdot e^{-(E_C-E_F)/kT}, \tag{3.7}$$

where the prefactor σ_0 equals $e \cdot N(E_C) \cdot \mu(E_C) \cdot kT$, and is $\sim 200\ \mathrm{S\,cm^{-1}}$ for extended state transport in a-Si:H [147].

This equation is a reasonable approximation if $\sigma(E)$ increases rapidly enough in a limited energy range. Although there is doubt about the sharpness or even existence of a mobility edge, experiments confirm that equation 3.7 is an adequate description of the DC conductivity at room temperature and above [205]. For temperatures below room temperature, conductivity significantly below the mobility edge can be important, and this equation is not longer appropriate. Because our interest is in the temperature range of approximately 300 to 400 K, equation 3.7 was used to model the conductivity.

3.6.2 The activation energy and the Meyer-Neldel rule

To introduce the concept of the activation energy, the conductivity is usually written as

$$\sigma = \sigma_0 \cdot e^{-E_\sigma/kT}, \tag{3.8}$$

where E_σ denotes the activation energy and σ_0 is the conductivity prefactor. Figure 3.10 shows the experimental temperature dependence of

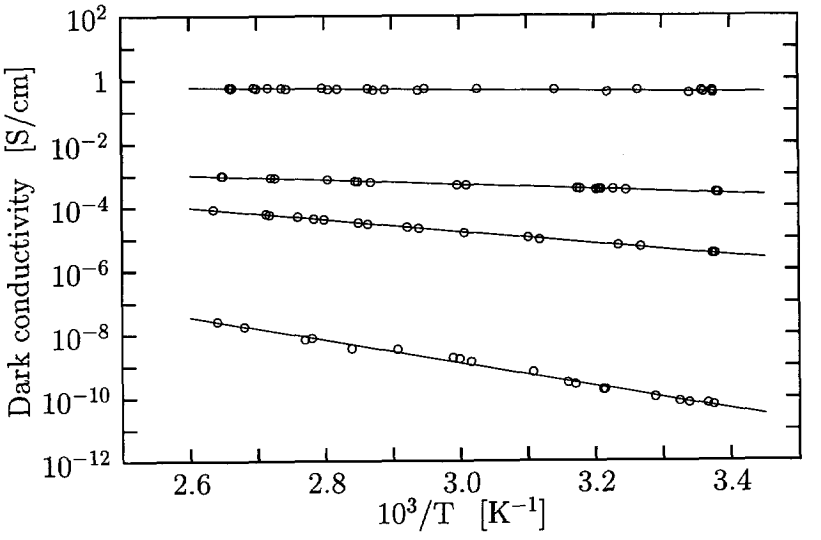

Figure 3.10: *Arrhenius plot: typical dark conductivity of doped microcrystalline and amorphous films as function of the reciprocal temperature.*

the dark conductivity of a few typical samples. From this figure it is clear that in this temperature range the measured data obey equation 3.8.

The Meyer-Neldel (MN) rule is frequently observed in the conductivity of inhomogeneous materials [39, 164], to which class amorphous materials belong. It describes the correlation between the prefactor σ_0 and the conductivity activation energy E_σ of equation 3.8 [114]:

$$\sigma_0 = \sigma_{00} \cdot e^{E_\sigma / kT_m}, \tag{3.9}$$

where σ_{00} and T_m are positive constants. The MN rule is satisfactorily explained by the statistical shift of the Fermi level with the temperature [76, 145, 146]. This statistical shift is the shift of the Fermi level with the temperature caused by the charge conservation law, together with the DOS $N(E)$ which is a non-constant function of the energy. The charge conservation law is

$$\int N(E) \cdot f(E,T)\, dE = constant\,, \tag{3.10}$$

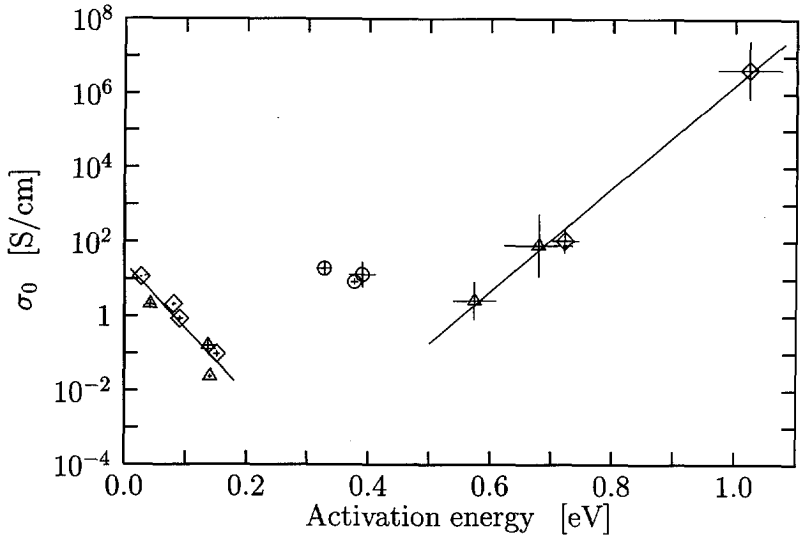

Figure 3.11: *The Meyer-Neldel rule of doped μc-SiC:H films, both p-type (△) and n-type (◇). For comparison, a few values of p-type a-SiC:H are also shown (denoted by ○). The error bars are denoted by horizontal and vertical lines.*

If it is assumed that $N(E)$ is independent of the temperature, differentiating equation 3.10 with respect to kT gives [257]

$$\frac{dE_F}{dkT} = -\frac{\int[\frac{E-E_F}{kT}]\cdot N(E)\cdot f(E,T)\cdot[1-f(E,T)]\,dE}{\int N(E)\cdot f(E,T)\cdot[1-f(E,T)]\,dE} \tag{3.11}$$

It is clear that the Fermi level shift with temperature is a weighted average of $-(E-E_F)/kT$. At higher temperatures the tail states become populated and the neutrality condition requires the Fermi level to move upwards in n-type a-Si:H.

As theoretically predicted by Overhof [147], there is a second region, with different values of σ_{00} and T_m, where σ_0 and E_σ also obey this relation, but with a negative T_m.

The MN rule states that for samples with different activation energies, the logarithm of σ_0 scales linearly with E_σ. From another point of view, it states that if the conductivity is plotted against the reciprocal absolute

Table 3.2: *The Meyer-Neldel parameters of different measurements.*

author	$\sigma_{00,low}$ [S cm^{-1}]	$T_{m,low}$ [10^2K]	$\sigma_{00,high}$ [S cm^{-1}]	$T_{m,high}$ [10^2 K]
Overhof [147]			0.0 ± 0.2	7.8 ± 0.5
Oversluizen [148]			-3 ± 1	5.5 ± 1.0
Street [205, p. 228]			-1.0	5.8
Lucovsky [100]	2.5 ± 0.8	-2.3 ± 1.5	0.2 ± 1.2	13.3 ± 7.0
this work	1.4 ± 0.8	-2.9 ± 1.3	-7.7 ± 2.7	3.6 ± 0.9

temperature for different samples, all lines intersect at the same point, given by

$$\sigma(T_m) = \sigma_{00}. \tag{3.12}$$

The MN rule is found independent of the way the activation energy is varied. In literature, the activation energy is varied by doping, by light-induced degradation, by the field effect in thin film transistors [37, 38, 70, 150, 245] and by the effect of the i-layer thickness on E_σ in n/i/n-structures [148, 149]. We report the MN rule by varying the activation energy caused by alloying with carbon. The results are shown in figure 3.11, and the values of σ_{00} and T_m, found from least squares fitting, are listed in table 3.2.

As can be seen from table 3.2, there is a wide variation in the constants σ_{00} and T_m. Other authors [205] also found this wide variation, depending on the film composition and the method of varying E_σ.

Both in the work of Lucovsky and in our work, σ_{00} and T_m of the low activation energy region, with $E_\sigma < 0.2$ eV, were determined from μc-SiC:H samples. For this low activation energy region, the values of σ_{00} and T_m found by Lucovsky and those found in our work agree within the limits of experimental error.

The values of σ_{00} and T_m of the high activation energy region, with $E_\sigma > 0.4$ eV, of Lucovsky's work were determined from conventional, a-Si:H samples. Therefore, no direct comparison between the σ_{00} and T_m of our and Lucovsky's work is permissible.

3.7 Conclusions

In section 3.1, the general requirements on the optical and electrical characteristics of the doped layers of solar cells were discussed: the doped layers should be as transparent as possible, while maintaining a sufficiently high dark conductivity and sufficiently low activation energy. Because the front p-type layer is the most crucial of the doped layers, we focused on this layer.

Two common methods to obtain highly transparent, highly conducting doped material are alloying a-Si:H with carbon, and producing microcrystalline material. We investigated the optical and electrical properties of films obtained by these methods and of a novel material, microcrystalline silicon alloyed with carbon. The last material, μc-SiC:H, was successfully produced earlier on a small scale with the ECRCVD technique [62, 64, 65]. However, the technique is difficult to scale up to industrial scale, and with deposition technologies compatible with industrial scale, μc-SiC:H material is much harder to obtain.

We showed that by adding carbon to microcrystalline films the optical properties are enhanced, but at the same time the electrical properties become less favorable in respect to the use of these layers in solar cells. By adding small amounts of carbon to μc-Si:H films these films remain microcrystalline, and from measurements of the optical and electrical properties of the investigated p-type μc-SiC:H films, it is expected that films deposited with a methane to silane ratio of up to 8 % yield solar cells which are superior to those with an a-SiC:H or unalloyed μc-Si:H p-type layer.

Regarding the microcrystalline films, it is found that the optical and electrical properties outperform a-SiC:H films, as shown in figure 3.9.

The concept of the activation energy and the Meyer-Neldel rule have been treated in section 3.6.2. We show that the Meyer-Neldel rule also applies to μc-SiC:H, and, for the low energy region, values of the conductivity prefactor and the characteristic temperature of 1.4 ± 0.8 S cm^{-1} and -290 ± 130 K were found. These values agree within the limits of experimental error with values found by Lucovsky [100].

Chapter 4

Modeling of a-Si:H based p/i-heterojunctions

4.1 Introduction

A heterojunction is a junction between two different semiconductors which can have different physical properties such as a different band gap or different electron affinity. By not only using homojunctions in a device, but also using heterojunctions, more freedom in the device design is obtained and devices with a higher performance can be fabricated. For example, silicon germanium transistors achieve a much higher gain bandwidth product than silicon transistors do. Therefore, heterojunctions play an important role in new electronic devices, for example superlattice structures, resonant tunneling transistors, thin film transistors, solar cells, high electron mobility transistors (HEMTs) and modulation doped field-effect transistors (MODFETs) [36, 41, 214]. The band lineup at a heterojunction is an important subject both from theoretical and experimental point of view.

In amorphous silicon solar cells the p/i-interface represents a heterojunction because the p-layer is alloyed with carbon in order to widen the band gap and so to increase the efficiency [219]. This junction significantly influences solar cell characteristics and several studies have been carried out on this subject [85, 190, 259]. Usually it is assumed that the band discontinuity is totally accommodated by the conduction band.

Different experimental methods have been applied to measure the band offset [44]. In 1978, for the first time photoemission techniques

were carried out on crystalline Ge/GaAs interfaces [12, 50, 154]. In a photoemission experiment, the surface of a semiconductor is bombarded with ultraviolet (UV) or soft X-ray photons. This photon flux causes electrons to be emitted from the material, and the energy distribution of these electrons is measured. In a first approximation, this distribution reflects the distribution in energy of the electrons in the specimen, shifted upwards in energy by an amount equal to the photon energy. Because the electrons excited upon absorption of a photon have a mean free path in the sample in the order of a few nanometers, the energy distribution of the emitted electrons reflect the energy distribution in the sample close to the surface. When the specimen consists of a semiconductor substrate with a thin overlayer of a different semiconductor, the photoemission spectrum contains contributions from the substrate and the overlayer, from which the valence band discontinuity can be found. Photoemission studies are widely used in investigations in interfaces formed between crystalline materials [107]. This method is not only restricted to the application on crystalline materials, but can also be applied to interfaces formed between amorphous semiconductors [43, 44].

For heterojunctions consisting of boron doped a-SiC:H on a-Si:H, a negligible valence band discontinuity was found by UV-photoemission spectroscopy [43, 44]. The precision of this method is not better than 0.1 to 0.15 eV and the technique does not give information on the mobility edge, which is the important quantity in dealing with electronic transport in amorphous semiconductors. Investigation by X-ray photoelectron spectroscopy shows valence band offsets increasing with the carbon content of the p-layer [44] with a precision of 0.1 eV.

In order to get a better understanding of abrupt p/i-heterojunctions, and in an attempt to determine the band lineup more accurately, simulations and measurements of the JV-characteristics of metal/p/i/metal structures have been carried out. To obtain the baseline set of parameters for the simulation of the p/i/metal structure, dark and illuminated JV-characteristics of a single-junction solar cell were simulated.

This work

First, some theoretical backgrounds will be given. Second, by inverse modeling a set of parameters was established to simulate the dark and illuminated JV-characteristics of an experimental single-junction solar cell. Third, a sensitivity study was performed to obtain information on the influence of several parameters on the JV-characteristics of p/i-heterojunctions. From this, it is concluded that it is feasible to extract the band lineup from measured JV-characteristics. Next, the extraction was actually carried out on an experimental p/i-sample. Last, the capacitance as a function of the frequency of the single-junction solar cell is determined. This measurement can serve as a cross check for the values of the electrical properties used in the electrical simulations.

4.2 Theory: the Anderson model

First, the best-known model for the description of a crystalline semiconductor heterojunction, the Anderson model [4], will be described. This model is the basis for the description and simulation of amorphous silicon heterojunctions.

Figure 4.1 shows the band diagram of a heterojunction consisting of two materials isolated from each other. When brought into contact with each other, band bending will occur, as depicted in figure 4.2. The two semiconductors may have different band gaps E_g, different work functions ϕ and different electron affinities χ. The work function is defined as the energy required to move an electron from the Fermi-level E_F to a position just outside the material. The electron affinity is defined as the energy required to move an electron from the conduction band E_C to a position just outside the material and equals 4.05 eV for crystalline silicon [213, 253]. Hydrogenated amorphous silicon has an electron affinity which is close to this value, as found by measuring the shift of flat-band voltages of metal/silicon dioxide/silicon devices with a-Si:H electrodes ($\chi = 4.06$ eV [93]) and from measurements of the conduction band discontinuity between a-Si:H and c-Si by means of internal photoemission [116] and junction capacitance measurements [42]. The last two mea-

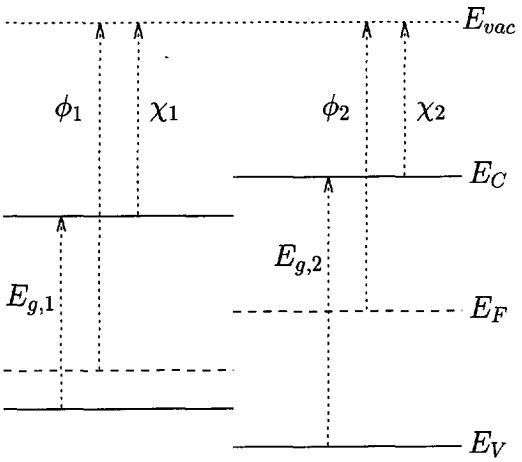

Figure 4.1: *Schematic energy diagram of an isolated p/i-heterojunction.*

surement techniques yield a difference in electron affinities between c-Si and a-Si:H of 50 ± 50 meV, resulting for the electron affinity of a-Si:H a value of 4.0 ± 0.05 eV.

The relation between the conduction band discontinuity $\triangle E_C$ and the electron affinities of the materials forming the junction equals

$$\triangle E_C = q(\chi_2 - \chi_1)\,. \tag{4.1}$$

From this, the valence band discontinuity $\triangle E_V$ must obey

$$\triangle E_V = q(\chi_2 - \chi_1) - (E_{g,2} - E_{g,1})\,. \tag{4.2}$$

4.3 Used samples

The solar cell used to establish the baseline set of parameters for simulating a-Si:H devices was a single-junction pin-cell, with a p- and n-layer thickness of 20 nm, and an intrinsic layer thickness of 500 nm. There was no buffer layer between the p- and i-layer. On this cell, also capacitance measurements were carried out, in an attempt to cross check the input parameters of the simulations of the JV-characteristics.

The sample was deposited in the multi-chamber ultra-high vacuum 13.56 MHz PECVD system called PASTA [104], by the University of Utrecht.

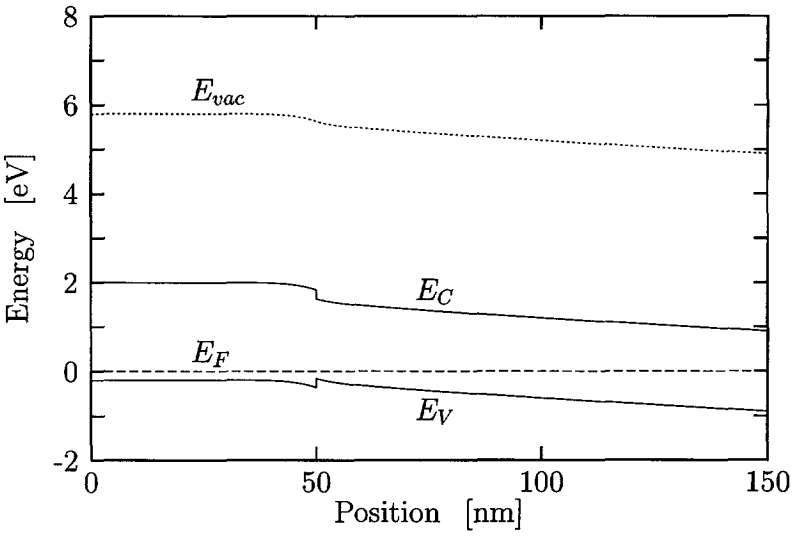

Figure 4.2: *Schematic energy diagram of a p/i-heterojunction in equilibrium. In this example, the band discontinuity is divided equally over the valence and conduction band. In order to show the band bending more clearly, the difference of mobility gaps is taken larger as usual (p-layer: 2.20 eV, i-layer: 1.80 eV) and the Fermi-level in the p-layer is taken quiet near the valence band (distance 0.2 eV).*

The deposition system is described detailed by Madan et al. [104]. The area of the silver back contacts is 16 mm^2. The layer thicknesses of the intrinsic and doped layers were determined from the growth rates, which values are well established. To check the layer thicknesses, the total thickness of the solar cell was measured with a step-profiler, a device to measure thickness differences of less than a nanometer. The total thickness of the amorphous layers of the cell was measured to be 537±1 nm, which means an accuracy of the layer thicknesses of better than 1 %.

The structure of the experimental p/i-sample was glass/Cr/p-SiC:H/ i-Si:H/Al. The p- and i-layer thicknesses are respectively 200 nm and 300 nm. The metal layers were produced by thermal evaporation. As a substrate, Corning glass covered with a semitransparent, 30 nm thick chromium layer was used. The amorphous layers were deposited by

RFCVD with the 13.56 MHz deposition system described in section 1.5. The p-layer was deposited with a silane/methane/hydrogen/diborane mixture in a gas flow ratio of 200/133/100/1 and the i-layer with a silane/hydrogen mixture with a gas flow ratio of 5/3. The area of the aluminum back contacts is 7.5 mm^2.

4.4 Modeling of a-Si:H devices

The forward model used to simulate the behavior of the amorphous silicon devices is the Amorphous Semiconductor Analysis (ASA) program, developed at the Delft University of Technology. The ASA computer code is a one-dimensional steady state simulator, designed to simulate single junction solar cells, tandem solar cells as well as Schottky structures.

For the calculation of the recombination rate, a discretized model of a continuous density of energy states in the gap was used. The gap states are described by conduction band and valence band tail states and the defect states. The conduction band and valence band tail states are assumed to have an exponential distribution, and the defect states in the gap are represented by two Gaussian distributions. The concentration of the defect states is calculated from the Urbach energy, as proposed by Stutzmann [209], and described in section 2.7.2.

ASA is described in more detail in appendix B.

4.4.1 Establishing the baseline set of simulation parameters

To determine the baseline set of parameters for the modeling of a-Si:H solar cells, dark and illuminated JV-characteristics of a single-junction solar cell were fitted to experimental characteristics. This was done with the technique of inverse modeling, in which the input parameters of a forward model are adapted by fitting the simulated results to experimental data by an optimization driver, until the simulated data sufficiently matches the experimental data. More on the technique of inverse modeling can be found in appendix A.

The JV-characteristics of the solar cell in dark and illuminated with

Table 4.1: *List of standard parameters used for the simulation of the single-junction solar cell. The measured values are denoted by m, the independent fitting parameters are denoted by ∗, and the parameters calculated from other fitting parameters are denoted by c. Parameters not mentioned are taken from literature.*

Parameter	status	p-layer	i-layer	n-layer
Thickness [nm]	m	20.0	500.0	20.0
Relative dielectric constant		7.2	11.9	11.9
Mobility gap $E_{g,mob}$ [eV]	$*$	1.83	1.70	1.70
Electron mobility μ_n [$cm^2 V^{-1} s^{-1}$]		1.0	10.0	2.0
Hole mobility μ_p [$cm^2 V^{-1} s^{-1}$]		0.2	2.0	0.4
Effective density of states $N_C = N_V$ [cm^{-3}]	c	$3.2 \cdot 10^{20}$	$3.2 \cdot 10^{20}$	$3.2 \cdot 10^{20}$
Activation energy E_σ [eV]	m	0.46	0.85	0.29
DOS at mobility edge N_{me} [$cm^{-3}eV^{-1}$]	$*$	$6.4 \cdot 10^{21}$	$6.4 \cdot 10^{21}$	$6.4 \cdot 10^{21}$
Valence band tail charact. energy [eV]		0.100	0.047	0.047
Conduct. band tail charact. energy [eV]		0.065	0.028	0.028
Cross section of neutral tail states [cm^2]	$*$	$1.2 \cdot 10^{-16}$	$1.2 \cdot 10^{-16}$	$1.2 \cdot 10^{-16}$
Cross section of charged tail states [cm^2]	c	$1.2 \cdot 10^{-14}$	$1.2 \cdot 10^{-14}$	$1.2 \cdot 10^{-14}$
Concentration of defect states N_{db} [cm^{-3}]		$4.0 \cdot 10^{18}$	$3.0 \cdot 10^{15}$	$7.6 \cdot 10^{16}$
Position of $E_C - E^0_{db}$ [eV]		−1.07	−1.00	−1.00
Position of $E_C - E^-_{db}$ [eV]		−0.76	−0.70	−0.70
Standard deviation Gaussian distribution		0.20	0.20	0.20
Cross section of neutral defect states [cm^2]	c	$1.2 \cdot 10^{-15}$	$1.2 \cdot 10^{-15}$	$1.2 \cdot 10^{-15}$
Cross section of charged defect states [cm^2]	c	$1.2 \cdot 10^{-13}$	$1.2 \cdot 10^{-13}$	$1.2 \cdot 10^{-13}$

400 nm and 600 nm monochromatic light were fitted with one set of simulation parameters. The results of the inverse modeling are shown in figure 4.3 [191, 261], and the set of parameters is listed in table 4.1. The status of the fitted parameters is listed in table 4.2.

4.5 Modeling of p/i-heterojunctions

4.5.1 Forward modeling

The sensitivity of several material properties on the behavior of the p/i-structure was studied in order to gain knowledge about the parameters with the most pronounced effect on the JV-characteristics of a p/i-

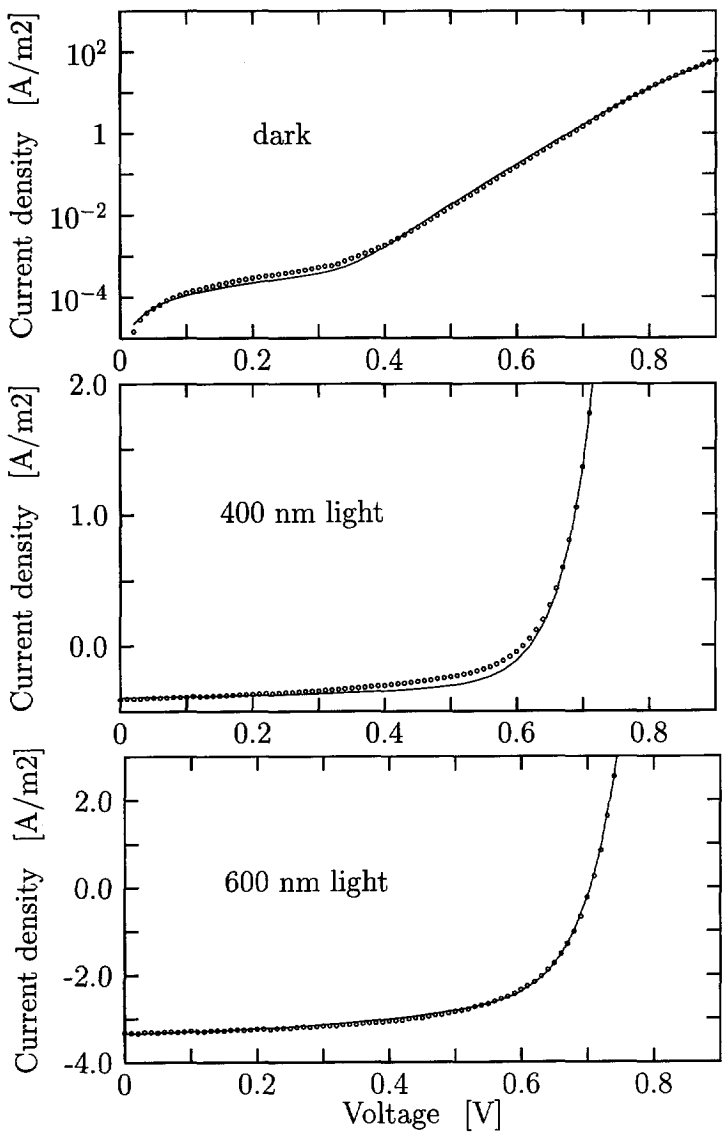

Figure 4.3: *Simulated* JV*-characteristics of a single-junction solar cell in dark (above), and illuminated with 400 nm (middle) and 600 nm (bottom) monochromatic light.*

Table 4.2: *List of the status of the fitted parameters used for the simulation of the single-junction solar cell, as listed in table 4.1. All parameters, except for the mobility gap, are taken equal throughout the pin-device.*

Independent fitting parameters	
Mobility gap of the i-layer [eV]	$E_{g,mob,i}$
DOS at the mobility edge [$cm^{-3}eV^{-1}$]	N_{me}
Cross section of the neutral tail states [cm^2]	c_n
Dependent fitting parameters	**dependence**
Mobility gap of the p-layer $E_{g,mob,p}$ [eV]	$E_{g,mob,i} + 0.13$
Mobility gap of the n-layer $E_{g,mob,n}$ [eV]	$E_{g,mob,i}$
Effective density of states $N_C = N_V$ [cm^{-3}]	$2 \cdot kT \cdot N_{me}$
Cross section of the charged tail states [cm^2]	$10^2 \cdot c_n$
Cross section of the neutral defect states [cm^2]	$10 \cdot c_n$
Cross section of the charged defect states [cm^2]	$10^3 \cdot c_n$

heterojunction. The influence of the interface states, the band offset and the mobility are presented here. The influence of interface states at the p/i-junction was simulated by a narrow (5 nm) defective intrinsic layer with a defect density equal that of the p-layer.

The voltage range of the simulations was chosen to be 0.0 to 1.0 V, because this is the range where the effect of different band lineups is most pronounced, as shown in figure 4.4.

The parameters used for the modeling of the p/i-structure are listed in table 4.3. Results for three types of band lineups are presented, viz. where the band discontinuity only appears in the conduction band or in the valence band, and where the discontinuity is equally divided between the bands.

Results of the forward modeling

The mobility of the charge carriers, the density of gap states and the introduction of a defect layer shows the most pronounced effect on the current characteristics. The effect of these parameters is shown in figure 4.5. This figure also shows that the band lineup clearly influences the current density. The band lineup where the discontinuity appears only in the conduction band gives rise to the highest current density,

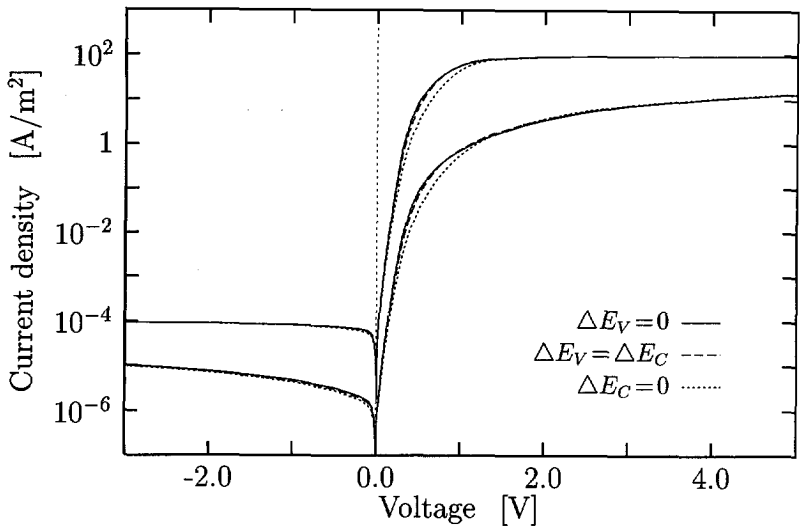

Figure 4.4: *Simulated* JV*-characteristics of a p/i-junction. Parameters are as listed in table 4.3. In each figure three graphs are given for* μ_p = *0.1* cm^2/Vs *(lowest current) and for* μ_p = *10* cm^2/Vs *(highest current).*

because the current in the p/i-structure is carried by holes.

The sensitivity study was important to determine the most influential parameters, which were chosen to be the fitting parameters for inverse modeling.

4.5.2 INVERSE MODELING

Inverse modeling was used to determine the band lineup of an amorphous p/i-structure, from the measured JV-characteristics [228]. The fit to the JV-curve is shown in figure 4.6 and the simulation parameters are listed in table 4.3. The band discontinuity was found to be located both at the conduction band and valence band, where $\Delta E_V = 0.11 \pm 0.05$ eV and the i-layer valence band is positioned lower than the p-layer valence band. The error is based on a 95.4 % confidence region and is deduced from the fitting procedure. The mobility gaps of the p- and i–layer were respectively 1.90 and 1.75 eV.

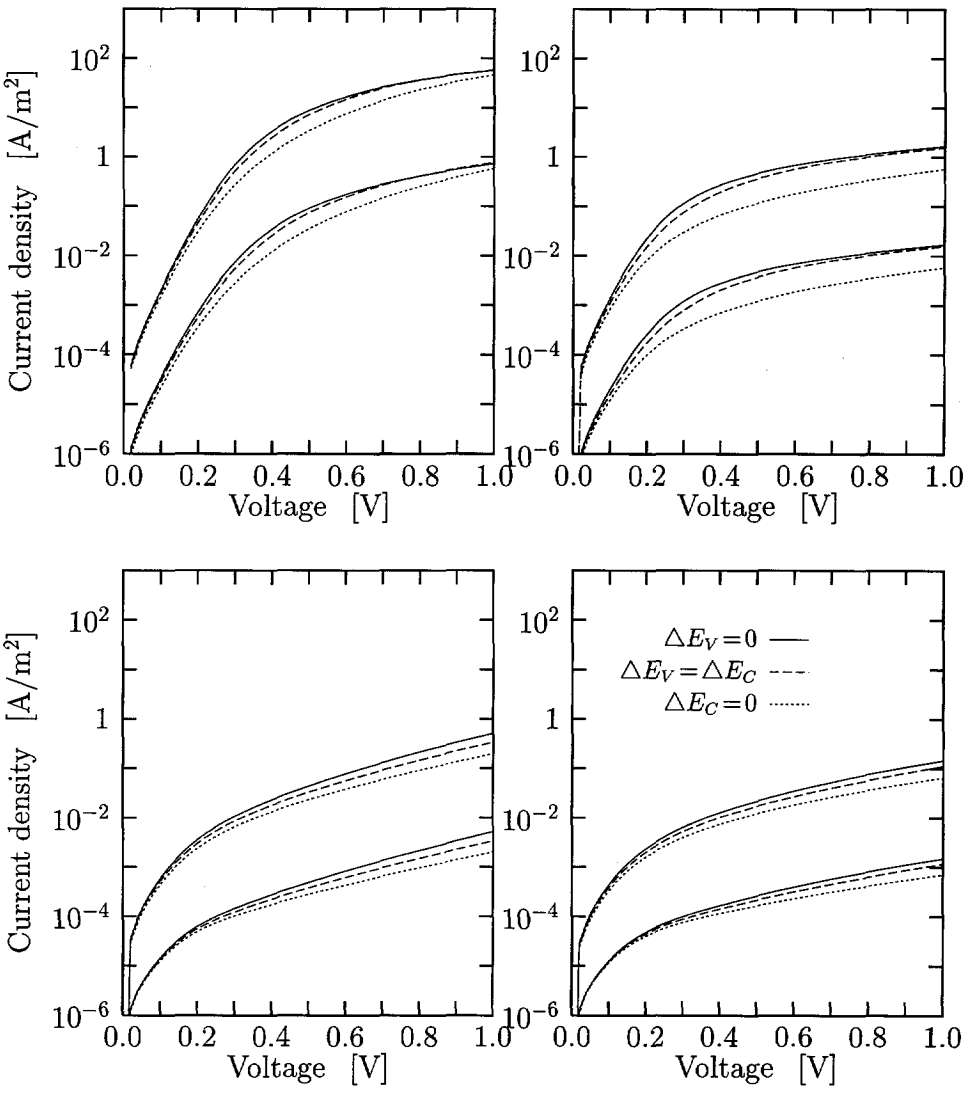

Figure 4.5: *Simulated* JV*-characteristics of a p/i-junction without (left figures) and with (figures on the right) defect layer. Parameters are as listed in table 4.3, with* $N_{db,i}$*=5·10*^{15} *for upper figures and 5·10*^{16} *for lower figures. In each figure three graphs are given for* μ_p*=0.1 cm*^{2}*/Vs (lowest current) and* μ_p*=10 cm*^{2}*/Vs (highest current).*

Table 4.3: *List of parameters used for the simulation of p/i-heterojunctions. The measured values are denoted by m and the independent fitting parameters are denoted by ∗.*

Parameter	status	p-layer	defect layer	i-layer
Thickness [nm]	m	50.0	5.0	300.0
Relative dielectric constant		7.2	11.9	11.9
Mobility gap $E_{g,mob}$ [eV]	$*$	1.90	1.75	1.75
Electron affinity χ [eV]	$*$	0.0	0.258	0.258
Electron mobility μ_n [$cm^2\,V^{-1}\,s^{-1}$]		10.0	10.0	10.0
Hole mobility μ_p [$cm^2\,V^{-1}\,s^{-1}$]	$*$	1.0	0.48	0.48
Effective density of states $N_C = N_V$ [cm^{-3}]		$2.0 \cdot 10^{20}$	$2.0 \cdot 10^{20}$	$2.0 \cdot 10^{20}$
Activation energy E_σ [eV]	m	0.47	0.88	0.88
DOS at mobility edge N_{me} [$cm^{-3}eV^{-1}$]		$1.0 \cdot 10^{21}$	$1.0 \cdot 10^{21}$	$1.0 \cdot 10^{21}$
Valence band tail charact. energy [eV]		0.100	0.100	0.045
Conduct. band tail charact. energy [eV]		0.040	0.030	0.030
Cross section of neutral tail states [cm^2]		$1.0 \cdot 10^{-16}$	$1.0 \cdot 10^{-16}$	$1.0 \cdot 10^{-16}$
Cross section of charged tail states [cm^2]		$1.0 \cdot 10^{-14}$	$1.0 \cdot 10^{-14}$	$1.0 \cdot 10^{-14}$
Concentration of defect states N_{db} [cm^{-3}]		$2.0 \cdot 10^{18}$	$2.0 \cdot 10^{18}$	$5.0 \cdot 10^{15}$
Position of $E_C - E_{db}^0$ [eV]	$*$	-1.15	-1.05	-1.05
Position of $E_C - E_{db}^-$ [eV]	$*$	-0.75	-0.65	-0.65
Standard deviation Gaussian distribution		0.15	0.15	0.15
Cross section of neutral defect states [cm^2]		$1.0 \cdot 10^{-14}$	$1.0 \cdot 10^{-16}$	$1.0 \cdot 10^{-16}$
Cross section of charged defect states [cm^2]		$1.0 \cdot 10^{-12}$	$1.0 \cdot 10^{-14}$	$1.0 \cdot 10^{-14}$

4.6 Capacitance measurements on amorphous devices

For the determination of doping-profiles of crystalline pn-junctions, a widely used method is measuring the capacitance as a function of the applied voltage (CV-measurements) [175, 68]. The small signal capacitance of the depletion region at the junction is measured, from which the depletion region width is determined. The capacitance is caused by the depletion region, which is the region depleted of free carriers, and therefore showing dielectric behavior. The impurity concentration as a function of the position is determined from the dependence of the depletion region width on the applied reverse bias.

However, impurity profiles can only be measured reliable if the measured capacitance is independent of the test frequency [82], which is not

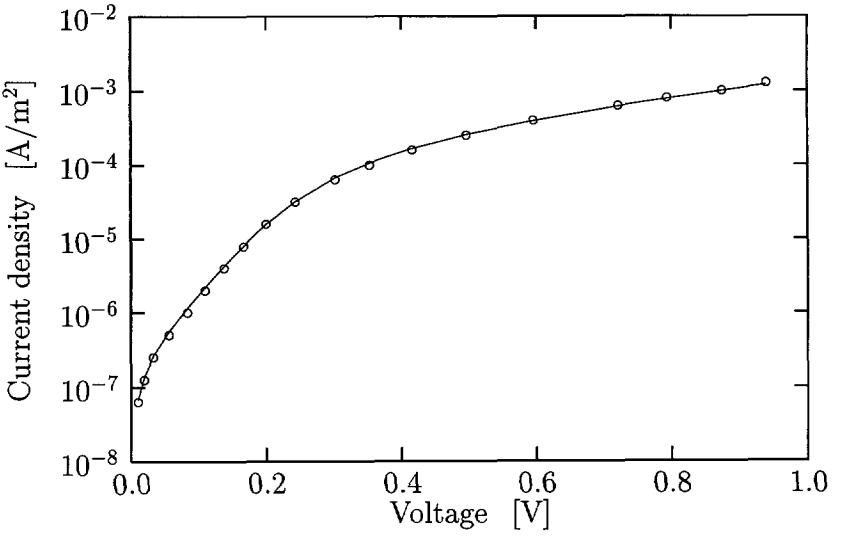

Figure 4.6: *Measured (o) and fitted (line)* JV*-characteristics of the p/i-heterojunction.*

the case when amorphous devices are measured, as shown in figure 4.7 and by other authors [66]. The continuous density of states in the band gap of an amorphous semiconductor causes the capacitance to be dependent on the test-signal frequency. The lower the frequency, the more band gap energy levels act as effective trapping centers trapping and releasing carriers within the time-scale of one cycle of the test signal, and thus the higher the capacitance.

Therefore, CV-measurements can be employed on amorphous devices for the extraction of the density of states in the band gap of the a-Si:H material. Extensive theory and calculations of the admittance and CV-characteristics of Schottky structures as a function of the frequency are published by different authors [2, 6, 7, 8, 77, 78, 187, 212]. However, for pin-devices these calculations are not valid, and an analogous treatment is far more complex because the charge in the intrinsic layer is not negligible, causing large depletion width variations as function of the reverse bias. Also, instead of one depletion region, as is the case in a Schottky structure, in a pin-device two depletion regions exist, compli-

cating a mathematical treatment of the device response to an AC stimulus. Only thick pνn-structures, where the ν-layer is a lightly doped amorphous layer, can be treated analogous to an a-Si:H Schottky barrier. The ν-layer should be in the order of 1 μm so that the pνn-structure behaves like a Schottky barrier with respect to the capacitance [82].

The frequency dependence of the capacitance of a pin-structure was measured at zero bias voltage. The high-frequency part of this measurement was used to check the values of the relative dielectric constants of the doped and undoped amorphous layers, and the low-frequency part is presented here as a reference for simulating Cf-characteristics of a pin-structure.

4.6.1 Measurement setup

The capacitance as a function of the frequency at zero bias voltage was measured with two setups. For the frequencies above 100 Hz, a Hewlett-Packard 4247A multi-frequency LCR-meter was used, which determines the real and imaginary part of the response of a device to a sine wave with small amplitude of typically 20 mV. The experimental error of the capacitance determined with this setup is estimated to be less than 4 %.

For frequencies below 200 Hz, a setup consisting of a separate function-generator and oscilloscope was used. A low-frequency sine wave, produced by the function-generator, was applied to the device, and the current effected by the applied voltage was measured with the oscilloscope. The oscilloscope used was a Tektronix DSA601A digitizing signal analyzer, a CPU-based storage scope which provides a time-base up to 100 sec/division, thus capable to monitor very low frequency signals. Both the voltage and current were measured with the signal analyzer, and from the basic equations of the transfer-function of a capacitor parallel to a resistance, the capacitance was calculated from the measured data. With this setup is was possible to determine the capacitance of the used pin-device down to 0.1 Hz. For this frequency, the experimental error is estimated to be $\sim$ 10 %.

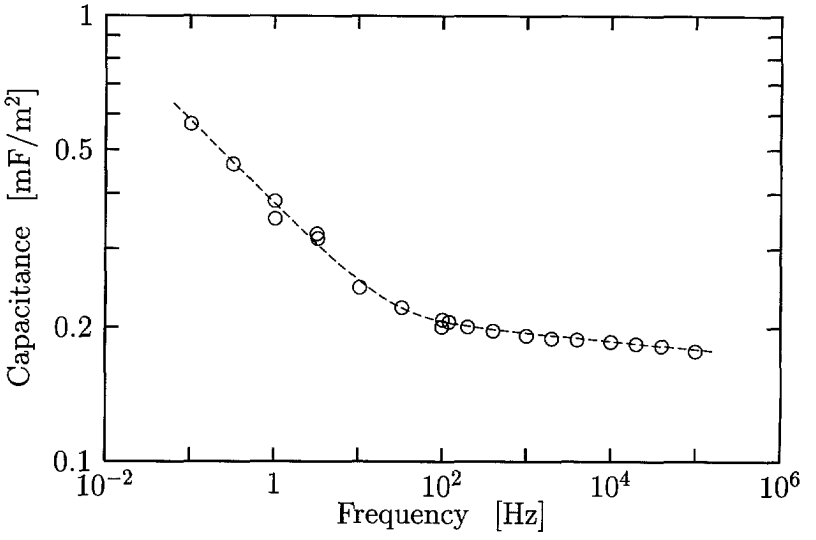

Figure 4.7: *Capacitance of the pin-device. The experimental error of the capacitance is about the height of the circles.*

4.6.2 Results and discussion

Figure 4.7 shows the capacitance of the pin-device. For high frequencies, the capacitance approaches the theoretical value of the geometrical capacitance formed by the p-, i- and n-layer, which amounts to 0.186 mF/m^2, if relative dielectric constants as stated in table 4.1 are assumed. So, this measurement confirms the correctness of these values.

For low frequencies, below 100 Hz, the effect of the defect states dominates the Cf-characteristics. For these frequencies, carriers move in and out the depletion region in the i-layer, thereby filling and emptying gap states at energies near the Fermi level. The capture and emission of carriers depend exponentially on the energy difference between the Fermi level and the conduction band.

With the steady-state simulator ASA, the Cf-characteristics can not be simulated, and, furthermore, ASA cannot easily be extended to handle transient signals necessary to simulate capacitance measurements. This is, because the semiconductor equations become time-dependent in

this case, requiring a different numerical approach to solve the set of equations. Work in this direction, for the simulation of time-of-flight measurements, is, for example, published by Shapiro [182].

The low-frequency part of the Cf-characteristics is presented as a reference for future modeling of the capacitance as a function of the frequency of pin-devices.

4.7 Conclusions

With the device simulator ASA, the JV-characteristics of a single-junction solar cell in dark and illuminated with 400 nm and 600 nm monochromatic light were simulated in order to obtain a set of input parameters for the modeling of amorphous p/i/metal-heterojunctions. Good fits were obtained for the dark and illuminated JV-characteristics of the experimental single-junction solar cell.

The influence of the band discontinuity, the mobility of charge carriers and the interface states on the JV-characteristics of a p/i/metal-structure were presented. From this sensitivity study it is concluded that it is feasible to extract the band lineup of a p/i/metal-structure from its JV-characteristics. Next, the extraction was actually performed on an experimental p/i/metal-structure, by fitting simulated JV-characteristics to measured ones with the inverse modeling technique. The determined band offset agrees within the limits of experimental error with measurements made by X-ray photoelectron spectroscopy [44].

As a cross check, the capacitance as a function of the frequency of the single-junction solar cell was measured. The high-frequency part of this measurement confirms the correctness of the relative dielectric constants used in the modeling, whereas the low-frequency part is presented as a reference for future modeling of the capacitance as a function of the frequency of pin-devices.

Chapter 5

Conclusions and recommendations for future research

5.1 Conclusions

The main conclusions of this work are listed below.

- In literature, two methods are found for the determination of the Tauc optical gap of an amorphous semiconductor. The methods differ in whether the refractive index is or is not taken into account in the determination. Although most authors omit the refractive index for the sake of convenience, from theory it follows that the refractive index must be taken into account. In this work, it is verified that the effect of omitting the refractive index on the Tauc gap is in the order of 0.01 eV, which is negligible compared to the effect of other error sources.
- Tauc's method yields values which depend strongly on, for example, the interpretation of which region can be approximated by a straight line, the sample thickness and on the sensitivity of the measurement setup. In this work it is shown that the determination of the optical gap, both according to Cody and to Klazes, yield less ambiguous results than according to Tauc, because the fitting region of Cody's and Klazes' method is twice as large as that of Tauc's method, and a better fit to a straight line is obtained. Combining results from Jackson and from the author gives rise to a determination of the optical gap as proposed by Cody. Notwithstanding this, the method most often employed to determine the optical gap is Tauc's method, because of historical reasons.

- For the first time, relations between values of the optical gap, found by the methods of Tauc, Klazes and Cody, were determined. We determined these relations from a large set of optical data of over 200 experimental samples, including a-SiGe:H, a-SiC:H, μc-Si:H and μc-SiC:H, doped as well as undoped. The relation between the Klazes and Cody gap is universally applicable to measurements of the optical gap determined by these methods, because of the unambiguous way the gap is determined.
- The relation between the Urbach energy and the optical gap, as found by Cody, only holds for unalloyed amorphous silicon. We show that alloying a-Si:H with germanium or carbon changes the band gap without a corresponding change of the Urbach energy. However, Cody's relation still can serve as a means to couple these two parameters of unalloyed intrinsic layers of a solar cell, thereby quantifying the tradeoff between the electrical and optical properties. From an electrical point of view, the lower the defect density of the intrinsic layer is, the better, because the recombination of photo-generated carriers becomes lower. But, the lower the defect density is, the lower the Urbach energy is. And, from Cody's relation, the lower the Urbach energy is, the higher the optical gap is, and thus the lower the absorption is, which is undesirable, because the lower the absorption, the less the photo-generated current can be.
- The absorption coefficient of a-Si:H can be calculated from the electronic density of states, which procedure serves as a cross check of the optical and electrical input parameters used in the simulation of a-Si:H devices. We fitted the calculated absorption coefficient of intrinsic a-Si:H to the measured absorption coefficient, where values of the total defect density in the gap, the band tail characteristic energies and the value of the gap are obtained. The found value of the valence band tail characteristic energy, 43 meV, is only $\sim$10 % lower than the Urbach energy, because of the relatively small conduction band tail characteristic energy of around 30 meV. The dependence of the optical gap, the mobility gap and the density of defect states on the assumed conduction band tail characteristic energy was found to be negligible. As was expected on theoretical grounds, the value of the valence band tail characteristic energy, found from fitting the absorption coefficient, clearly depends on the assumed conduction band tail characteristic energy.

- Undoped intrinsic a-Si:H and doped amorphous and microcrystalline silicon and silicon carbide films were deposited, and the optical and electrical properties were measured in order to establish the quality and suitability of the films for use in solar cells. The measured properties are the refractive index, the absorption coefficient, the dark and photoconductivity and the temperature dependence of the dark conductivity. The Fermi level position was determined from the temperature dependence of the dark conductivity; the valence and conduction band tail characteristic energies and the defect density in the gap were determined from sub band gap absorption measurements, and the optical gap was determined from the optical absorption. The measured and derived values were used as an input for modeling amorphous silicon devices.
- For p-doped microcrystalline silicon carbide, a transition from microcrystalline to amorphous growth was found at a methane/silane ratio of the source gas of 8 %, where this ratio amounted for n-doped μc-SiC:H to 12 %. In the microcrystalline regime, by adding more methane to the source gas, the films became more transparent, whereas the Fermi level shifted to mid gap, resulting in a lower dark conductivity and higher activation energy of the dark conductivity. Thus, by adding methane to the source gas, the optical properties of the films enhance, whereas the electrical properties worsen. To find an optimum of the electrical properties versus the optical properties, the films must be incorporated in solar cells, and the efficiency and stability of these cells must be determined.
- The Meyer-Neldel rule is the experimentally found linear relation between the prefactor of the dark conductivity and the activation energy of a material. This rule seems to be universally valid for unordered materials such as amorphous silicon, and in this work it is shown that the Meyer-Neldel rule also applies to doped microcrystalline silicon and its carbon alloys.
- With the device simulator ASA, the JV-characteristics of a single-junction solar cell in dark and illuminated with 400 nm and 600 nm monochromatic light were simulated. The set of input parameters was found by the inverse modeling technique, and this set was used as a basis for the simulation of a p/i/metal-heterojunction structure. The band lineup of an experimental p/i/metal-structure was found from its

JV-characteristics with the inverse modeling technique. The found value agrees within experimental error with measurements made by X-ray photoelectron spectroscopy. As a cross check, the capacitance as a function of the frequency of the single-junction solar cell was measured. The high-frequency part of this measurement confirms the correctness of the relative dielectric constants used in the modeling, whereas the low-frequency part is presented as a reference for future modeling of the capacitance as a function of the frequency of pin-devices.

5.2 Recommendations for future research

- The different p-layers described in this thesis should be judged on their merit by applying them in solar cells. Although optical and electrical measurements on the separate films can serve to predict their usefulness in solar cells, the ultimate test of the film quality for solar cell use is by actually applying it in solar cells.
- The more complex the device structure which is simulated is, the more variables enter the device simulation, and the simulations become less reliable and accurate. In order to reduce the number of input parameters, it is recommended that the test devices have a structure as simple as possible. This implicates, for example, the use of devices with abrupt junctions, instead of graded junction devices.
- The more devices described correctly with a certain input parameter set under different illuminations, the higher the degree is of certainty of the parameter set. Therefore, it is desirable to find a parameter set which correctly describes as many different structures, such as pin, pip, nin and p/i/metal, as possible. This requires not only the simultaneous modeling of the dark and illuminated JV-characteristics of one device, but the modeling of more devices simultaneously.
- The integration of optical and electrical modeling in one simulator package is highly desirable to facilitate the modeling of illuminated amorphous silicon devices. Such an integration would, for example, give insight into the dependence of the solar cell efficiency on the band alignment of the p/i-junction, or into the dependence on the mobility gap of the i-layer of the solar cell.

APPENDIX A

PARAMETER EXTRACTION BY MEANS OF INVERSE MODELING

Introduction

Forward modeling is the simulation of the external behavior of a device for given physical parameters and boundary conditions, whereas inverse modeling is the extraction of the internal, physical parameters from the measured, external behavior of this device [142, 143]. In inverse modeling, the input parameters of a forward model are adapted by fitting the simulated results to experimental data by an optimization driver, which minimizes a cost function. This means that internal, physical parameters can be extracted from the measured, external behavior of a device. Of course, the reliability and accuracy of the physical parameters found depend on the correctness of the used forward model.

Some applications of inverse modeling

The method of inverse modeling has been successfully applied in geophysics, which led to important breakthroughs in hydrocarbon exploration [30].

Ouwerling used this approach to determine doping profiles in MOS, Schottky, Junction gates and Junction Charge-Coupled Devices, where Profile was used as an optimization driver and a fast forward Poisson solver was used as the forward model [144].

Van Rijs used the method of inverse modeling to determine the minority carrier mobility, carrier lifetime and band gap narrowing in heavily

doped crystalline silicon, and used Profile as an optimization driver too [163].

The inverse modeling described in this thesis was also carried out with Profile as the optimization driver, where the forward models were, respectively, the calculation of the absorption coefficient as described in section 2.9, and ASA, which is described in appendix B.

Optimization procedure

The parameter optimization driver and the forward model can be two separate entities, in which case the parameter optimization driver does not have to have any knowledge about the inner workings of the forward model. In this case, the driver and the forward model are two separate programs which communicate through files [97, 142]. The interaction between the optimization driver and the forward model is schematically depicted in figure A.1. The optimization driver takes a sequence of steps, where at each step an input parameter is adapted such that the cost function is minimized. Thus the input parameter vector is adapted step by step, until a minimum of the cost function is reached.

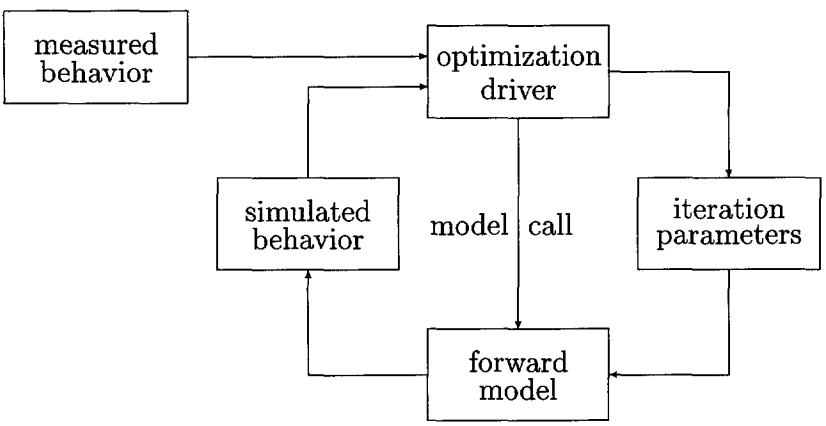

Figure A.1: *Inverse modeling.*

Minimizing the difference between the simulated and measured behavior was done by minimizing the weighted sum of squared differences, which well-known procedure is commonly referred to as a least squares fitting. The least squares error $\xi(\vec{p})$ is given by

$$\xi(\vec{p}) = \frac{1}{N} \sum_{j=1}^{N} w_j^2 [y_j^{meas} - y_j^{model}(\vec{p})]^2, \tag{A.1}$$

where ξ is the cost function,
N is the number of data points,
w_j is the weight factor of a data point j,
y_j^{meas} is the measured value of data point j,
y_j^{model} is the simulated value of data point j and
$\vec{p}$ is the input parameter vector which is adapted.

Generally, it is useful to bring the different measured quantities into the same value range. For functions with an exponential dependence on a parameter, such as the absorption as a function of the photon energy (see section 2.9), or the current density as a function of the applied forward voltage in a diode, the values are brought into the same range by taking the logarithm of the calculated and measured values in the fitting process.

Implementation of the inverse modeling

Minimization of the least squares error constitutes a multi-dimensional nonlinear optimization problem, and several numerical methods for the approximate solution of such problems are available [10, 252]. However these methods were originally developed for use with analytical models, there is no objection to the use of these methods for numerical models. The Modified Damped Least Squares (MDLS) method as originated by Meyer and Roth [115] and described by Wolfe [252] was implemented in the nonlinear optimization driver Profile by Ouwerling [141, 143]. The MDLS method as implemented in Profile is a modification of the Levenberg-Marquardt method [94, 109], where the modification consists of a linear search in the calculated step direction when needed.

A detailed description of the MDLS method as implemented in Profile is given by Ouwerling [144, app. C].

Potential of inverse modeling

In practice, the described technique of inverse modeling allows the simultaneous determination of about maximally five parameters for typical cases as described in this thesis. In this thesis, the determination of the density of states of a semiconductor from the measured absorption spectrum, and the determination of electrical parameters, such as the carrier mobility or mobility gap, from the JV-characteristics, are described. A prerequisite for the determination of several parameters is that the parameters are, at least to some degree, independent from each other.

Appendix B

The Amorphous Semiconductor Analysis program

Introduction

To gain insight into the electronic processes that take place in amorphous silicon devices such as a-Si:H solar cells, electrical simulations can be carried out. Over the past years, several research groups have developed software packages for the electrical modeling of solar cells. An overview of the evolution of these simulation programs is given by Rubinelli et al. [168].

Most of the work done by different research groups is limited to one-dimensional modeling, which is suited to model solar cells on flat substrates. Modeling the behavior of recently introduced structures, such as solar cells on textured substrates, with their typical problems such as pinholes and layer thickness inhomogeneities, requires a two-dimensional approach. Only recently, a Sanyo group presented the results of two dimensional modeling [172].

Because of the steady-state character of power conversion in solar cells, the first method to gain insight into the electrical behavior of these devices is by simulating them with a steady-state simulator. Additionally, transient simulators can be used for simulating transient experiments such as Time-Of-Flight measurements [223, 224, 182] or capacitance measurements, for gaining extra insight into the electrical behavior, or as a cross check of parameters used in steady-state modeling.

The ASA computer code is a one-dimensional steady-state simulator, designed to simulate amorphous silicon devices. It is described in more

detail in the following sections, where the basic equations, the boundary conditions describing the contacts, the numerical solution of the formed mathematical problem and the description of the defect states is treated.

Basic equations

ASA is based on the classical drift-diffusion model and uses the potential ψ, the hole density p and the electron density n as the independent variables. It solves Poisson's equation, the continuity equation for free electrons and the continuity equation for free holes successively.
Poisson's equation in one-dimensional form is

$$\frac{d}{dx}\left(\epsilon \frac{d\psi}{dx}\right) = \rho\,, \tag{B.1}$$

where ϵ is the dielectric permittivity,
ψ is the potential and
ρ is the space charge density.

The space charge density ρ in Poisson's equation is given by

$$\rho = -\frac{q}{\epsilon}\left(p - n + p_{loc} - n_{loc} + N_D - N_A\right), \tag{B.2}$$

where q is the magnitude of the electron charge,
p is the free hole and electron concentrations,
n is the free hole and electron concentrations,
p_{loc} is the hole concentration in localized states,
n_{loc} is the electron concentration in localized states,
N_D is the ionized donor concentration and
N_A is the ionized acceptor concentration.

The free electron and hole concentration in a semiconductor are given by

$$n = \int_{E_C}^{\infty} g_{\mathrm{C}}(E)\cdot f(E)\,dE\,, \tag{B.3}$$

$$p = \int_{-\infty}^{E_V} g_{\mathrm{V}}(E)\cdot[1-f(E)]\,dE\,, \tag{B.4}$$

where $g_C(E)$ is the density of states in the conduction band,
$g_V(E)$ is the density of states in the valence band and
$f(E)$ is the probability that an energy level with energy E is occupied.

For a parabolic density of states, $g_C(E)$ and $g_V(E)$ equal

$$g_C(E) = c_n \cdot \sqrt{E - E_C}\,, \tag{B.5}$$

$$g_V(E) = c_p \cdot \sqrt{E_V - E}\,, \tag{B.6}$$

where c_n and c_p are constants depending on the effective masses of the electrons and holes in the extended states. For crystalline semiconductors, theoretical treatments teach that $g_C(E)$ and $g_V(E)$ are parabolic [157].

The occupation probability function $f(E)$ of fermions, to which class electrons belong, is given by the Fermi-Dirac distribution function:

$$f(E) = \frac{1}{1 + e^{(E-E_F)/kT}}\,. \tag{B.7}$$

Taking this Fermi-Dirac distribution and a parabolic density of states, the concentrations of free electrons n and free holes p are given by

$$n = N_C \frac{2}{\sqrt{\pi}} \mathcal{F}_{1/2}(\eta_n)\,, \tag{B.8}$$

$$p = N_V \frac{2}{\sqrt{\pi}} \mathcal{F}_{1/2}(\eta_p)\,, \tag{B.9}$$

where N_C is the effective density of conduction band states and
N_V is the effective density of valence band states.
$\mathcal{F}_{1/2}$ is the Fermi-Dirac integral of order one-half.

The variables η_n and η_p represent

$$\eta_n = \frac{E_{F_n} - E_C}{kT}\,, \tag{B.10}$$

$$\eta_p = \frac{E_V - E_{F_p}}{kT}\,, \tag{B.11}$$

where E_C is the energy of the conduction band mobility edge and
E_V is the energy of the valence band mobility edge.

The Fermi-Dirac integral of order one-half $\mathcal{F}_{1/2}$ is defined by

$$\mathcal{F}_{1/2}(\eta_s) \equiv \frac{2}{\sqrt{\pi}} \int_0^\infty \frac{\eta^{1/2}}{1 + e^{\eta - \eta_s}} d\eta \,. \tag{B.12}$$

If the semiconductor is non-degenerate, which is usually the case, Maxwell-Boltzmann statistics can be applied, and the Fermi-Dirac integral can be simplified into an exponential:

$$\mathcal{F}_{1/2}(\eta_s) \approx e^{\eta_s} \,. \tag{B.13}$$

In this case, the expressions for the free electron density (equation B.8) and the free hole density (equation B.9) simplify into the commonly encountered forms

$$n = N_C \cdot \exp(\frac{E_{F_n} - E_C}{kT}) \,, \tag{B.14}$$

$$p = N_V \cdot \exp(\frac{E_V - E_{F_p}}{kT}) \,. \tag{B.15}$$

The conduction band energy E_C and the valence band energy E_V are related to the potential ψ and the electron affinity χ as

$$E_C = -q\psi - \chi \,, \tag{B.16}$$

$$E_V = -q\psi - \chi - E_g \,. \tag{B.17}$$

With these expressions for the conduction band energy and valence band energy, the expressions for the free electron density B.14 and the free hole density B.15 become

$$n = N_C \cdot \exp(\frac{E_{F_n} + q\psi + \chi}{kT}) \,, \tag{B.18}$$

$$p = N_V \cdot \exp(\frac{-q\psi - \chi - E_g - E_{F_p}}{kT}) \,. \tag{B.19}$$

Besides Poisson's equation, ASA solves the continuity equations for free electrons and holes, which are

$$-\frac{1}{q}\frac{dJ_n}{dx} = G - R, \tag{B.20}$$

$$\frac{1}{q}\frac{dJ_p}{dx} = G - R, \tag{B.21}$$

where J_n is the electron current density,
J_p is the hole current density,
G is the total generation rate and
R is the total recombination rate.

From the Boltzmann transport theory, the electron and hole current densities can be written as

$$J_n = q\,\mu_n \frac{dE_{F_n}}{dx}, \tag{B.22}$$

$$J_p = q\,\mu_p \frac{dE_{F_p}}{dx}, \tag{B.23}$$

where μ_n, μ_p are the electron and hole mobilities and
E_{F_n}, E_{F_p} are the electron and hole quasi Fermi levels.

By using Maxwell-Boltzmann statistics, the electron and hole current densities given in equations B.22 and B.23 can be written as

$$J_n = -q\,\mu_n\, n \frac{d\psi}{dx} + q\,D_n \frac{dn}{dx}, \tag{B.24}$$

$$J_p = -q\,\mu_p\, p \frac{d\psi}{dx} - q\,D_p \frac{dp}{dx}, \tag{B.25}$$

where D_n and D_p are the electron and hole diffusion coefficients.

In short, ASA solves equations B.1, B.24 and B.25, where the free electron and hole densities are given by B.18 and B.19. When solving these equations, the proper values of the position-dependent mobilities, space charge, recombination and generation rates and the boundary conditions must be evaluated.

Boundary conditions: modeling of the contacts

The interface between the semiconductor device and the outside world is usually formed by metal semiconductor contacts, or by contacts between a transparent conductive oxide and the semiconductor. Such a contact can become a rectifying contact (Schottky contact), or an effective Ohmic contact. Depending on the contact type, rectifying or Ohmic, different boundary conditions must be imposed on the semiconductor equations.

Ideal Ohmic contacts assume an infinite surface recombination velocity, and are described by space charge neutrality at the contacts, and by carrier concentrations which equal their equilibrium values:

$$\rho = 0\,, \tag{B.26}$$

$$n = n_0\,, \tag{B.27}$$

$$p = p_0\,, \tag{B.28}$$

where n_0 and p_0 are the equilibrium electron and hole concentrations.

For general Ohmic contacts, the carrier concentrations at the boundaries are determined by the surface recombination velocities of electrons and holes, S_n and S_p. The equations of the electron and hole current densities at the boundaries of the device become

$$J_n(x=0) = \quad q \cdot S_{n0} \cdot [n(x=0) - n_0(x=0)]\,, \tag{B.29}$$

$$J_p(x=0) = -q \cdot S_{p0} \cdot [p(x=0) - p_0(x=0)]\,, \tag{B.30}$$

$$J_n(x=L) = -q \cdot S_{nL} \cdot [n(x=L) - n_0(x=L)]\,, \tag{B.31}$$

$$J_n(x=L) = \quad q \cdot S_{pL} \cdot [p(x=L) - p_0(x=L)]\,. \tag{B.32}$$

Numerical solution of the semiconductor equations

In order to numerically solve the semiconductor equations, these equations are discretized by finite differencing. The equations are linearized by the approximation of all non-linear terms by their first-order Taylor expansions. The continuity equations are discretized according to the

integral expressions of Scharfetter and Gummel [173] for numerical stability. There are two common approaches to solve the resulting set of algebraic equations.

Firstly, the fully coupled set of equations can be solved [88, 180]. And, secondly, the coupling between the equations can only be partly taken into account, which method is used by Gummel [57, 180].

The Gummel method is an iterative Newton Raphson solution of the three basic equations separately, where the coupling between the equations is partly taken into account.

Both methods use the Newton Raphson iteration method to solve the resulting set of equations.

The advantages of the Gummel method are the relatively simple program coding and the broad range of convergence, which allows the use of relatively poor initial guesses for the independent variables. However, the convergence properties become very poor when the coupling between equations is too strong. This is, for instance, the case with large generation-recombination terms, which occur in the tunneling recombination junction of a-Si:H tandem solar cells [248], in illuminated solar cells, or in solar cells with an applied voltage of more than ~ 0.6 V.

The fully coupled Newton Raphson method shows a much better convergence rate in cases with strong recombination, where Gummel's method fails. However, in the case of the Newton method, the initial guess should be relatively close to the solution. In terms of program complexity and matrix computation time, this algorithm is more elaborate.

Three solution methods are implemented in ASA: the fully coupled Newton Raphson method, the decoupled Gummel method, and a hybrid algorithm in which the fully coupled Newton scheme is preceded by a few Gummel iterations. The latter method is especially useful when a relatively poor initial solution would result in convergence failure with the fully coupled Newton method, and the Gummel method would take numerous iterations, which could be the case in illuminated solar cells.

Modeling of the defect states

The density of states assumed for the modeling of the amorphous semiconductor devices is depicted in figure B.1. The conduction and valence band tails are modeled by exponentially decreasing acceptor-type, respectively donor-type states. The charge occupation and recombination of these defect states are modeled according to Shockley-Read-Hall statistics [185].

The defect states in the gap are represented by two Gaussian distributions at different energies. The concentration of the defect states are calculated from the Urbach energy, as proposed by Stutzmann [209], and treated in section 2.7.2. The Gaussian distributed defect states in the gap, which are amphoteric of character, are modeled with statistics derived for defects with multiple charged states. These statistics were derived by Sah and Shockley [137, 170].

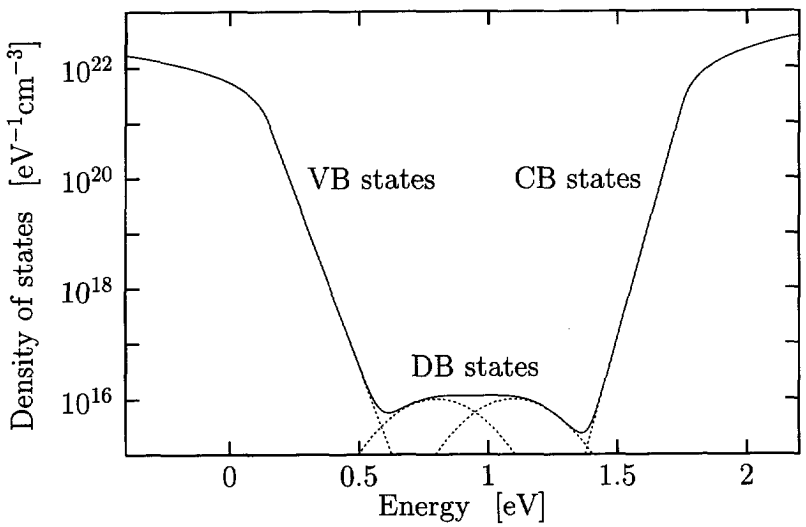

Figure B.1: *Density of states in hydrogenated amorphous silicon. The valence and conduction band tail states are denoted by 'VB states' and 'CB states', respectively, and 'DB states' denote the dangling bond states.*

REFERENCES

[1] B. Abeles, C.R. Wronski, T. Tiedje and G.D. Cody, *Exponential absorption edge in hydrogenated a-Si films*, Solid State Commun. 36 (1980) 537–540.

[2] R.A. Abram and P.J. Doherty, *A Theory of Capacitance-Voltage Measurements on Amorphous Silicon Schottky Barriers*, Phil. Mag. B45 (1982) 413–418.

[3] P.B. Allen and M. Cardona, *Theory of the temperature dependence of the direct gap of germanium*, Phys. Rev. B23 (1981) 1495–1505.

[4] R.L. Anderson, *Experiments on Ge–GaAs Heterojunctions*, Solid-State Electron. 5 (1962) 341–351.

[5] D.A. Anderson and W.E. Spear, *Electrical and Optical properties of amorphous silicon carbide, silicon nitride and germanium carbide by the glow discharge technique*, Phil. Mag. B35 (1977) 1–16.

[6] I.W. Archibald and R.A. Abram, *A theory of the admittance of an amorphous silicon Schottky barrier*, Phil. Mag. B48 (1983) 111–125.

[7] I.W. Archibald and R.A. Abram, *More theory of the admittance of an amorphous silicon Schottky barrier*, Phil. Mag. B54 (1986) 421.

[8] I.W. Archibald and R.A. Abram, *Experimental determination of the density of gap states in amorphous silicon by Schottky barrier admittance*, Phil. Mag. B56 (1987) 429–441.

[9] R.R. Arya, A. Catalano and R.S. Oswald, *Amorphous silicon p-i-n solar cells with graded interface*, Appl. Phys. Lett. 49 (1986) 1089–1091.

[10] Y. Bard, *Nonlinear Parameter Estimation*, Academic Press, New York, 1974.

[11] Y. Bar-Yam, D. Adler and J.D. Joannopoulos, *Structure and Electronic States in Disordered Systems*, Phys. Rev. Lett. 57 (1986) 467–470.

[12] R.S. Bauer and J.C. McMenamin, *Ge-GaAs(110) interface formation*, J. Vac. Sci. and Technol. 15 (1978) 1444–1449.

[13] W. den Boer, *Determination of midgap density of states in a-Si:H using space-charge-limited current measurements*, J. Phys. C4 (1981) 451–454.

[14] W. den Boer, *Interference effects and Space-Charge-Limited Conduction in amorphous silicon devices*, Ph.D. thesis, Delft University of Technology, the Netherlands, 1983.

[15] M.J. v.d. Boogaard, *Microvoids and Hydrogen Diffusion in Hydrogenated Amorphous Silicon*, Ph.D. thesis, Utrecht University, the Netherlands, 1992.

[16] M.H. Brodsky, R.S. Title, *Electron spin resonance in amorphous silicon, germanium, and silicon carbide*, Phys. Rev. Lett. 23 (1969) 581–585.

[17] D.E. Carlson and C.R. Wronski, *Amorphous silicon solar cell*, Appl. Phys. Lett. 28 (1976) 671–673.

[18] D.E. Carlson, *Amorphous Silicon Solar Cells*, IEEE Trans. on Electron Devices ED-24 (1977) 449–453.

[19] D.E. Carlson, *Factors influencing the efficiency of amorphous silicon solar cells*, J. Non-Cryst. Solids 35&36 (1980) 707–717.

[20] B.N. Chapman, *Glow discharge processes*, John Wiley & Sons, New York, 1980.

[21] R.C. Chittick, J.H. Alexander and H.F. Sterling, *The preparation and properties of amorphous silicon*, J. Electrochem. Soc. 116 (1969) 77–81.

[22] T.C. Chuang, L.E. Fennell, W.B. Jackson, J. Levine, M.J. Thompson, H.C. Tuan and R. Weisfield, *Large-area a-Si:H TFT arrays for printing, input scanning and electronic copying applications*, J. Non-Cryst. Solids 97&98 (1987) 301–304.

[23] G.D. Cody, B. Abeles, C.R. Wronski, R.B. Stevens and B. Brooks, *Optical characterization of amorphous silicon hydride films*, Solar Cells 2 (1980) 227–243.

[24] G.D. Cody, T. Tiedje, B. Abeles, B. Brooks and Y. Goldstein, *Disorder and the Optical-Absorption Edge of Hydrogenated Amorphous Silicon*, Phys. Rev. Lett. 47 (1981) 1480–1483.

[25] G.D. Cody, T. Tiedje, T.D. Moustakas, B. Abeles, B. Brooks and Y. Goldstein, *Disorder and the optical absorption edge of hydrogenated amorphous silicon*, J. Phys. C4 (1981) 301–304.

[26] G.D. Cody, B.G. Brooks and B. Abeles, *Optical absorption above the optical gap of amorphous silicon hydride*, Solar Energy Mater. 8 (1982) 231–240.

[27] G.D. Cody, *The optical absorption edge*, in Semiconductors and Semimetals, Vol. 21, Part B, ed. J.I. Pankove, Academic Press, New York, U.S.A., 1984, 11–82.

[28] M.H. Cohen, H. Fritzche and S.R. Ovshinsky, *Simple band model for amorphous semiconducting alloys*, Phys. Rev. Lett. 22 (1969) 1065–1068.

[29] Corning glass: for information: Materials Division Europe, BP61 77211 AVON, France.

[30] W. Crans and A.J. Berkhout, *Assessment of seismic amplitude anomalies*, The Oil & Gas Journal, November 17 (1980) 156–166.

[31] B.L. Crowder, R.S. Title, M.H. Brodsky, G.D. Pettit, *ESR and optical studies of ion-implanted silicon*, Appl. Phys. Lett. 16 (1970) 205–208.

[32] H. Curtins, N. Wyrsch and A. Shah, *Influence of plasma excitation frequency on deposition rate and on film properties for hydrogenated amorphous silicon*, Mat. Res. Soc. Symp. Proc. 95 (1987) 249–253.

[33] E.A. Davis and N.F. Mott, *Conduction in Non-crystalline Systems, V. Conductivity, Optical Absorption and Photoconductivity in Amorphous Semiconductors*, Phil. Mag. 22 (1970) 903–922.

[34] A. Derrick, R.W. Barlow, B. McNelis and J.A. Gregory, *Photovoltaics: A Market Overview*, James & James Science Publishers Ltd., London, 1993, 13.

[35] R.E. Denton, R.D. Campbell and S.G. Tomlin, *The determination of the optical constants of thin films from measurements of reflectance and transmittance at normal incidence*, J. Phys. D5 (1972) 852–863.

[36] R. Dingle, H.L. Stormer, A.C. Gossard and W. Wiegmann, *Electron mobilities in modulation-doped heterojunction superlattices*, Appl. Phys. Lett. 33 (1978) 665–667.

[37] F. Djamdji and P.G. LeComber, *An investigation of the conductivity prefactor in a-Si as a function of Fermi level position using the field-effect experiment*, Phil. Mag. B56 (1983) 31–50.

[38] T. Drüsedau and R. Bindemann, *The Meyer-Neldel Rule and the Fundamental Pre-Exponential Factor in the Conductivity of a-Si:H*, Phys. Stat. Sol. B136 (1986) K61-K69.

[39] J.C. Dyre, *A phenomenological model for the Meyer-Neldel rule*, J. Phys. C19 (1986) 5655–5664.

[40] EMIS Datareviews series no. 1, *Properties of Amorphous Silicon*, Inspec, The Gresham Press, Surrey, England, 1989.

[41] L. Esaki and R. Tsu, *Superlattice and Negative Conductivity in Semiconductors*, IBM Research, Internal Report RC2418, 1969.

[42] J.M. Essick and J.D. Cohen, *Band offsets and anomalous deep defect distribution at the hydrogenated amorphous silicon-crystalline silicon interface via junction capacitance techniques*, Mat. Res. Soc. Symp. Proc. 149 (1989) 699–704.

[43] F. Evangelisti, P. Fiorini, C. Giovannella, F. Patella, P. Perfetti, C. Quaresima and M. Capozi, *Photoemission studies of a-Si_xC_{1-x}:H/a-Si and a-Si_xC_{1-x}:H/ hydrogenated amorphous silicon junctions*, Appl. Phys. Lett. 44 (1984) 764–766.

[44] F. Evangelisti, *Photoemission studies of amorphous semiconductor heterojunctions*, J. Non-Cryst. Solids 77&78 (1985) 969–977.

[45] M. Faraji, S.V. Rajarshi, V.G. Bhide, S.V. Ghaisas and S.T. Kshirsagar, *Preparation of high conductivity and large band gap p-type a-Si:H films produced by high dilution of silane at low rf power*, Techn. Digest of the 6th Intern. Photovoltaic Science and Engineering Conf., New Delhi, India (1992) 481–485.

[46] D.L. Flamm, *Frequency effects in plasma etching*, J. Vac. Technol. A4 (1986) 729–738.

[47] H. Fritzsche, *Amorphous and Liquid Semiconductors*, ed. J. Tauc, Plenum Press, London, New York, 1974.

[48] H. Fritzsche and N. Ibaraki, *Thermostimulated conductivity in amorphous semiconductors*, Phil. Mag. B52 (1985) 299–311.

[49] I. Gianinoni and M. Musci, *Laser-assisted* CVD *of amorphous materials*, J. Non-Cryst. Solids 77&78 (1985) 743–752.

[50] R.W. Grant, J.R. Waldrop and E.A. Kraut, *Observation of the Orientation Dependence of Interface Dipole Energies in Ge-GaAs*, Phys. Rev. Lett. 40 (1978) 656–659.

[51] M.A. Green, *Solar Cells*, University of New South Wales, England, 1986, 189.

[52] M.A. Green, *Intrinsic concentration, effective densities of states, and effective mass in silicon*, J. Appl. Phys. 67 (1990) 2944–2954.

[53] D.A. Greenwood, *The Bolzmann Equation in the Theory of Electrical Conduction in Metals*, Proc. Phys. Soc. London 71 (1958) 585–596.

[54] S. Griep and L. Ley, *Direct spectroscopic determination of the distribution of occupied gap states in a-Si:H*, J. Non-Cryst. Solids 59&60 (1983) 253–256.

[55] R. Grigorovici, *Amorphous Germanium and Silicon (Structure and Transport Phenomena)*, Mat. Res. Bull. 3 (1968) 13–24.

[56] H.G. Grimmeiss and L-Å. Ledebo, *Spectral distribution of photoionization cross sections by photoconductivity measurements*, J. Appl. Phys. 46 (1975) 2155–2162.

[57] H.K. Gummel, *A Self-Consistent Iterative Scheme for One-Dimensional Steady State Transistor Calculations*, IEEE Trans. on Electron Devices ED-11 (1964) 455–465.

[58] M. Hack and M. Shur, *Physics of amorphous silicon alloy p-i-n solar cells*, J. Appl. Phys. 58 (1985) 997–1020.

[59] M. Hack and M. Shur, Appl. Phys. Lett. 49 (1986) 1432.

[60] Y. Hamakawa, *Present status of solar photovoltaic R&D projects in Japan*, Surface Sci. 86 (1979) 444–461.

[61] Y. Hamakawa, H. Okamoto and Y. Nitta, *A new type of amorphous silicon photovoltaic cell generating more than 2.0 V*, Appl. Phys. Lett. 35 (1979) 187–189.

[62] Y. Hamakawa, Y. Matsumoto, G. Hirata and H. Okamoto, *Optoelectronics and Photovoltaic Applications of Microcrystalline SiC*, Mat. Res. Soc. Symp. Proc. 164 (1990) 291–301.

[63] Y. Hamakawa, *Recent Progress of amorphous silicon solar cell technology in Japan*, Proc. of the 22nd IEEE Photovoltaic Specialists Conf. (1991) 1199–1206.

[64] Y. Hattori, D. Kruangam, K. Katoh, Y. Nitta, H. Okamoto and Y. Hamakawa, *High-conductive wide band gap p-type a-SiC:H prepared by ECR CVD and its application to high efficiency a-Si basis solar cells*, Proc. of the 19th IEEE Photovoltaic Specialists Conf., New Orleans, U.S.A. (1987) 689–694.

[65] Y. Hattori, D. Kruangam, T. Toyama, H. Okamoto and Y. Hamakawa, *High Efficiency Amorphous Heterojunction Solar Cell Employing ECR-CVD Produced p-type Microcrystalline SiC Film*, Techn. Digest of the 3rd Intern. Photovoltaic Science and Engineering Conf., Tokyo (1987) 171–174.

[66] S.S. Hegedus, *Capacitance studies of a-SiGe:H p-i-n solar cells*, Proc. 21th IEEE Photovoltaic Specialists Conf. (1990) 1544–1549.

[67] J. v.d. Heuvel, *Optical properties and Transport Properties of Hydrogenated Amorphous Silicon*, Ph.D. thesis, Delft University of Technology, the Netherlands, 1989.

[68] J. Hilibrand and R.D. Gold, *Determination of the impurity distribution in junction diodes from capacitance-voltage measurements*, RCA Review 21 (1960) 25–252.

[69] R.E. Hollingsworth, P.K. Bhat and A. Madan, *Microcrystalline and wide band gap p^+ window layers for a-Si p-i-n solar cells*, J. Non-Cryst. Solids 97&98 (1987) 309–312.

[70] P. Irsigler, D. Wagner and D.J. Dunstan, *On the application of the Meyer-Neldel rule to a-Si:H*, J. Phys. C16 (1983) 6605–6613.

[71] M. Isomura, T. Takahama, S. Tsuda and S. Nakano, *Dependence of Open Circuit Voltage of Amorphous Silicon Solar Cells on Thickness and Doping Level of the p-Layer*, Jap. J. Appl. Phys. 32 (1993) 1902–1907.

[72] W.B. Jackson, N.M. Amer, A.C. Boccora and D. Fournier, *Photothermal deflection spectroscopy and detection*, Appl. Optics 20 (1981) 1333–1344.

[73] W.B. Jackson and N.M. Amer, *Sub-bandgap and band edge optical absorption in a-Si:H by photothermal deflection spectroscopy*, J. Phys. C4 (1981) 293–296.

[74] W.B. Jackson and N.M. Amer, *Direct measurement of gap-state absorption in hydrogenated amorphous silicon by photothermal deflection spectroscopy*, Phys. Rev. B25 (1982) 5559–5562.

[75] W.B. Jackson, S.M. Kelso, C.C. Tsai, J.W. Allen and S.-J. Oh, *Energy dependence of the optical matrix element in hydrogenated amorphous and crystalline silicon*, Phys. Rev. B31 (1985) 5187–5197.

[76] D.I. Jones, P.G. LeComber and W.E. Spear, *Thermoelectric power in phosphorus doped amorphous silicon*, Phil. Mag. 36 (1977) 541–551.

[77] J. Kanicki, C.M. Ransom, W. Bauhofer, T.I. Chappel and B.A. Scott, *Transport Properties and Defect States of a-Si:H Grown by* HOMOCVD, J. Non-Cryst. Solids 66 (1984) 51–58.

[78] J. Kanicki, *Minority Carrier Injection and Series Resistance Effects in Hydrogenated Amorphous Silicon Schottky barrier Diodes*, Mat. Res. Soc. Symp. Proc. 49 (1988) 101–109.

[79] J. Kanicki, E. Hasan, D.F. Kotecki, T. Takamori and J. Griffith *Properties and application of undoped hydrogenated microcrystalline silicon thin films*, Mat. Res. Soc. Symp. Proc. 149 (1989) 173–179.

[80] J. Kanicki, E. Hasan, J.H. Griffith, T. Takamori and J.C. Tsang, *Properties of high conductivity phosphorus doped hydrogenated microcrystalline silicon and application in thin film transistor technology*, Mat. Res. Soc. Symp. Proc. 149 (1989) 239–246.

[81] J. Kanicki, editor, *Amorphous & Microcrystalline Semiconductor Devices, Optoelectronic Devices*, Artech House, Boston, London, 1991.

[82] J. Kanicki, editor, *Amorphous & Microcrystalline Semiconductor Devices, Volume II: Materials and Device Physics*, Artech House, Boston, London, 1992.

[83] R.H. Klazes, M.H.L.M. van den Broek, J. Bezemer and S. Radelaar, *Determination of the optical bandgap of amorphous silicon*, Phil. Mag. B45 (1982) 377–383.

[84] J. Kolodzey, R. Schwarz, S. Aljishi, V. Chu, D.S. Shen, P.M. Fauchet and S. Wagner, *Optical and electronic properties of an amorphous silicon-germanium alloy with a 1.28 eV optical gap*, Appl. Phys. Lett. 52 (1988) 477–479.

[85] W.J. Kopetzky and R Schwartz, *Influence of the Buffer Layer of a-SiC:H/a-Si:H pin Solar Cells on the Spectral Response*, Proc. of the Tenth E.C. Photovoltaic Solar Energy Conf., Lisbon (1991) 188–191.

[86] D. Kruangam, T. Endo, Wei Guang-Pu, H.Okamoto and Y. Hamakawa, *Visible Light Injection-Electroluminescent a-SiC/p-i-n Diode*, Jap. J. Appl. Phys. 24 (1985) L806-L808.

[87] R. Kubo, *Statistical-Mechanical Theory of Irreversible Processes. I.*, J. Phys. Soc. Jap. 12 (1957) 570–586.

[88] M. Kurata, *Numerical Analysis for Semiconductor Devices*, Lexington Books, Lexington, MA, 1982.

[89] G.E.N. Landweer, *The Application of Amorphous Silicon in Solar Cells*, Ph.D. thesis, Utrecht University, the Netherlands, 1990.

[90] D.V. Lang, J.D. Cohen and J.P. Harbison, *Measurements of the density of gap states in hydrogenated amorphous silicon by space charge spectroscopy*, Phys. Rev. B25 (1982) 5285–5320.

[91] P.G. LeComber, *Focussed session on device physics*, J. Non-Cryst. Solids 97&98 (1987) 325–327.

[92] S. Lee, S. Kumar, C.R. Wronski and N. Maley, *A critical investigation of a-Si:H photoconductivity generated by subgap absorption of light*, J. Non-Cryst. Solids 114 (1989) 316–319.

[93] D.R. Lee, C.H. Bjorkman and G. Lucovsky, *Effective electron affinities in doped a-Si:H and μc-Si films as determined from studies of* MOS *capacitors*, J. Non-Cryst. Solids 137&138 (1991) 1059–1062.

[94] K. Levenberg, *A method for the solution of certain nonlinear problems in least squares*, Quarterly of Applied Mathemathics 2 (1944) 164–168.

[95] L. Ley, *Photoemission and Optical Properties*, in The Physics of Hydrogenated Amorphous Silicon II, ed. J.D. Joannopoulos and G. Luconvsky, Springer-Verlag, Berlin, 1984, 61–168.

[96] K.S. Lim, M. Konagai and K. Takahashi, *A novel structure, high conversion efficiency p-SiC/graded p-SiC/i-Si/n-Si/metal substrate-type amorphous silicon solar cell*, J. Appl. Phys. 56 (1984) 538–542.

[97] P. Lloyd, E.J. Prendergast and K. Singhal, *Technology CAD for competitive products*, Proc. 3rd Conf. on Simul. of Semicond. Dev. and Proc. (SISDEP-88), ed. G. Baccarani and M. Rudan, Bologna (1988) 111–126.

[98] C. Longeaud, J. Baixeras, E. Arene and D. Mencaraglia, *Influence of hydrogen on electronic transport in dc triode sputtered amorphous silicon*, J. Appl. Phys. 55 (1984) 1508–1512.

[99] R.J. Loveland, W.E. Spear and A. Al-Sharbaty, *Photoconductivity and absorption in amorphous Si*, J. Non-Cryst. Solids 13 (1973) 55–68.

[100] G. Lucovsky and H. Overhof, *An Application of the Statistical Shift Model to the Inverted Meyer-Neldel, M-N, Relationship in Heavily-Doped Microcrystalline Si, μc-Si*, J. Non-Cryst. Solids 164–166 (1993) 973–976.

[101] A. Madan, S.R. Ovshinsky and E. Benn, *Electrical and optical properties of amorphous Si:F:H alloys*, Phil. Mag. 40 (1979) 259–277.

[102] A. Madan, J. McGill, W. Czunatyj, J. Yang, S.R. Ovshinsky, *Metal-insulator-semiconductor solar cells using amorphous Si:F:H alloys*, Appl. Phys. Lett. 37 (1980) 826–828.

[103] A. Madan and M.P. Shaw, *The Physics and Applications of Amorphous Semiconductors*, Academic Press, Boston, 1988,

[104] A. Madan, P. Rava, R.E.I. Schropp and B. von Roedern, *A new modular multichamber plasma enhanced chemical vapor deposition system*, Appl. Surf. Science 70/71 (1993) 716–721.

[105] K.M.H. Maessen, *Hydrogenated Amorphous Silicon: Structure and Optical Properties*, Ph.D. thesis, Utrecht University, the Netherlands, 1988.

[106] J. Magarino, D. Kaplan, A. Friedrich and A. Deneuville, *Doping effects on post-hydrogenated chemical-vapour-deposited amorphous silicon*, Phil. Mag. B45 (1982) 285–306.

[107] G. Margaritondo, *Microscopic investigations of semiconductor interfaces*, Solid-State Electron. 26 (1983) 499–513.

[108] A.H. Mahan, J. Carapella, B.P. Nelson and R.S. Crandall, *Deposition of device quality, low H content amorphous silicon*, Appl. Phys. Lett. 69 (1991) 6728–6730.

[109] D.W. Marquardt, *An algorithm for least squares estimation of nonlinear parameters*, Journal of the Society for Industrial and Applied Mathematics (SIAM) 11 (1963) 431–444.

[110] A. Matsuda, S. Yamasaki, K. Nakayama, H. Okushi, K. Tanaka, S. Iizima, M. Matsumura and H. Yamamoto, *Electrical and Structural Properties of Phosphorus-Doped Glow-Discharge Si:F:H and Si:H Films*, Jap. J. Appl. Phys. 19 (1980) L305-L308.

[111] A. Matsuda, M. Matsumura, S. Yamasaki, H. Yamamoto, T. Imura, H. Okushi, S. Iizima and K. Tanaka, *Boron Doping of Hydrogenated Silicon Thin Films*, Jap. J. Appl. Phys. 20 (1981) L183-L186.

[112] A. Matsuda, *Formation kinetics and control of microcrystallite in μc-Si:H from glow discharge plasma*, J. Non-Cryst. Solids 59&60 (1983) 767–774.

[113] M. Matsumura, S. Sekine, J. Yue and Y. Takeuchi, *Device Physics of a-Si:H Charge-Coupled Devices*, J. Non-Cryst. Solids 97&98 (1987) 1299–1302.

[114] W. Meyer and H. Neldel, *Über die Beziehungen zwischen der Energiekonstanten ε und der Mengenkonstanten a in der Leitwerts Temperaturformel bei oxydischen Halbleitern*, Z. Tech. Phys. 18 (1937) 588–593.

[115] R.R. Meyer and P.M. Roth, *Modified Damped Least Squares: an algorithm for nonlinear optimization*, Journal of the Institute of Mathematics and its Applications 9 (1972) 218–233.

[116] H. Mimura and Y. Hatanaka, *Energy-band discontinuities in a heterojunction of amorphous hydrogenated Si and crystalline Si measured by internal photoemission*, Appl. Phys. Lett. 50 (1987) 326–328.

[117] Y. Mishima, S. Miyazaki, M. Hirose and Y. Osaka, *Characterization of plasma-deposited microcrystalline silicon*, Phil. Mag. B46 (1982) 1–12.

[118] K. Miyachi, N. Ishiguro, T. Miyashita, N, Yanagawa, H. Tanaka, M. Koyama, Y. Ashida and N. Fukada, *Fabrication of single pin solar cells with a high conversion efficiency of 13.0 %*, Proc. of the Eleventh E.C. Photovoltaic Solar Energy Conf., Montreux, Swiss (1992) 88–91.

[119] G. Moddel, D.A. Anderson, W. Paul, *Derivation of the low-energy optical-absorption spectra of a-Si:H from photoconductivity*, Phys. Rev. B22 (1980) 1918–1925.

[120] H.J. Möller, *Semiconductors for Solar Cells*, Artech House, Boston, London, 1993, 234.

[121] A. Morimoto, T. Miura, M. Kumeda and T. Shimizu, *Defects in hydrogenated amorphous silicon-carbon alloy films prepared by glow discharge decomposition and sputtering*, J. Appl. Phys. 53 (1982) 7299–7305.

[122] J. Morris, R.R. Arya, J.G. O'Dowd and S. Wiedeman, *Absorption enhancement in hydrogenated amorphous silicon-based solar cells*, J. Appl. Phys. 67 (1990) 1079–1087.

[123] N.F. Mott and E.A. Davis, *Conduction in Non-crystalline Systems. II. The Metal-insulator Transition in a Random Array of Centres*, Phil. Mag. 17 (1968) 1269–1284.

[124] N.F. Mott, *Conduction in Non-crystalline Materials, III. Localized States in a Pseudogap and Near Extremities of Conduction and Valence Bands*, Phil. Mag. 19 (1969) 835–852.

[125] N.F. Mott, *Introductory talk: conduction in non-crystalline materials*, J. Non-Cryst. Solids 8–10 (1972) 1–18.

[126] N.F. Mott and E.A. Davis, *Electronic Processes in Non-crystalline Materials*, Clarendon Press, Oxford, U.K., 1979.

[127] G. Müller, H. Mannsperger and S. Kalbitzer, *Substitutional doping of amorphous silicon, A comparison of different doping mechanisms*, Phil. Mag. B53 (1986) 257–268.

[128] G. Müller, *Equilibrium Dangling Bond Densities in a-Si:H and Its Related Thin-Film Alloys*, Appl. Phys. A45 (1988) 103–107.

[129] G. Nakamura, K. Sato and Y. Yukimoto, *High performance tandem type amorphous solar cells*, Proc. of the 16nd IEEE Photovoltaic Specialists Conf., San Diego, USA (1982) 1331–1337.

[130] G. Nakamura, K. Sato, T. Ishihara, M. Usui, K. Okaniwa and Y. Yukimoto, *Tandem type amorphous solar cells*, J. Non-Cryst. Solids 59&60 (1983) 1111–1114.

[131] F. Nakabeppu, T. Ishimura, K. Kumagai and K. Fukui, *Development of the very thin microcrystalline n-layer and its application to the stacked solar cell*, Mat. Res. Soc. Symp. Proc. 164 (1990) 389–393.

[132] S. Nonomura, K. Fukumoto, H. Okamoto and Y. Hamakawa, *Back surface reflected electroabsorption as a new characterization method of internal potential in a-Si homo- and hetero-junction*, J. Non-Cryst. Solids 59&60 (1983) 1099–1102.

[133] S. Oda, J. Noda and M. Matsumura, *Preparation of a-Si:H films by* VHF *plasma cvd*, Mat. Res. Soc. Symp. Proc. 118 (1988) 117–122.

[134] S. Oda and M. Yasukawa, *High quality a-Si:H films and interfaces prepared by VHF plasma CVD*, J. Non-Cryst. Solids 137&138 (1991) 677–680.

[135] H. Okamoto, Y. Nitta, T. Adachi and Y. Hamakawa, *Glow discharge produced amorphous silicon solar cells*, Surface Sci. 86 (1979) 486–491.

[136] H. Okamoto, Y. Nitta, T. Yamagushi and Y. Hamakawa, *Device physics and design of a-Si ITO/p-i-n heteroface solar cells*, Solar Energy Mater. 2 (1980) 313–325.

[137] H. Okamoto, H. Kida and Y. Hamakawa, *Steady-state photoconductivity in amorphous semiconductors containing correlated defects*, Phil. Mag. 49 (1984) 231–247.

[138] M. Ondris and W. den Boer, *Hydrogenated a-Si multi-junction solar cells and interference effects in the spectral response*, Proc. of the Third E.C. Photovoltaic Solar Energy Conf., Cannes, France (1980) 809–814.

[139] R.C. van Oort, *Hydrogenated amorphous and microcrystalline silicon deposited from silane-hydrogen mixtures*, Ph.D. thesis, Delft University of Technology, the Netherlands, 1989.

[140] Y. Osaka and T. Imura, in Amorphous Semiconductor Technologies & Devices, Ed. Y. Hamakawa, (1984) 80.

[141] G.J.L. Ouwerling, *The Profile/Prof2d User Manual*, Delft University of Technology, 1987.

[142] G.J.L. Ouwerling, F. van Rijs, H.M. Wentinck, J.C. Staalenburg and W. Crans, *Physical parameter extraction by inverse modelling of semiconductor devices*, Proc. 3rd Conf. on Simul. of Semicond. Dev. and Proc. (SISDEP-88), ed. G. Baccarani and M. Rudan, Bologna (1988) 599–610.

[143] G.J.L. Ouwerling, F. van Rijs, B.F.P. Jansen and W. Crans. *Inverse modelling with the Profile optimization driver*, Digest of the NASECODE VI Software Forum, Part: Short Course on Software Tools for Process, Device and Circuit Modelling, ed. W. Crans, Boole Press, Dublin, 1989.

[144] G.J.L. Ouwerling, *Nondestructive one- and two-dimensional doping profiling by inverse methods*, Ph.D. thesis, Delft University of Technology, the Netherlands, 1989.

[145] H. Overhof and W. Beyer, *Density of states in amorphous silicon determined from transport experiments*, J. Non-Cryst. Solids 35&36 (1980) 375–380.

[146] H. Overhof and W. Beyer, *A model for the electronic transport in hydrogenated amorphous silicon*, Phil. Mag. B43 (1981) 433–450.

[147] H. Overhof and W. Beyer, *Electronic transport in hydrogenated amorphous silicon*, Phil. Mag. B47 (1983) 377–392.

[148] G. Oversluizen, R.P. van Kessel, K.J. Oversteeg and J. Boogaard, *The Meyer-Neldel rule in hydrogenated amorphous silicon nin devices*, J. Appl. Phys. 69 (1991) 3082–3086.

[149] G. Oversluizen, K.J.B.M. Oversteeg and J. Boogaard, *Meyer-Neldel rule in the space-charge-limited conduction of hydrogenated amorphous silicon*, Appl. Phys. Lett. 59 (1991) 312–314.

[150] J.S. Park, M.K. Han and C.H. Lee, *Light-induced effects on doped- and undoped-hydrogenated amorphous silicon*, J. Appl. Phys. 64 (1988) 2107–2112.

[151] W. Paul and D.A. Anderson, *Properties of Amorphous Hydrogenated Silicon, with special emphasis on Preparation by Sputtering*, Solar Energy Mater. 5 (1981) 229–316.

[152] W. Paul, J.H. Chen, E.Z. Liu, A.E. Wetsel and P. Wickboldt, *Structural and Electronic Properties of Amorphous SiGe:H Alloys*, J. Non-Cryst. Solids 164–166 (1993) 1–10.

[153] V. Perez-Mendez, G. Cho, J. Drewery, T. Jing, S.N. Kaplan, S. Qureshi and D. Wildermuth, *Amorphous silicon based radiation detectors*, J. Non-Cryst. Solids 137&138 (1991) 1291–1296.

[154] P. Perfetti, D. Denley, K.A. Mills and D.A. Shirley, *Angle-resolved photoemission measurements of band discontinuities in the GaAs-Ge heterojunction*, Appl. Phys. Lett. 33 (1978) 667–670.

[155] for example sold by Phototronics Solartechnik GmbH, Hermann-Oberth-Strasse 9, D-80–11 Putzbrunn, phone 089/45660–307, fax 089/45660–332

[156] W. Pickin, J.C. Alonso and D. Mendoza, *On the constant Photoconductivity method in amorphous semiconductors*, J. Phys. C20 (1987) L341-L345.

[157] R.F. Pierret, *Advanced semiconductor fundamentals*, Addison-Wesley Publishing Co., Reading, Massachusetts, 1987.

[158] R.F. Pierret, *Semiconductor fundamentals*, Addison-Wesley Publishing Co., Reading, Massachusetts, 1988, 70–72.

[159] F.L. Pilar, *Elementary quantum chemistry*, McGraw-Hill Book Co., New York, 1968, 500.

[160] J.E. Potts, E.M. Peterson, J.A. McMillan, *Effects of rf power and reactant gas pressure on plasma deposited amorphous hydrogenated silicon*, J. Appl. Phys. 52 (1981) 6665–6672.

[161] K. Prasad, U. Kroll, F. Finger, A. Shah, J-L. Dorier, A. Howling, J. Baumann and M. Schubert, *Highly conductive microcrystalline silicon layers for tunnel junctions in stacked amorphous silicon based solar cells*, Mat. Res. Soc. Symp. Proc. 219 (1991) 469–474.

[162] H. Richter and L. Ley, *Optical properties and transport in microcrystalline prepared at temperatures below 400 °C*, J. Appl. Phys. 52 (1981) 7281–7286.

[163] F. v. Rijs, *Measurement of minority carrier mobility, carrier lifetime and bandgap narrowing in heavily doped silicon*, Ph.D. thesis, Delft University of Technology, the Netherlands, 1992.

[164] G.G. Roberts, *Temperature dependent electronic conduction in semiconductors*, Phys. Rep. 60 (1980) 59–150.

[165] A. Rose, in *Concepts in Photoconductivity and Allied Problems*, Wiley, New York 1963.

[166] R.C. Ross and J. Jaklik Jr., *Plasma polymerization and deposition of amorphous hydrogenated silicon thin films from fr and dc silane plasmas*, J. Appl. Phys. 55 (1984) 3785–3794.

[167] A. Rothwarf, *A mechanism for enhanced recombination at the p-i junction of a-Si:H solar cells*, Proc. of the 20th IEEE Photovoltaic Specialists Conf. (1988) 166–170.

[168] F.A. Rubinelli, S.J. Fonash and J.K. Arch, *Computer modeling of solar cell structures*, Techn. Digest of the 6th Intern. Photovoltaic Science and Engineering Conf., New Delhi, India (1992) 811–819.

[169] W.R. Runyan, *Semiconductor Measurements and Instrumentation*, McGraw-Hill, New York, 1975, chap. 3.

[170] C.T. Sah and W. Shockley, *Electron-Hole Recombination Statistics in Semiconductors through Flaws with Many Charge Conditions*, Phys. Rev. 109 (1958) 1103–1115.

[171] T. Saitoh, S. Muramatsu, T. Shimada and M. Migitaka, *Optical and electrical properties of amorphous silicon films prepared by photochemical vapor deposition*, Appl. Phys. Lett. 42 (1983) 678–679.

[172] T. Sawada, H. Tarui, N. Terada, M. Tanaka, T. Takahama, S. Tsuda and S. Nakano, *Theoretical analysis of textured thin-film solar cells and a guideline*

to achieving higher efficiency, Proc. of the 23rd IEEE Photovoltaic Specialists Conf. (1993) 1–8.

[173] D.L. Scharfetter and H.K. Gummel, *Large-Signal Analysis of a Silicon Read Diode Oscillator*, IEEE Trans. on Electron Devices ED-16 (1969) 64–77.

[174] M.P. Schmidt, J. Bullot, M. Gauthier, P. Cordier, I. Solomon and H. Tran-Quoc, *Influence of carbon incorporation in amorphous hydrogenated silicon*, Phil. Mag. B51 (1985) 581–589.

[175] W. Schottky, *Vereinfachte und Erweiterte Theorie der Randschichtgleichrichter*, Zeitschrift für Physik 118 (1942) 539.

[176] R.E.I. Schropp, J. Bezemer, W.G.J.H.M van Sark, H. Meiling, M.B.von der Linden, W.F. van der Weg, J.W. Metselaar, G. Tao, M. Trijssenaar, G.E.N. Landweer and M. Zeman, *Amorf silicium zonnecellen en materialen; onderzoek bij RUU en TUD*, Proc. of the Derde Nationale Zonne-energie Conferentie, Noordwijkerhout, the Netherlands (1991) 120–124.

[177] G. Schumm and G.H. Bauer, *Equilibrium and Non-Equilibrium Gap State Distribution in a-Si:H*, J. Non-Cryst. Solids 137&138 (1991) 315–318.

[178] B.A. Scott, R.M. Plecenik and E.E. Simonyi, *Kinetics and mechanism of amorphous hydrogenated silicon growth by homogeneous chemical vapor deposition*, Appl. Phys. Lett. 39 (1981) 73–75.

[179] B.A. Scott, *Homogeneous Chemical Vapor Deposition*, in Semiconductors and Semimetals, Vol. 21, Part A, ed. J. Pankove, Academic Press, Orlando, U.S.A. (1984) 123.

[180] S. Selberherr, *Analysis and Simulation of Semiconductor Devices*, Springer Verlag, Wien, 1984.

[181] A. Shah, J. Dutta, N. Wyrsch, K. Prasad, H. Curtins, F. Finger, A. Howling and C. Hollenstein, *VHF Plasma deposition: a comparative overview*, Mat. Res. Soc. Symp. Proc. 258 (1992) 15–26.

[182] F.R. Shapiro, *Computer Simulation of the transient response of amorphous silicon hydride devices*, Ph.D. Thesis, Massachusetts Institute of Technology, USA, 1988, private communication

[183] T. Shimada, S. Matsubara, H. Itoh and S. Muramatsu, *Structural and Photoelectric Properties of Ultra Thin Silicon Films prepared by Glow Discharge Method under Microcrystalline-Formation Conditions*, Proc. of the Nineth E.C. Photovoltaic Solar Energy Conf., Freiburg, (1990) 81–83.

[184] J. Shirafuji, S. Nagata and M. Kuwagaki, *Effect of hydrogen dilution of silane on optoelectronic properties in glow-discharged hydrogenated silicon films*, J. Appl. Phys. 58 (1985) 3661–3663.

[185] W. Shockley and W.T. Read, *Statistics of the recombinations of holes and electrons*, Phys. Rev. 87 (1952) 835–842.

[186] J.G. Simmons, G.W. Taylor and M.C. Tam, *Thermally Stimulated Currents in Semiconductors and Insulators Having Arbitrary Trap Distributions*, Phys. Rev. B7 (1973) 3714–3719.

[187] J. Singh and M.H. Cohen, *Capacitance-Voltage Measurements in Amorphous Schottky Barriers*, J. Appl. Phys. 51 (1980) 413–418.

[188] A. Skumanich and N.M. Amer, *Evidence for the intrinsic nature of light-induced defects in undoped a-Si:H*, Phys. Rev. B37 (1988) 8465–8467.

[189] Z.E. Smith and S. Wagner, *Band Tails, Entropy, and Equilibrium Defects in Hydrogenated Amorphous Silicon*, Phys. Rev. Lett. 59 (1987) 688–691.

[190] F. Smole and J. Furlan, *Effects of abrupt and graded a-Si:C:H/a-Si:H interface on internal properties and external characteristics of p-i-n a-Si:H solar cells*, J. Appl. Phys. 72 (1992) 5964–5969.

[191] S. Solntsev, M. Trijssenaar, M. Zeman, J.A. Willemen and J.W. Metselaar, *Investigation of the Interface Properties of Single Junction a-Si Solar Cells by Inverse Modelling*, Proc. 12th Eur. Com. Phot. Sol. En. Conf., Amsterdam, the Netherlands (1994) 100–103.

[192] C.M. Soukoulis, M.H. Cohen and E.N. Economou, *Exponential Band Tails in Random Systems*, Phys. Rev. Lett. 53 (1984) 616–619.

[193] W.E. Spear, R.J. Loveland and A. Al-Sharbaty, *The temperature dependence of photoconductivity in a-Si*, J. Non-Cryst. Solids 15 (1974) 410–422.

[194] W.E. Spear and P.G. LeComber, *Substitutional doping of amorphous silicon*, Solid State Commun. 17 (1975) 1193–1196.

[195] W.E. Spear and P.G. LeComber, *Electronic properties of substitutionally doped amorphous Si and Ge*, Phil. Mag. 33 (1976) 935–949.

[196] W.E. Spear and P.G. LeComber, *Chapter 3* in *The Physics of Hydrogenated Amorphous Silicon I*, ed. J.D. Joannopoulos and G. Lucovsky, Springer Verlag, Berlin, 1984.

[197] W.E. Spicer and T.M. Donovan, *Electronic structure of amorphous Ge*, Phys. Rev. Lett. 24 (1970) 595–598.

[198] D.L. Staebler and C.R. Wronski, *Reversible conductivity changes in discharge-produced amorphous Si*, Appl. Phys. Lett. 31 (1977) 292–294.

[199] D.L. Staebler and C.R. Wronski, *Optically induced conductivity changes in discharge-produced hydrogenated amorphous silicon*, J. Appl. Phys. 51 (1981) 3262–3268.

[200] H.F. Sterling and R.C.G. Swan, *Chemical Vapor Deposition promoted by r.f. Discharge*, Solid-State Electron. 8 (1965) 653–654.

[201] R.A. Street, *Doping and the Fermi Energy in Amorphous Silicon*, Phys. Rev. Lett. 49 (1982) 1187–1190.

[202] R.A. Street, J. Kakalios and T.M. Hayes, *Thermal equilibrium in doped amorphous silicon*, Phys. Rev. B34 (1986) 3030–3033.

[203] R.A. Street, J.C Knights, D.K. Biegelsen, *Luminescence studies of plasma-deposited hydrogenated silicon*, Phys. Rev. B18 (1978) 1880–1891.

[204] R.A. Street, C.C. Tsai, J. Kakalios and W.B. Jackson, *Hydrogen diffusion in amorphous silicon*, Phil. Mag. B56 (1987) 305–320.

[205] R.A. Street, *Hydrogenated amorphous silicon*, Cambridge University Press, Cambridge, U.K., 1991.

[206] M. Stutzmann, *The doping efficiency in amorphous silicon and germanium*, Phil. Mag. B53 (1986) L15-L21.

[207] M. Stutzmann, D.K. Biegelsen and R.A. Street, *Detailed investigation of doping in hydrogenated amorphous silicon and germanium*, Phys. Rev. B35 (1987) 5666–5701.

[208] M. Stutzmann, *Charge-Induced Structural Relaxation in Hydrogenated Amorphous Silicon*, Adv. Solid State Phys. 28, 1–20.

[209] M. Stutzmann, *The defect density in amorphous silicon*, Phil. Mag. B60 (1989) 531–546.

[210] M. Stutzmann, R.A. Street, C.C. Tsai, J.B. Boyce and S.E. Ready, *Structural, optical, and spin properties of hydrogenated amorphous silicon-germanium alloys*, J. Appl. Phys. 66 (1989) 569–592.

[211] M. Suzuki, T. Maekawa, Y. Kakimoto, T. Bandow, *Properties of pure amorphous films prepared by rf-bias sputtering*, J. Phys. C4 (1981) 623–626.

[212] T. Suzuki, Y. Osaka and M. Hirose, *Theoretical Interpretation of Capacitance-Voltage Characteristics of Metal–a-Si:H Schottky Barriers*, Jap. J. Appl. Phys. 22 (1983) 785–788.

[213] S.M. Sze, *Physics of Semiconductor Devices*, John Wiley & Sons, New York, USA, 1981.

[214] S.M. Sze, *High-speed semiconductor devices*, John Wiley & Sons, New York, USA, 1990, 283.

[215] G. Tao, B.S. Girwar, G.E.N. Landweer, M. Zeman and J.W. Metselaar, *Enhanced Light absorption in a-Si:H layers of solar cells by applying TCO/metal back contacts*, Mat. Res. Soc. Symp. Proc. 297 (1993) 845–849.

[216] J. Tauc, R. Grigorovici and A. Vancu, *Optical Properties and Electronic Structure of Amorphous Germanium*, Phys. Stat. Sol. 15 (1966) 627–637.

[217] J. Tauc, *Optical properties of solids*, ed. F. Abelès, North-Holland, Amsterdam, the Netherlands, 1972, 277.

[218] J. Tauc, *Amorphous and liquid semiconductors*, Plenum Press, London, 1974.

[219] Y. Tawada, H. Okamoto and Y. Hamakawa, *a-SiC:H/a-Si:H heterojunction solar cell having more than 7.1 % conversion efficiency*, Appl. Phys. Lett. 39 (1981) 237–239.

[220] Y. Tawada, M. Kondo, H. Okamoto and Y. Hamakawa, *Hydrogenated amorphous silicon carbide as a window material for high efficiency a-Si solar cells*, Solar Energy Mater. 6 (1982) 299–315.

[221] Y. Tawada, K. Tsuge, M. Kondo, H. Okamoto and Y. Hamakawa, *Properties and structure of a-IC:H for high-efficiency a-Si solar cell* J. Appl. Phys. 53 (1982) 5273–5281.

[222] M.J. Thompson, *A comparison of amorphous and poly crystalline TFT's for LCD displays*, J. Non-Cryst. Solids 137&138 (1991) 1209–1214.

[223] T. Tiedje, *Evidencce for Exponential Band Tails in Amorphous Silicon Hydride*, Phys. Rev. Lett. 46 (1981) 1425–1428.

[224] T. Tiedje, *Information about Band-Tail States from Time-of-Flight Experiments*, Semiconductors and Semimetals Vol. 21, part C, Academic Press, Orlando (1984) 207–238.

[225] S.G. Tomlin, *Optical reflection and transmission formulae for thin films*, J. Phys. D1 (1968) 1667–1671.

[226] S.G. Tomlin, *More formulae relating to optical reflection and transmission by thin films*, J. Phys. D5 (1972) 847–851.

[227] M. Trijssenaar, G.E.N. Landweer, L.L.A. Vosteen, J.W. Metselaar, *Highly conductive micro-crystalline p- and n-type layers for amorphous silicon tandem solar cells*, Proc. 11th Eur. Com. Phot. Sol. En. Conf., Montreux, Swiss (1992) 564–567.

[228] M. Trijssenaar, M. Zeman and J.W. Metselaar, *Investigation of the interface properties of hydrogenated amorphous silicon p-i junctions*, J. Non-Cryst. Solids 164–166 (1993) 667–670.

[229] M. Trijssenaar, M. Zeman and J.W. Metselaar, *Highly Transparent, Micro Crystalline, Doped Silicon Carbide for the Application in Tandem Solar Cells*, Proc. 12th Eur. Com. Phot. Sol. En. Conf., Amsterdam, the Netherlands (1994) 346–349.

[230] M. Trijssenaar, M. Zeman, J.A. Willemen, G. Tao and J.W. Metselaar, *Computer modeling: a tool for solar cell optimization*, Proc. of the Vijfde Nederlandse Zonne-energie Conferentie, Veldhoven, the Netherlands (1995) 278–280.

[231] C.C. Tsai, *Characterization of amorphous semiconducting silicon-boron alloys prepared by plasma decomposition*, Phys. Rev. B19 (1979) 2041–2055.

[232] C.C. Tsai, R. Thompson, C. Doland, F.A. Ponce, G.B. Anderson and B. Wacker, *Transition from amorphous to crystalline silicon: effect of hydrogen on film growth*, Mat. Res. Soc. Symp. Proc. 118 (1988) 49–54.

[233] H.K. Tsai and S.C. Lee, *Amorphous SiC/Si three-color detector*, Appl. Phys. Lett. 52 (1988) 275–277.

[234] F. Urbach, *The Long-Wavelength Edge of Photographic Sensitivity and of the Electronic Absorption of Solids*, Phys. Rev. 92 (1953) 1324.

[235] M. Vaněček, J. Kočka, J. Stuchlík and A. Tříska, *Direct measurement of the gap states and band tail absorption by constant photocurrent method in amorphous silicon*, Solid State Commun. 39 (1981) 1199–1202.

[236] M. Vaněček, J. Kočka, J. Stuchlík, Z. Kožíšek, O. Štika and A. Tříska, *Density of the gap states in undoped and doped glow discharge a-Si:H*, Solar Energy Mater. 8 (1983) 411–423.

[237] M. Vaněček, A. Abrahám, O. Štika, J. Stuchlík and J. Kočka, *Gap States Density in a-Si:H Deduced from Subgap Optical Absorption Measurement on Schottky Solar Cells*, Phys. Stat. Sol. A83 (1984) 617–623.

[238] P.E. Vanier, F.J. Kampas, R.R. Cordermann and G. Rajeswaran, *A study of hydrogenated amorphous silicon deposited by rf glow discharge in silane-hydrogen mixtures*, J. Appl. Phys. 56 (1984) 1812–1820.

[239] S. Vepřek and W. Peier, *Chemical Equilibrium in nonisothermal low pressure plasma*, Chemical Physics 2 (1973) 478–484.

[240] S. Vepřek, Z. Iqbal, H.R. Oswald, F.A. Scott and J.J. Wagner, *Parameters controlling the deposition of amorphous and microcrystalline silicon in Si/H discharge plasmas*, J. Phys. C4 (1981) 251–255.

[241] S. Vepřek, M. Heintze, F.A. Sarott, M. Jurčik-Rajman and P. Willmott, *Mechanisms of plasma induced silicon deposition and the control of the properties of the deposit*, Mat. Res. Soc. Symp. Proc. 118 (1988) 3–17.

[242] S. Vepřek, *Chemistry and solid state physics of microcrystalline silicon*, Mat. Res. Soc. Symp. Proc. 164 (1990) 39–49.

[243] J.J. Wagner and S. Vepřek, *Kinetic Study of the Heterogeneous Si/H System Under Low-Pressure Plasma Conditions by Means of Mass Spectrometry*, Plasma Chem. Plasma Process. 2 (1983) 95–107.

[244] J.J. Wagner and S. Vepřek, *Chemical Relaxation Study of the Heterogeneous Silicon-Hydrogen System Under Plasma Conditions*, Plasma Chem. Plasma Process. 3 (1983) 219–234.

[245] X. Wang, Y. Bar-Yam, D. Adler and J.D. Joannopoulos, *DC conductivity and the Meyer-Neldel rule in a-Si:H*, Phys. Rev. B38 (1988) 1601–1604.

[246] H. Wiesmann, A.K. Ghosh, T. McMahon and M. Strongin, *a-Si:H produced by high-temperature thermal decomposition of silane*, J. Appl. Phys. 50 (1979) 3752–3754.

[247] G. Willeke, *Physics and electronic properties of microcrystalline semiconductors*, in Amorphous & microcrystalline semiconductor devices, Volume II: Materials and Device Physics, ed. J. Kanicki, Artech house, Boston, London, 1992, 55–88.

[248] J.A. Willemen, M. Zeman and J.W. Metselaar, *Computer modeling of amorphous silicon tandem cells*, Proc. of the First World Conf. on Photovoltaic Energy Conversion, Hawaii (1994), to be published.

[249] K. Winer and L. Ley, *Surface states and the exponential valence-band tail in a-Si:H*, Phys. Rev. B36 (1987) 6072–6078.

[250] K. Winer, I. Hirabayashi and L. Ley, *Distribution of occupied near-surface bandgap states in a-Si:H*, Phys. Rev. B38 (1988) 7680–7693.

[251] K. Winer, *Defect formation in a-Si:H*, Phys. Rev. B41 (1990) 12150–12161.

[252] M.A. Wolfe, *Numerical Methods for Unconstrained Optimization*, Workingham: van Nostrand Reinhold, 1978.

[253] H.F. Wolf, *Semiconductors*, John Wiley & Sons, New York, USA, 1971.

[254] D.L. Wood and J. Tauc, *Weak Absorption Tails in Amorphous Semiconductors*, Phys. Rev. B5 (1972) 3144–3151.

[255] C.R. Wronski, S. Lee, M. Hicks and Satyendra Kumar, *Internal Photoemission of Holes and the Mobility Gap of Hydrogenated Amorphous Silicon*, Phys. Rev. Lett. 63 (1989) 1420–1423.

[256] J. Yang, R. Ross, T. Glatfelter, R. Mohr, G. Hammond, C. Bernotaitis, E. Chen, J. Burdick, M. Hopson and S. Guha, *High efficiency multi-junction solar cells using amorphous silicon and amorphous silicon-germanium alloys*, Proc. of the 20th IEEE Photovoltaic Specialists Conf. (1988) 241–246.

[257] B.G. Yoon and C. Lee, *Effect of the statistical shift on the anomalous conductivities of n-type hydrogenated amorphous silicon*, J. Appl. Phys. 60 (1986) 673–676.

[258] T. Yoshida, K. Maruyamaa, O. Nabeta, Y.Ichikawa, H. Sakai and Y. Uchida, *High efficiency a-Si:H two-stacked tandem solar cell*, Proc. of the 19th IEEE Photovoltaic Specialists Conf. (1987) 1095–1100.

[259] S. Yoshida, K. Seki, K. Nabeshima, S. Katayama, S. Kitahara and A. Ohmura, *Effect of the p/i interface layer on the performance of a-Si:H solar cells*, Techn. Digest of the 5th Photovoltaic Science and Engineering Conf., Kyoto, Japan (1990) 371–374.

[260] M. Zeman, I. Ferreira, M.J. Geerts and J.W. Metselaar, *The effect of hydrogen dilution on glow discharge a-SiGe:H alloys*, Solar Energy Mater. 21 (1991) 255–265.

[261] M. Zeman, J.A. Willemen, S. Solntsev and J.W. Metselaar, *Amorphous Silicon Solar Cell Parameters Extraction by Inverse Modelling*, Techn. Digest of the 7th Intern. Photovoltaic Science and Engineering Conf., Nagoya, Japan (1993) 609–610.

[262] M. Zeman, G. Tao, M. Trijssenaar, J.A. Willemen, J.W. Metselaar and R.E.I. Schropp, *Application of the defect pool model in modelling of a-Si:H solar cells*, Mat. Res. Soc. Symp. Proc. 1995 (in press).

[263] M. Zhu and H. Fritzsche, *Density of states and mobility-lifetime product in hydrogenated amorphous silicon, from thermostimulated conductivity and photoconductivity measurements*, Phil. Mag. B53 (1986) 41–54.

[264] M. Zhu, *A Study of the density of Gap States in Amorphous Semiconductors from Thermostimulated Conductivity Spectra*, Appl. Phys. A52 (1991) 285–288.

List of main symbols

Symbol	Description	Unit
A	fraction absorbed light in a film	1
d	film thickness	cm
D_n	electron diffusion coefficient	$\mathrm{cm^2\,s^{-1}}$
D_p	hole diffusion coefficient	$\mathrm{cm^2\,s^{-1}}$
E	energy	eV
E_0	Urbach energy	eV
E_C	conduction band energy level	eV
E_F	Fermi level	eV
$E_{g,mob}$	mobility band gap, equals $E_C - E_V$	eV
$E_{g,opt}$	optical band gap, equals $E_b - E_a$	eV
E_V	valence band energy level	eV
E_σ	activation energy	eV
e	electron charge	C
$f(E)$	occupation probability function	1
G	total generation rate	$\mathrm{C\,cm^{-3}}$
G_L	generation rate under illumination	$\mathrm{C\,cm^{-3}}$
$\hbar$	Planck's constant	eV s
$\hbar\omega$	photon energy	eV
I	incident photon flux	$\mathrm{s^{-1}cm^{-2}}$
J_n	electron current density	$\mathrm{A\,cm^{-2}}$
J_p	hole current density	$\mathrm{A\,cm^{-2}}$
k	Boltzmann's constant	$\mathrm{J\,K^{-1}}$
$k(\omega)$	extinction coefficient	1
kT_C	conduction band characteristic energy	eV
kT_V	valence band characteristic energy	eV
m_e	electron mass	kg
n	free electron concentration	$\mathrm{cm^{-3}}$
$n(\omega)$	refractive index	1
n_{loc}	free electron concentration in localized states	$\mathrm{cm^{-3}}$

Symbol	Description	Unit
N_{db}	dangling bond density	cm^{-3}
N_A	acceptor concentration	cm^{-3}
N_C	effective density of states in the conduction band	cm^{-3}
N_D	donor concentration	cm^{-3}
N_V	effective density of states in the valence band	cm^{-3}
$N(E)$	density of states distribution function	$\mathrm{cm}^{-3}\,\mathrm{eV}^{-1}$
p	free hole concentration	cm^{-3}
p_{loc}	free hole concentration in localized states	cm^{-3}
q	magnitude of the electron charge	C
R	total recombination rate	$\mathrm{C\,cm}^{-3}$
T	absolute temperature	K
T_m	Meyer-Neldel characteristic temperature	K
$\alpha(\omega)$	absorption coefficient	cm^{-1}
$\alpha_{2.3}$	absorption coefficient at 2.3 eV	cm^{-1}
ϵ	dielectric permittivity	$\mathrm{F\,cm}^{-1}$
$\tilde{\varepsilon}(\omega)$	complex dielectric constant	1
λ	light wavelength	nm
$\mu(E)$	carrier mobility	$\mathrm{cm}^2\,\mathrm{V}^{-1}\,\mathrm{s}^{-1}$
μ_n	electron mobility	$\mathrm{cm}^2\,\mathrm{V}^{-1}\,\mathrm{s}^{-1}$
μ_p	hole mobility	$\mathrm{cm}^2\,\mathrm{V}^{-1}\,\mathrm{s}^{-1}$
ρ	space charge density	$\mathrm{C\,cm}^{-3}$
σ_0	conductivity prefactor	$\mathrm{S\,cm}^{-1}$
σ_{00}	Meyer-Neldel characteristic conductivity prefactor	$\mathrm{S\,cm}^{-1}$
σ_d	dark conductivity	$\mathrm{S\,cm}^{-1}$
σ_{ph}	photoconductivity	$\mathrm{S\,cm}^{-1}$
σ_{ph}/σ_d	photosensitivity	1
τ	carrier lifetime	s
ϕ	work function	eV
χ	electron affinity	eV
ψ	electrostatic potential	V
ω	angular frequency	rad

SUMMARY

Amorphous and microcrystalline silicon deposited by Plasma Enhanced Chemical Vapor Deposition is used in commercial solar cells. In the past 18 years the initial efficiency of single-junction p-i-n amorphous silicon solar cells has increased steadily from 2.4% of the first solar cells to 13.2% presently.

In this thesis investigations in two fields of solar cell research are described, viz. concerning p-type material for use in solar cells, and simulations. First, we investigated the deposition, characterization and optimization of p-type amorphous and microcrystalline silicon based materials for use in solar cells. Secondly, amorphous silicon solar cells were investigated with computer simulations. Chapter 1 gives an introduction to these subjects.

Chapter 2 and 3 deal with optical and electrical measurements on amorphous and microcrystalline silicon-based materials, in order to determine the quality of the p- and i-type material and to obtain a baseline set of parameters for simulations of devices.

Chapter 2 deals with measurements and the analysis of the optical properties of thin amorphous and microcrystalline films. The reflectance and transmittance of UV, visible and IR light of thin films was measured, from which the thickness of the film, the refractive index and the absorption was derived.

The optical and electrical properties of amorphous silicon and related materials, such as microcrystalline silicon and alloys of it, are predominantly determined by the density of states (DOS). Therefore, to perform realistic modeling, it is necessary to have knowledge about the DOS. We determined the DOS in the band gap of intrinsic amorphous silicon with the Constant Photocurrent Method (CPM) and from Dual Beam Photoconductivity (DBP) measurements. The two methods use different methods to circumvent the difficulty that the carrier lifetime, and thus the sub band gap photoconductivity, depends on the carrier concentration, and thus on the illumination intensity. We have demonstrated that within experimental error CPM and DBP yield the same results for the

DOS. The measurements of the DOS of a-Si:H deposited in our laboratory confirms the device quality of this material.

Further, chapter 2 describes the relation between the Urbach energy and the optical gap, as found by Cody [24, 25]. Our measurements show that this relation is only valid if the optical gap is varied by other means than alloying it. Alloying amorphous silicon with carbon or germanium changes the band gap without a corresponding change in the Urbach energy, as predicted by the relation between the Urbach energy and the optical gap. The relation quantifies the trade-off between the optical and electrical properties of the intrinsic layer of a solar cell. From an electrical point of view, the lower the defect density of the intrinsic layer, the better, because the recombination of photo-generated carriers becomes lower. But the lower the defect density, the lower the Urbach energy. From Cody's relation, the lower the Urbach energy, the higher the optical gap, and thus the lower the absorption is, which is undesirable, because the lower the absorption, the less the photo-generated current can be.

Last, chapter 2 describes optical simulations to determine the energy dependence of the extended states. A computer model was developed which relates the DOS with the absorption coefficient. The different models of the DOS distribution were tested to fit the measured absorption coefficient. If a constant dipole matrix element is assumed to describe the optical transitions best, as found by Jackson in 1985 [75], a parabolic energy dependence is found. This leads to the determination of the optical gap according to Cody's method.

Because light enters the cell from the p-layer side, the p-layer and the p/i-junction are the most critical parts in the single-junction solar cell. Because of the importance of the p-layer, we deposited several series of p-doped amorphous silicon carbide, microcrystalline silicon and microcrystalline silicon carbide which are suitable for use in solar cells. The suitability of these materials for solar cell use is investigated by determining their refractive index, absorption coefficient, dark and photoconductivity and their Fermi level position as functions of the deposition conditions. These topics are covered in chapter 3.

Also, in this chapter, the conduction mechanisms in amorphous semiconductors and the Meyer-Neldel (MN) rule are described. The MN rule

gives the relation between the prefactor of the dark conductivity and the activation energy, where previously it was found that amorphous silicon and its alloys obey the MN rule. Our measurements on μc-Si:H and μc-SiC:H show that the MN rule also applies to microcrystalline silicon and its carbon alloys.

Concerning microcrystalline silicon carbide films, we found that below a critical methane/silane ratio of the source gas the films were microcrystalline, while above this critical ratio the films were amorphous. These ratios are 8 % and 12 % for n-doped and p-doped films, respectively. In the microcrystalline regime, the films became more transparent and less conducting with increasing carbon content.

Chapter 4 describes simulations of solar cells. Device simulations offer notable advantages over the actual production and measurement of devices: simulations are generally much cheaper, the impact of small changes of a configuration can be determined much faster and more reliably and it is possible to examine the influence of input parameters which are otherwise hard or impossible to set independently.

We investigated solar cells and theirs p/i-junction by means of simulations. First, we determined a baseline set of parameters by fitting the dark and illuminated JV-characteristics of a single-junction solar cell. Next, we used modeling to examine the influence of material parameters on the JV-characteristics of the p/i-junction. We found that the mobility of the charge carriers, the density of gap states and the introduction of an defect layer show the most pronounced effect on the JV-characteristics.

By means of forward simulations we established that it is feasible to extract the band lineup of a p/i-heterojunction by fitting its measured JV-characteristics to simulated ones. With the inverse modeling technique, the band lineup of an experimental p/i-heterojunction was actually determined. We found that the offset was both in the valence and conduction band, in contrast with the common assumption that the offset is totally accommodated by the conduction band. The determined band lineup agrees within error with X-ray photoelectron spectroscopy measurements.

Chapter 5 gives a reśumé of the thesis and recommendations for future research concerning the topics covered in the thesis.

Concluding, this work has led to better p-type material for use in solar cells, and to more insight into the optical and electrical characteristics of the materials used in solar cells.

SAMENVATTING

Amorf en microkristallijn silicium gefabriceerd met de Plasma Enhanced Chemische Damp Neerslag methode wordt toegepast in commerciële zonnecellen. Sinds de eerste amorf silicium zonnecel, 18 jaar geleden, heeft een gestage groei van het rendement plaatsgevonden, van 2.4 % van de eerste cel, tot 13.2 %, hedendaags.

Dit proefschrift beschrijft onderzoek op twee gebieden ter verbetering van amorf silicium zonnecellen, nl. betreffende p-type gedoteerd materiaal voor toepassing in zonnecellen en betreffende simulaties. De depositie, karakterisatie en optimalisatie van p-type amorf en microkristallijn silicium en koolstoflegeringen hiervan zijn uitgevoerd, met als oogmerk de toepassing van deze materialen in zonnecellen. Tevens is met behulp van computersimulaties onderzoek verricht naar het gedrag van amorf silicium zonnecellen. Hoofdstuk 1 geeft een introductie in deze onderwerpen.

In hoofdstuk 2 en 3 zijn optische en elektrische metingen op amorf en microkristallijn silicium gebaseerde materialen beschreven. Met behulp van deze metingen is de kwaliteit van de p- en i-type lagen vastgesteld en is een uitgangsset parameters ten behoeve van het modelleren van amorf silicium devices verkregen.

Hoofdstuk 2 behandelt de metingen en de analyse van de optische eigenschappen van dunne amorfe en microkristallijne silicium lagen. De reflectie en transmissie van UV, zichtbaar en IR licht is gemeten en uit deze metingen is de laagdikte, de brekingsindex en de absorptiecoëfficiënt van de lagen bepaald.

De optische en elektrische eigenschappen van de besproken materialen worden voornamelijk bepaald door de toestandsdichtheid van energieniveaus (DOS) binnen en buiten de verboden band. Daarom is kennis van de DOS een conditio sine qua non voor het realistisch modelleren van amorf silicium devices. Wij hebben de DOS in de verboden band bepaald met de Constante Fotostroom Methode (CPM) en met behulp van Dubbelstraals Fotogeleidings (DBP) metingen, waarbij wij laten zien dat deze twee methoden binnen de experimentele onzekerheid dezelfde

resultaten opleveren. De twee methoden verschillen in de manier waarop omgegaan wordt met het gegeven dat de levensduur van de ladingdragers afhankelijk is van de concentratie van deze, en dus afhankelijk is van de belichtingssterkte. De metingen tonen aan dat het amorf silicium gefabriceerd in onze depositieopstelling van zeer hoogwaardige kwaliteit is.

Hoofdstuk 2 beschrijft tevens de relatie tussen de Urbach energie en de optische bandafstand, welke relatie voor het eerst door Cody beschreven is [24, 25]. Onze metingen laten zien dat de relatie tussen de Urbach energie en de optische bandafstand slechts geldig is als de optische bandafstand op andere manieren dan door legeren veranderd wordt. Legeren van amorf silicium met koolstof of met germanium verandert de optische bandafstand zonder een corresponderende verandering van de Urbach energie teweeg te brengen, zoals door Cody's relatie voorspeld wordt. Deze relatie kwantificeert de afweging tussen de optische en elektrische eigenschappen van de intrinsieke laag van een zonnecel. Des te lager de toestandsdichtheid van deze laag en dus des te lager de Urbach energie, des te beter. Echter, volgens de relatie van Cody gaat een lage Urbach energie gepaard met een hoge optische bandafstand, hetgeen ongewenst is daar de absorptie dan minder is en dus de maximale fotostroom tevens lager is.

Als laatste zijn in hoofdstuk 2 simulaties beschreven om de energieafhankelijkheid van de extended states toestandsdichtheid te bepalen. Een computermodel is ontwikkeld welke de optische absorptie berekent uit de toestandsdichtheid. Wij hebben verschillende modellen voor de toestandsdichtheid getest of deze de gemeten absorptie kunnen verklaren. Als aangenomen wordt dat bij optische overgangen het dipoolmoment behouden is, hetgeen is aangetoond door Jackson in 1985 [75], vinden wij een parabolische afhankelijkheid van de toestandsdichtheid als functie van de energie. Dit geeft aanleiding geeft om de optische bandafstand te bepalen volgens de methode van Cody.

Omdat het licht door de p-type laag de zonnecel binnenkomt, zijn de p-type laag en de p/i-overgang de meest kritische onderdelen van een zonnecel. Vanwege het belang van een goede p-laag hebben wij meerdere series amorf siliciumcarbide, microkristallijn silicium en microkristallijn siliciumcarbide, geschikt voor gebruik in zonnecellen, gefabriceerd en

gekarakteriseerd. De geschiktheid voor zonnecelgebruik is bepaald door de brekingsindex, de absorptiecoëfficiënt, de donker- en licht-geleiding en het Ferminiveau te bepalen als functie van de depositieomstandigheden, hetgeen in hoofdstuk 3 beschreven is.

Tevens zijn in dit hoofdstuk de geleidingsmechanismen en de Meyer-Neldel (MN) relatie beschreven. De MN relatie geeft het verband tussen de voorfactor van de donkergeleiding en de activatieënergie. Eerder is gevonden dat amorf silicium en legeringen hiervan aan deze regel voldoen. Onze metingen wijzen uit dat deze relatie tevens van toepassing is op microkristallijn materiaal en koolstoflegeringen hiervan.

Betreffende de microkristallijne siliciumcarbide lagen, vonden wij dat beneden een kritieke verhouding van methaan tot silaan in het gasmengsel de lagen microkristallijn groeien, terwijl daarboven de lagen amorf werden. Voor n-type en p-type lagen waren deze verhoudingen respectievelijk 8 % en 12 %. In het microkristallijne gebied zijn de lagen transparanter en minder geleidend naarmate meer methaan aan het gasmengsel wordt toegevoegd.

Hoofdstuk 4 behandelt computersimulaties. Simulaties brengen belangrijke voordelen boven de feitelijke produktie van devices met zich mee: over het algemeen zijn simulaties goedkoper, de invloed van kleine veranderingen in een configuratie kunnen sneller en betrouwbaarder onderzocht worden en parameters kunnen onafhankelijk van elkaar veranderd worden, hetgeen in een hardware device zeer lastig of zelfs onmogelijk kan zijn.

Wij hebben zonnecellen en hun p/i-overgang met behulp van simulaties onderzocht. Als eerste is met behulp van invers modelleren een basisset van simulatieparameters bepaald door de gesimuleerde en gemeten donker en licht IV-karakteristieken van een single-junction zonnecel te fitten. Vervolgens is via simulaties de invloed van verschillende materiaal parameters op de IV-karakteristieken van de p/i-overgang onderzocht. Wij vonden dat de mobiliteit, de toestandsdichtheid en de introductie van een defectlaag de grootste invloed op de IV-karakteristieken hebben.

Met behulp van simulaties is aangetoond dat de ligging van de banden in de p- en i-laag ten opzichte van elkaar een zodanige invloed op de IV-karakteristieken hebben dat het mogelijk is met behulp van invers model-

leren de bandenligging ten opzichte van elkaar te bepalen. Wij hebben deze bepaling voor een experimentele structuur uitgevoerd, waarbij wij vonden dat zowel de valentieband als de geleidingsband verschuiven bij de materiaalovergang, in tegenstelling tot de algemeen gebruikte aanname dat de sprong volledig in de geleidingsband ligt. De bandenligging komt binnen de experimentele fout overeen met Röntgenstraling foto-electronen spectroscopie metingen.

Hoofdstuk 5 tenslotte, geeft de conclusies van het onderhavige werk en doet aanbevelingen betreffende vervolgonderzoek.

Samenvattend kan gesteld worden dat dit werk heeft geleid tot verbeterd p-type materiaal voor gebruik in zonnecellen en tot meer inzicht in de elektrische en optische eigenschappen van de materialen gebruikt in zonnecellen.

Biography

Marcel Trijssenaar was born in The Hague, the Netherlands, on April 6, 1965. His secondary education was completed at the Daltonscholengemeenschap in The Hague, after which he attended the one-year course of the Vrije Hogeschool in Driebergen. The focus of this course was on general, personal development, and several subjects, such as the arts, sociology, psychology and a life perspective are given.

Subsequently, he commenced his studies at the Delft University of Technology. He obtained a B.Sc. in Chemical Engineering in August 1985 and a B.Sc. in Physical Engineering in November 1986 (both cum laude). His graduate work concerned the development of low-level software for a pipelined, parallel computer and he graduated with a M.Sc. in Physical Engineering in May 1990.

In September 1990, he became a Research Assistant at the Electrical Materials Laboratory of the Faculty of Electrical Engineering at the Delft University of Technology, where he conducted research on amorphous silicon solar cells. The results of the research are described in this thesis.

ACKNOWLEDGEMENTS

The research described in this thesis could not have been carried out without the help, guidance and interaction from many people, both during my time spent as a Ph.D. student, as well as earlier.

First of all, I would like to thank my parents for continuously stimulating me to learn, to do the best and most I can and to enjoy life as much as possible. I would like to thank Inge for being understanding when I was working more than 40 hours a week to finish this job.

Also, I would like to thank all the other people who, in one way or another, contributed to this thesis, whether as outlined above, or by moral, practical or other means of support.

To mention some names with respect to recent years, I would like to thank Dr. J.W. Metselaar for providing me with the opportunity to undertake this Ph.D. research. His optimistic view on life and confidence in people shaped the space for this research. I would like to thank Dr. M. Zeman for his attendance, helpful discussions and for critically reading and commenting on this manuscript. I would like to thank the other Ph.D. students for fruitful discussions and productive cooperation. Also, I would like to thank the technicians: Ben Girwar for carrying out numerous measurements with great enthusiasm and accuracy, Jan van Staden for fabricating the devices and Jan Chris Staalenburg for providing the reliable computer system. Of the students, I would especially like to thank Amir Vosteen, who did most of the measurements described in chapter 2. His graduate work led him to become a Ph.D. student at our laboratory.

I would like to mention the people of the Department of Atomic and Interface Physics of the University of Utrecht, our research partner, for the cooperation. Last but not least, I appreciate the correction of this manuscript by Ms. Zaat-Jones very much.